Systematic Analysis of Light Ion Yields and Dose Equivalents from Thick Targets Bombarded by Proton, Helium, and Heavy Ions

A Dissertation Presented for the
Doctor of Philosophy
Degree
The University of Tennessee, Knoxville

Hui-Chen Wang

May 2019

ACKNOWLEDGEMENTS

This Work was supported by Grants NNX17Al10A and NNX15AD89A from NASA.

I would like to express my sincere gratitude to Dr. Lawrence Heilbronn for being my advisor. I couldn't have come this far without his patience and advising. I also greatly appreciate his understanding while I was having a hard time.

I would also like to thank Dr. Lawrence Townsend, Dr. Yuri Kamyshkov, Dr. Maik Lang for being on my committee and giving me comments on my work.

I also appreciate the help from Dr. Michael Sivertz, Dr. Adam Rusek, Rory Rosselot and Main Control from Brookhaven National Laboratory; Dr. Chiara La Tessa from the University of Trento, Italy; Dr. Cary Zeitlin from Leidos; Dr. Martha Clowdsley, Dr. Steve Blattnig, Dr. John Norbury, Dr. Ryan Norman, Dr. Tony Slaba, Dr. Charlie Werneth, Mr. David Moore, and Mr. Kevin Somervill from NASA Langley Research Center throughout this project.

I also want to express my special thanks to members in Dr. Heilbronn's research group, Dr. Pi-En Tsai, Dr. Matthew Beach, Dr. Natalie McGirl, Dr. Luis Castellanos, Dr. Ashwin Srikrishna, Hunter Ratliff, and Tyler Steiner.

Finally but importantly, I would like to thank my parents and brothers for their unwavering support and encouragement. I'm also grateful to David Sikorski for being there for me. And special thanks to my friends all over the world, Hung-Yi (Gino) Liu, Trei Yuan, Christine Young, Jessica Lee, Wei-Neng Hsu, Mimi Chou, Yaohung Mike Tsai, Elyse Shih, Wan-Yu Tsai, Yan-Ru Lin, Shao-Yu Wang, Hao-Hsien Fang, HongWei Tzeng, Yupi Su, Heng-An Wang and YuWen Huang. Thank you all!

ABSTRACT

Galactic cosmic rays (GCR) originating from outside the solar system create a unique radiation environment in space, which is difficult to replicate on Earth. Transport codes are used to simulate the space radiation environment and to evaluate dose and dose equivalent behind shielding for manned space missions. However, the accuracy of these transport codes depends on the accuracy and availability of the experimental data used to verify the physics models. Therefore, a series of experiments were performed to study thick-target light charged particle yields produced from GCR-like ion interactions with shields.

This dissertation presents secondary light charged particle (Z=1 and 2) measurements performed in November 2016 and November 2017 at the National Aeronautics and Space Administration (NASA) Space Radiation Laboratory at Brookhaven National Laboratory (BNL). Double-differential thick-target yields were calculated for protons, deuterons, tritons, helium-3, and helium-4. These yields were calculated from measurements collected by organic liquid scintillators oriented at 10, 30, 45, 60, 80, and 135 degrees with respect to the beam direction. The beams consisted of 400-, 800-, and 2500-MeV [megaelectron volt] protons and 400-, 800-, and 1500-MeV/n [megaelectron volt per nucleon] He, C, Si, Fe ions incident on thick targets (20, 40, and 60 g/cm^2 [grams per centimeter squared] aluminum and high-density polyethylene (HDPE), and 20 and 60 g/cm^2 combination of aluminum and HDPE). In the analysis, pulse shape discrimination and time of flight techniques were used to produce secondary charged particle angular-energy spectra. Additionally, the spectra were compared with Monte Carlo simulations using Particle and Heavy Ion Transport code System (PHITS) and Monte Carlo N-Particle Transport code (MCNP). Also, dose equivalents were calculated from the measured double-differential thick-target light charged particle yields using the International Commission on Radiological Protection (ICRP) 60 quality factor and the NASA quality factors for solid cancers and leukemia. These experimental data will be integrated into NASA's uncertainty analysis for optimization of future GCR shielding design.

TABLE OF CONTENTS

LIST OF TABLES

LIST OF FIGURES

CHAPTER ONE
INTRODUCTION

1.1 Dissertation Overview

For long duration deep-space missions, astronauts will be exposed to Galactic Cosmic Rays (GCRs) which can cause a health risk. In order to protect crew members from the radiation environment in space, thick shielding materials are required to reduce the exposure. Since the unique radiation environment in space is difficult to reproduce and test on Earth, transport codes are used to simulate the space radiation environment and to evaluate different shielding materials and thicknesses. However, the accuracy of these transport codes depends on the accuracy and the availability of the experimental data used to verify the physics models. Therefore, over the past three years, a series of experiments were performed to study previously unmeasured thick-target secondary particle yields produced from GCR-like ion interactions with a variety of shielding materials and thicknesses. Particularly, these experiments measured secondary light charged particle yields that are critical to help benchmark various transport codes.

This dissertation presents a series of light charged nuclei (Z<3) measurements performed in November 2016 and November 2017 at the National Aeronautics and Space Administration (NASA) Space Radiation Laboratory at Brookhaven National Laboratory (BNL). Double-differential thick-target light charged particle yields were calculated from the experimental data measured at six angles in the laboratory. The light charged particle yield results were compared to a series of Monte Carlo simulations using Particle and Heavy Ion Transport code System (PHITS) and Monte Carlo N-Particle Transport code (MCNP). Also, dose equivalents were calculated from the measured double-differential thick-target light charged particle yields using the International Commission on Radiological Protection (ICRP) 60 quality factor [1] and the NASA quality factors for solid cancers and leukemia [2]. These double-differential thick-target light charged particle yield results will eventually be incorporated into uncertainty quantification of various transport codes by NASA to optimize future GCR shielding to protect crew members from the radiation exposure in space.

1.2 Original Contribution

The double-differential thick-target light charged particle (Z=1 and 2) yields at six angles produced by 400-, 800-, and 2500-MeV protons and 400-, 800-, and 1500-MeV/n He, C, Si, Fe ions bombarding thick upstream targets (20, 40, and 60 g/cm^2 aluminum and high-density polyethylene (HDPE), and 20 and 60 g/cm^2 combination of aluminum and HDPE) have never been measured before. In previous measured experiments in literature, the measurements were done by using single target, so the placements of the second 60 g/cm^2 downstream target in the experiments performed for this dissertation is unique. In addition, the PHITS simulations presented in this work were designed by the author to compare with the experimental yields. The comparison between the experimental data, and PHITS and MCNP simulated results presented in this work will benefit the discussion on the differences between these Monte Carlo simulations for light charged particle production from thick target bombardment and will further help improve the physics models used in the transport codes. Furthermore, the dose equivalent calculations associated with the measured double-differential thick-target light charged particle yields using ICRP 60 quality factor and the NASA quality factors for solid cancers and leukemia provide a new dataset for discussion on the quality factors in terms of track structure model. Overall, the 39 analyzed beam and target combination systems generating 1469 light charged particle yield spectra will be a benchmark dataset for comparisons to various transport codes to help investigate the accuracy of the transport codes. Also, the specific achievements done by the author are summarized in the following section.

1.3 Dissertation Goal

The general goal of this dissertation is to provide an extensive and new double-differential thick-target secondary light charged particle yield data produced from GCR-like ion interactions with a variety of shielding materials and thicknesses and then compute dose equivalent data associated with the measured light charged particle yields for all analyzed systems. The specific achievements done by the author, with the exception of the MCNP calculations performed by Hunter Ratliff, for this dissertation are:

1. Produce 1469 double-differential thick-target light charged particle (p, d, t, ^{3}He, and ^{4}He) yield spectra measured by organic liquid scintillators at six angles for 39 beam and target combination systems across five beam projectile species, three beam energies, and three types of targets (20, 40, and 60 g/cm^2 aluminum and high-density polyethylene (HDPE), and 20 and 60 g/cm^2 combination of aluminum and HDPE).
2. Determine statistical, energy, and systematic uncertainties for all experimental data.
3. Calculate dose equivalents from analyzed light charged particle yields using the ICRP 60 quality factor and the NASA quality factors for solid cancers and leukemia to provide new database.
4. Model the experimental setup with PHITS and compare the experimental results with PHITS and MCNP calculations.
5. Complete systematic analysis across beam species, beam energies, target materials, and target thicknesses.

1.4 Dissertation Outline

This dissertation is organized as follows:

Chapter Two provides background information and the review of literature with measurements similar to the work presented in this dissertation.

Chapter Three includes the experimental setup and Monte Carlo simulation designed for comparisons to experimental results.

Chapter Four contains the data analysis methodology used for this work.

Chapter Five includes the experimental and Monte Carlo simulated double-differential thick-target yield results, as well as the dose equivalent data.

Chapter Six states conclusions and future work.

CHAPTER TWO
BACKGROUND INFORMATION AND LITERATURE REVIEW

2.1 Galactic Cosmic Rays

Galactic cosmic rays (GCR) originate from outside the solar system and are composed of varieties of charged particles with energies over a range from tens of MeV/n to several TeV/n, where the maximum GCR flux occurs within the range from 200 to 1000 MeV/n (Figure 2.1). The extensive measurements using balloons and satellites showed that about 98% of GCR are composed of hadrons and the remaining 2% of GCR consist of electrons and positrons. The hadronic component of GCR includes on average 87% protons, 12% helium, and 1% heavier nuclei with all orbital electrons stripped [4]. Figure 2.2 shows the relative abundance of GCR component and their estimated dose contribution, which illustrates that heavy ions contribute to significant amount of dose before adding shield [5].

2.2 Secondary Radiation Field

When primary GCR is incident on thick shielding materials, GCR may slow down or even stop in the shield due to atomic interactions, or the heavier ions in GCR can fragment into a variety of secondary particles by a series of nuclear interactions. These projectile fragments most likely retain the velocity of the projectile and can transport further in the shielding material since the stopping power of fragments is smaller. While these lighter projectile fragments travel through the shield, target fragmentation can occur leading to more secondary particle production [6],[7]. With the secondary particle production, there is a possibility that the dose equivalent received behind the shield could increase when shielding heavy ions. Figure 2.3 shows the annual dose equivalents in units of centi-sievert behind aluminum, polyethylene, and TransHab shields, which is a multilayer wall material developed by NASA Johnson Space Center [8], using the 1977 solar minimum GCR environment from Badhwar and O’Neill’s 1996 GCR model [9]. After adding 1.51 g/cm2 shielding materials, polyethylene is the only one that decreased the annual dose equivalent,

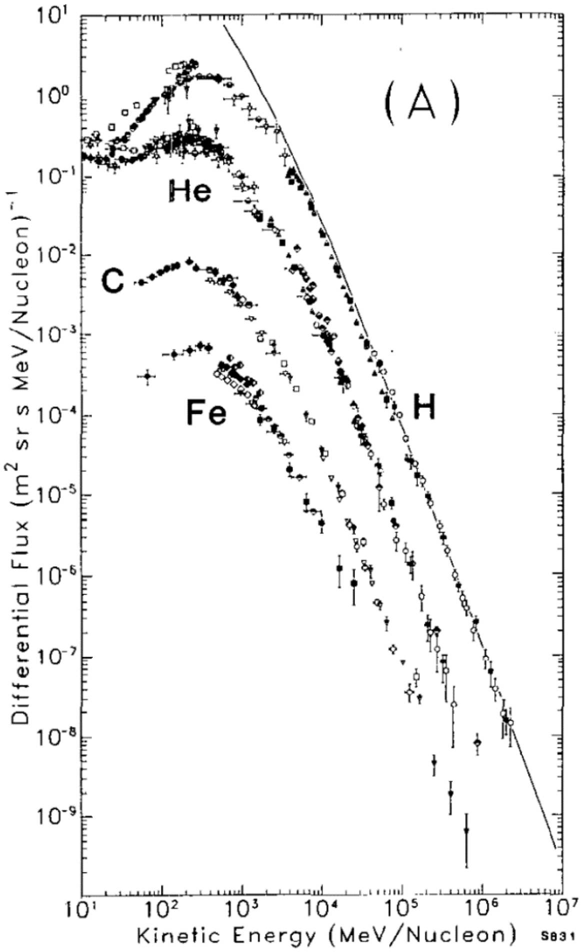

Figure 2.1. The differential energy spectrum of selected ions in GCR measured at Earth using balloons and satellites [3].

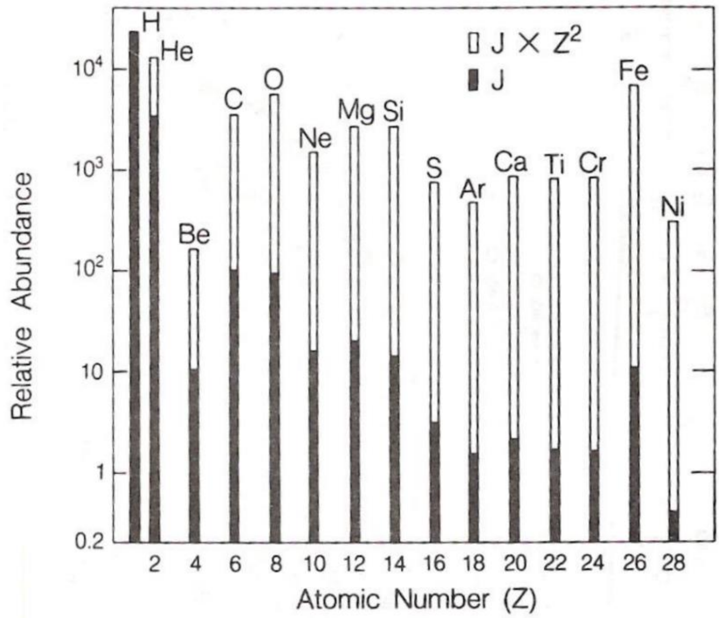

Figure 2.2. The relative abundance (black) and estimated dose contribution (white) of GCR components [5].

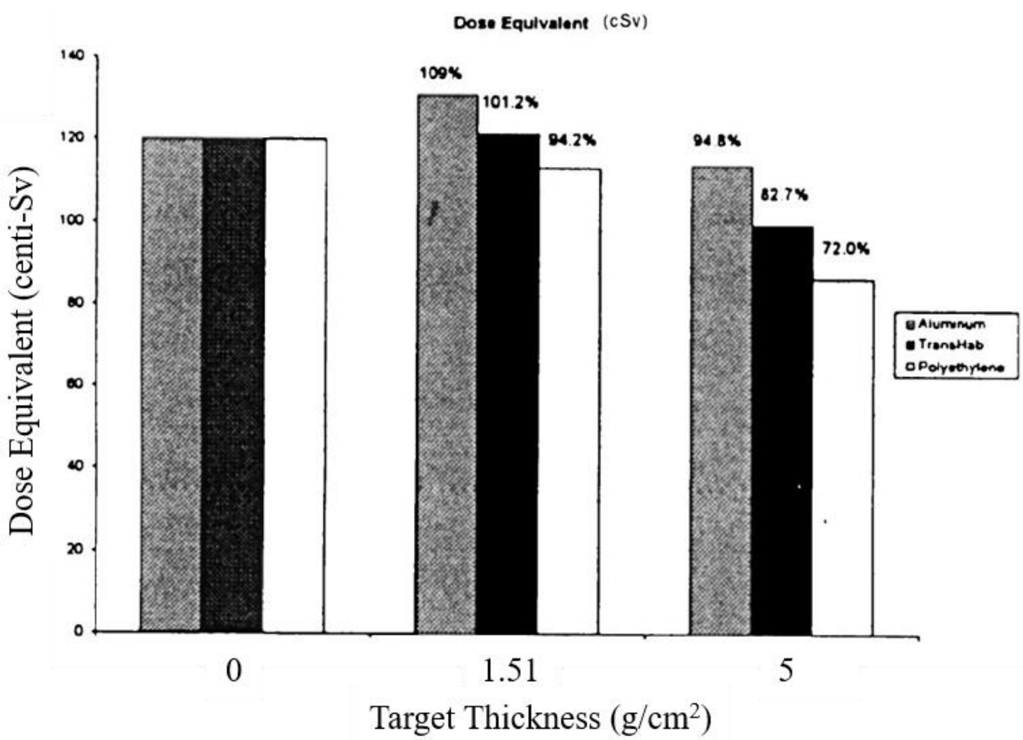

Figure 2.3. Dose equivalent behind different thicknesses of three shielding materials [8].

while the other two shielding materials increased the annual dose equivalents received behind the shields [8].

As mentioned earlier, transport codes are utilized to model GCR interactions with shielding materials. These transport codes have uncertainties directly associated with the lack of data in the database used to validate the physics models. This is the reason that an extensive database of experimental measurements is necessary, which can provide information to compare with simulation results to validate the transport codes and quantify the uncertainty. A study for GCR incident on different shielding materials using various transport codes was conducted by Slaba *et al.* [10]. In this study, four Monte Carlo transport codes (FLUKA [11], Geant4 [12], MCNP6 [13], and PHITS [14]) and three versions of the deterministic code HZETRN (N=1: straight-ahead approximation, N=2: bi-direction, and N=34: three-dimension [15],[16]) were used to calculate dose and dose equivalent behind different shielding materials and thicknesses. The GCR boundary condition used in these simulations was the solar minimum GCR environment from Badhwar and O'Neill's 2010 GCR model (BON2010) [17]. The geometry in this study modeled the upstream and downstream slabs with a thin water layer in between, which simulated an enclosed shielding environment for space applications. In the enclosed shielding environment, primary GCR may interact with one side of the shield (upstream shield) first and then interact with the other side of the shield (downstream shield) if GCR penetrates the upstream shield. As primary GCR travels through the upstream shield, a variety of secondary particles produced may also interact with the downstream shield. Figure 2.4 shows the total dose equivalent for GCR boundary condition on aluminum and HDPE targets as a function of thickness. Dose equivalent in this study was calculated by using linear energy transfer (LET)-dependent ICRP 60 quality factor [1]. As you can see in Figure 2.4, the total dose equivalent value decreases at first and then starts to increase beyond 20 g/cm^2 of aluminum shielding. At the same time, the calculation using HDPE shielding doesn't show the presence of a local minimum in dose equivalent as a function of HDPE shielding thickness but also doesn't show a significant decrease as the shielding

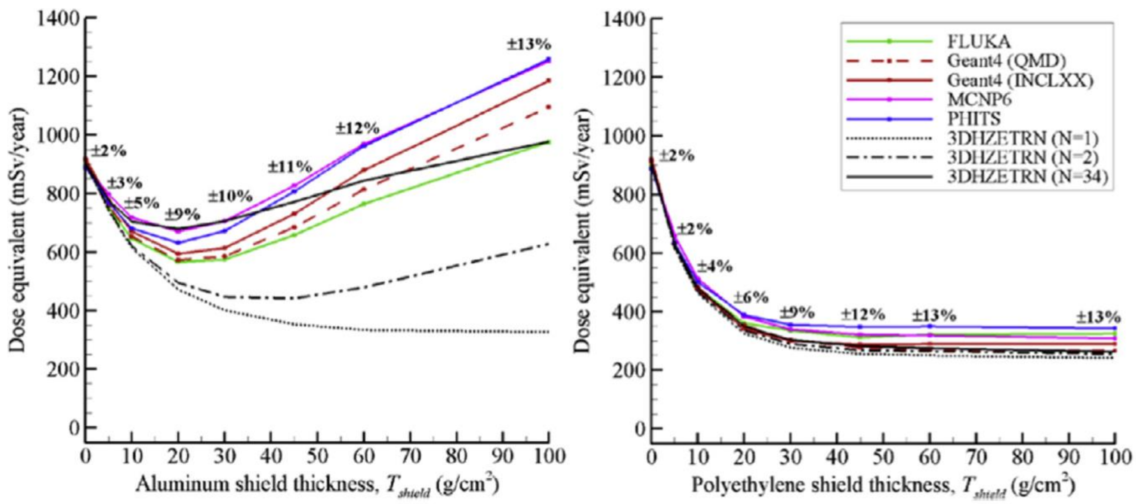

Figure 2.4. Total dose equivalent for GCR boundary condition on various thicknesses of aluminum (left) and HDPE (right). The relative variations between Monte Carlo codes and 3DHZETRN (N=34) results are indicated as percentages in the plot [10].

thickness increases. The results in this study also show that about 70% of total dose equivalent was from proton contributions at large shielding thicknesses (Figure 2.5) and 10-20% of total dose equivalent was from the remaining light ions. For the proton contributions at large shielding thicknesses, the secondary protons produced by neutron-hydrogen elastic collisions contributed to about 50% of the proton dose equivalent and the secondary protons produced by proton-nucleus nonelastic collisions contributed to about 25% [10]. Overall, the proton dose equivalent comes from primary and secondary protons as well as neutrons. Additional calculations using HZETRN 2010 space radiation transport code conducted by Walker *et al.* [18] also demonstrated the charged particles and neutron contributions to organ dose equivalents from exposures to the 1977 solar minimum GCR spectrum for various shielding geometries, including spheres and locations within the Space Transportation System and the International Space Station (ISS). The results showed that heavy ions contributed about 50% or more to organ dose equivalent for the shielding thickness equal to or less than 5 g/cm^2. On the other hand, about 75 to 85% or more of the organ dose equivalents were from proton, alpha, and neutron for thick shields. All these results ([10] and [18]) demonstrated that light ions and neutrons were the main contributors to the total dose equivalent behind thick shields.

However, in the study by Slaba *et al.* [10], the difference of various transport code results for total dose equivalent in thick shielding environment, which was significantly attributed to secondary light ions and neutrons, illustrates the uncertainties in the secondary particle production models between various transport codes. The difference in the total dose equivalent results between four MC codes and 3DHZETRN (N=34) was quantified by dividing the difference between maximum and minimum results by the average of maximum plus minimum results at a given thickness [10]. The variations between different transport codes illustrate the necessity to provide more experimental data to validate the physics models and quantify uncertainties.

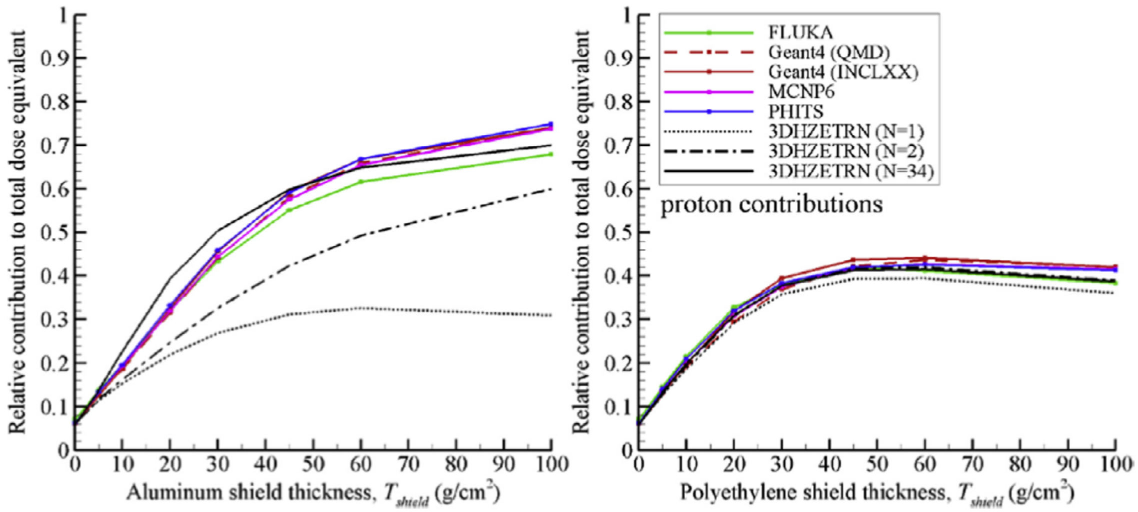

Figure 2.5. Dose equivalent contributions from protons for GCR boundary condition on various thicknesses of aluminum (left) and HDPE (right) [10].

2.3 Dose Equivalent for Space Radiation

The secondary particles produced by shielding primary GCR are of interest because the dose equivalent received behind the shield may increase in certain situations [8], [10]. Dose equivalent (H) is a quantity that can be used to appropriately evaluate the health risks resulted from the radiation fields. The results in the studies [10], [18], and [19] show that the secondary light ions and neutrons contribute to a majority of the total dose equivalent for thickly shielded environments, which brings the focus onto secondary light ion and neutron production. Since it is difficult to replicate the full GCR environment on Earth, various transport codes are used to model the GCR environment, which will need experimental results to compare with and lead to improvements in the physics models in those codes. In most of transport codes, the LET-dependent ICRP 60 quality factor [1] is used to calculate the dose equivalent. The ICRP 60 quality factor is determined as a function of the LET of incoming radiation particle in water. The integral of organ dose equivalent is calculated by multiplying the quality factor $(Q(LET))$ by the absorbed dose (D) in the organ of interest, as shown below:

$$H = D \times Q. \quad (2.1)$$

Despite the extensive usage of the ICRP 60 quality factor, NASA has developed new models to evaluate radiological risk. The new models took epidemiological and radiobiological data, which show the differences between solid tumors and leukemia in Relative Biological Effectiveness (RBE), into consideration [2]. In order to derive new risk cross sections for risk assessment during space missions, the comprehensive computational methods, modeling of track structure and the resultant damage to biological structures and molecules, have been used [20]. This then contributed to new formulations of quality factors appropriate for space radiations. The NASA quality factor ($Q_{NASA}(Z, \beta)$) includes the concepts of track structure rather than only LET-dependence and is defined as a function of charge (Z) and velocity (β) [2], [20]. Figure 2.6 shows the NASA quality factor for solid cancers as a function of ${Z^*}^2/\beta^2$ for different ions, which Z^* is the effective charge of ions. At a given ${Z^*}^2/\beta^2$, the value of NASA quality factor is smaller for Fe, which illustrates the concept of track structure model. For a give value of ${Z^*}^2/\beta^2$, heavier particles will have a larger velocity. Also, this reveals that charge (Z) and velocity (β) are required to determine the NASA quality factor [2]. This demonstrates that the NASA quality factor includes a more convincing consideration of different biophysical processes, while the ICRP 60 quality factor does not. The dose equivalent data in section "5.3 Dose Equivalent Results" will present if there is any significant difference between using the ICRP 60 quality factor and the NASA quality factors for solid cancers and leukemia for the GCR-like beam systems conducted in the experiments for this dissertation.

2.4 Literature Summary

Norbury *et al.* [21] conducted a comprehensive literature review on existing measured nuclear cross-section data critical for space radiation. This study is mainly to identify the available nuclear cross-section data for space exploration and further recommend future cross-section measurements. The kinetic energy of projectiles was organized into four

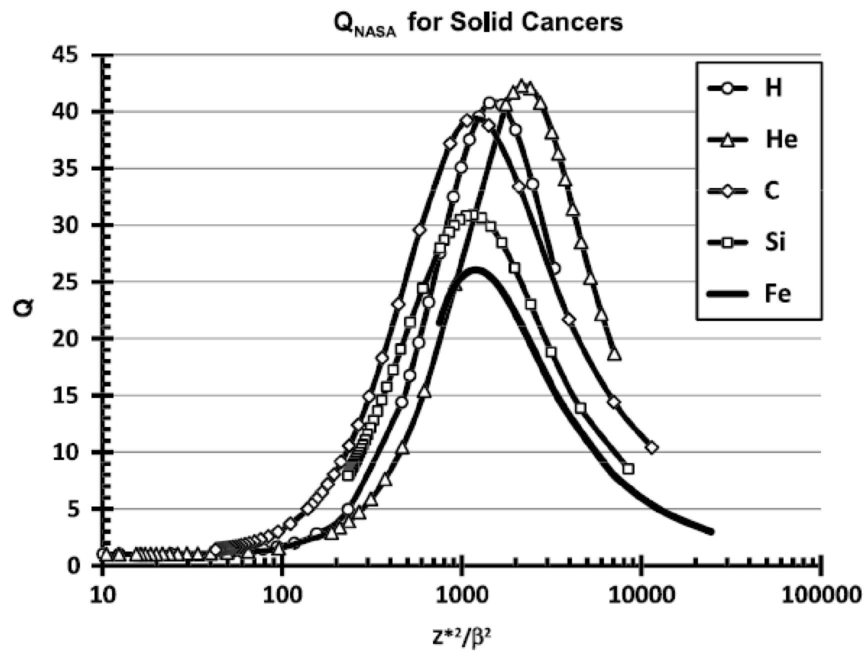

Figure 2.6. Q_{NASA} for solid cancers as a function of $(Z^*)^2/\beta^2$ [2].

different regions. The energy region in the study relevant to the experiments performed and presented in this dissertation is 280 MeV/n $\leq$ kinetic energy $<$ 3 GeV/n. The measured cross-section data for hydrogen and helium production from H, He, C, Si, and Fe projectiles are of interest here. For total cross-sections for hydrogen isotopes (p, d, and t), there are several measurements using H and C projectiles on various target materials and a few measurements using He projectiles. However, there's no measurement of total cross-section for hydrogen isotope using Si and Fe projectiles. For total cross-sections for helium isotopes (he-3 and he-4), there are some measurements using He projectiles on low atomic number target but no measurement using He projectiles on a variety of heavier target material. The total cross-sections for helium isotope using C projectiles on various target are available but there's a lack of measurements using Si and Fe projectiles. On the other hand, the double-differential cross-sections for hydrogen isotopes from H projectiles are well-represented but there are not many double-differential cross-sections for hydrogen isotopes from He, C, Si, and Fe projectiles. Similar to the double-differential cross-sections for hydrogen isotopes, most of the double-differential cross-sections for helium isotopes are for H projectiles. There are some measurements of the double-differential cross-sections using He and C projectiles but not using Si and Fe projectiles. Overall, within the energy range similar to the experiments performed for this dissertation, most of the total cross-section and double-differential cross-section data are for H projectiles and there're some data available using He and C projectiles. However, the cross-section data from He, C, Si, and Fe projectiles are generally not represented, especially for Si and Fe projectiles [21], which illustrates the necessity to perform more cross-section measurements for these projectiles.

Other than the cross-section measurements, there are some measurements incorporated similar double-differential thick-target light charged particle yield presented in this dissertation, which will be discussed below. The measurements of proton, deuteron, and triton at 0°, 7.5°, 15°, 30°, 60°, and 90° for 100 MeV/n helium projectiles on 5 cm thick carbon, 4 cm carbon, 1.5 cm thick copper, and 1.5 cm thick lead targets were conducted at

Heavy Ion Medical Accelerator in Chiba (HIMAC) [22]. The target thicknesses were selected to fully stop the beam projectiles. The experimental results were compared with the LAHET Code System (LCS) [23]. Another light charged particle yields measurement using helium projectiles was performed by Rovituso *et al.* at the Heidelberg Ion-Beam Therapy Center in Heidelberg [24]. Protons, deuterons, tritons, helium-3, and helium-4 produced by 120 and 200 MeV/n helium projectiles on water target were measured at 0°, 2°, 4°, 6°, 8°, 12°, and 23°. The target thicknesses were 4.28 and 13.92 cm, which were selected to attenuate half of the range of 120 and 200 MeV/n helium projectiles in water respectively.

The study conducted by Gunzert-Marx *et al.* included the measured secondary charged particle production for 200 MeV/n carbon projectiles on 12.78 cm thick water target at the GSI Helmholtz Centre for Heavy Ion Research (GSI) in Darmstadt [25]. The target thickness was selected to be able to stop the 200 MeV/n carbon projectiles. The double-differential light charged particle yield spectra at 0°, 5°, 10°, 20°, and 30° were generated and then compared with PHITS simulations. Additionally, another double-differential charged particle yield measurement for carbon projectiles with energy of 200 and 400 MeV/n on water target was studied by Haettner et al. [26]. There were seven different target thicknesses (5.9, 15.9, 25.8, 27.9, 28.8, 31.2, and 34.7 cm). The angular distributions of hydrogen, helium, and heavier fragments (B, Be, and Li) were measured at 0°, 1°, 2°, 3°, 4°, 5°, 6° and 8°. Table 2.1 summarizes the review conducted for the existing experimental double-differential thick-target light charged particle yield measurements.

For the measurements mentioned above, three of them were conducted for the purpose of characterizing fragmentation of radiation therapy so that the beam projectiles were mainly helium-4 or carbon and the target choice was tissue-like water with thickness that was able to stop the projectiles. Also, their beam energy was lower than 400 MeV/n. Measurements of GCR-like projectile (Si and Fe) or beam energy up to 800 and 1500 MeV/n have not been found. Moreover, the light charged particle yield produced from target thickness from

20 to 60 g/cm^2 bombarded by H, He, C, Si, and Fe have not been seen. However, all these will be presented in this dissertation.

Table 2.1. Existing double-differential thick-target light charged particle yield measurements.

Beam Projectile	Energy (MeV/n)	Target	Measured Ions	Measured Angle (degree)	Reference
He-4	100	C, Al, Cu, Pb	p, d, t	0, 7.5, 15, 30, 60, 90	[22]
He-4	120, 200	H_2O	p, d, t, he-3, he-4	0, 2, 4, 6, 8, 12, 23	[24]
C-12	200	H_2O	p, d, t, he-3, he-4	0, 5, 10, 20, 30	[25]
C-12	200, 400	H_2O	H, He, Li, Be, B	0, 1, 2, 3, 4, 5, 8	[26]

CHAPTER THREE
EXPERIMENT SETUP AND MONTE CARLO SIMULATION OVERVIEW

3.1 Experimental Setup

3.1.1 Overview

Secondary light charged particles (proton, deuterons, tritons, helium-3, and helium-4) were measured at 10°, 30°, 45°, 60°, 80°, and 135° with respect to the beam direction and upstream target center using organic liquid scintillator arrays at the NASA Space Radiation Laboratory (NSRL) facility at Brookhaven National Laboratory (BNL) in November 2016 and November 2017. The Booster accelerator at BNL was used to deliver five separate beam species to the NSRL target room. The heavy ion projectiles were accepted from the Electron Beam Ion Source (EBIS) and the proton projectiles were accepted from the Tandem van de Graaff accelerators. The 400-, 800-, and 2500-MeV protons and 400-, 800-, and 1500-MeV/n He, C, Si, Fe beams entered the NSRL target room 121.92 cm above the floor and were projected to the center of 20, 40, and 60 g/cm^2 thick aluminum and HDPE, and 20 and 60 g/cm^2 thick combination of aluminum and HDPE upstream targets with area of 30 x 100 cm^2. Also, a 60 g/cm^2 thick aluminum or HDPE downstream target with area of 100 x 100 cm^2 was placed downstream 3.5 m from the middle of the upstream target. The downstream target was added to study the secondary radiation field created by interactions in the downstream target, which are not studied in this work. A full list of beam projectile and target combination systems can be seen in Table 3.1. A schematic of the upstream target and the downstream target combinations is shown in Figure 3.1.

In the November 2016 and November 2017 experiments, 400-, 800-, and 2500-MeV protons and 400-, 800-, and 1500-MeV/n He, C, Si, Fe beams were selected. The ranges of these beam projectiles were calculated by using Stopping and Range of Ions in Matter

Table 3.1. List of beam species and incident energies, and target systems. Gray, blue, and green boxes indicate measurements occurred in March 2016, November 2016, and November 2017, respectively. Diagonal boxes were the systems analyzed by Luis Castellanos, a former graduate student in Department of Nuclear Engineering at UTK.

Beam Energy (MeV/n)	Beam Species				
	H	He	C	Si	Fe
400	Al	Al	Al	Al	Al
	HDPE	HDPE	HDPE	HDPE	HDPE
	Al+HDPE	Al+HDPE	Al+HDPE	Al+HDPE	Al+HDPE
800	Al	Al	Al	Al	Al
	HDPE	HDPE	HDPE	HDPE	HDPE
	Al+HDPE	Al+HDPE	Al+HDPE	Al+HDPE	Al+HDPE
1500 (2500 for H)	Al	Al	Al	Al	Al
	HDPE	HDPE	HDPE	HDPE	HDPE
	Al+HDPE	Al+HDPE	Al+HDPE	Al+HDPE	Al+HDPE

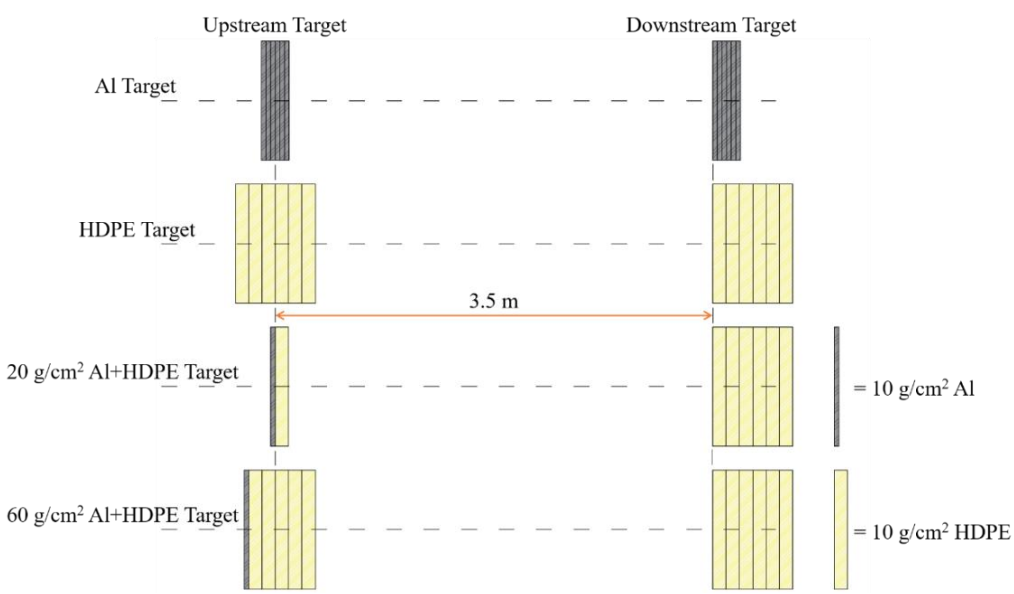

Figure 3.1. Schematic of the upstream target and the downstream target combinations.

Version 2008 (SRIM-2008) [28]. For all the beam-target systems, some beam projectiles punched through the upstream target and struck the downstream target, while some beam projectiles fully stopped in the upstream target (Table 3.2).

3.1.2 Detector Information

A schematic of the NSRL target room experimental setup is shown in Figure 3.2. Figure 3.3 shows the tube that enclosed the two thin EJ-228 plastic "start" scintillators (S1 and S2), which were placed 3 cm apart inside the tube. The midpoint of start scintillator tube was placed 383.8 cm downstream from the beam exit window and 76.2 cm upstream from the middle of the upstream target. S1 and S2 are both 0.2 cm thick, but S1 has smaller active cross-sectional area than S2, which allows the identification of valid beam particles that were on-axis relative to the center of the beam. The beam scintillators were also used to initiate timing information and to count the number of beam particles incident on the target. A summary of the detector properties related to this work is shown in Table 3.3.

Secondary light charged particles produced in the upstream target were measured by six organic liquid scintillators (OLS) with active volume of 12.7 cm in diameter and 12.7 cm in depth encased in 0.15-cm thick aluminum housing. These detectors were positioned at 10°, 30°, 45°, 60°, 80°, and 135° with respect to the beam direction and the midpoint of the upstream target, as shown in Figure 3.2. In these experiments, three EJ-301 liquid scintillators were used at the three forward-angle detectors (10°, 30°, and 45°), while three EJ-309 liquid scintillators were used at 60°, 80°, and 135°. Also, two 12.7 x 12.7 cm^2 and 0.635-cm-thick EJ-204 plastic organic scintillators (veto detectors) were paired with each OLS. One veto detector was placed before the front face of the OLS while the other one was placed at the side face of the OLS facing the beam line to ensure that secondary particles produced in the air column along the beam direction could be detected and removed from the data during analysis. The veto detectors were used to distinguish charged and neutral particle events which were detected in the liquid scintillators. One OLS and two paired veto detectors placed on a rolling detector stand to align with the height of the

Table 3.2. Beam projectiles that punched through (green) or stopped (red) in the upstream target. Diagonal boxes were the beam-target combination systems analyzed by Luis Castellanos.

Beam	Energy (MeV/n)	Upstream Target Thickness (g/cm^2)							
		Al			HDPE			Al+HDPE	
		20	40	60	20	40	60	20	60
H	400								
	800								
	2500								
He	400								
	800								
	1500								
C	400								
	800								
	1500								
Si	400								
	800								
	1500								
Fe	400								
	800								
	1500								

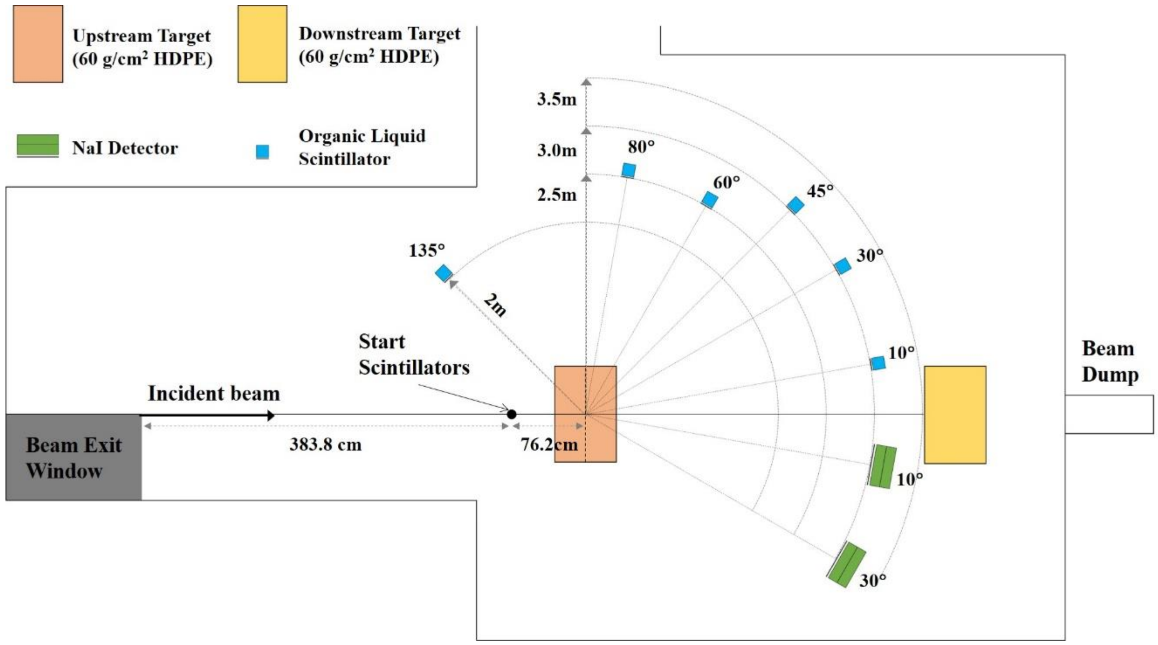

Figure 3.2. Top view of the experimental setup in the NSRL target room with 60 g/cm^2 upstream and downstream HDPE targets (to scale). Listed distances for organic liquid scintillators and NaI detectors are the nominal design distances which are slightly different from the real distances in the experiments.

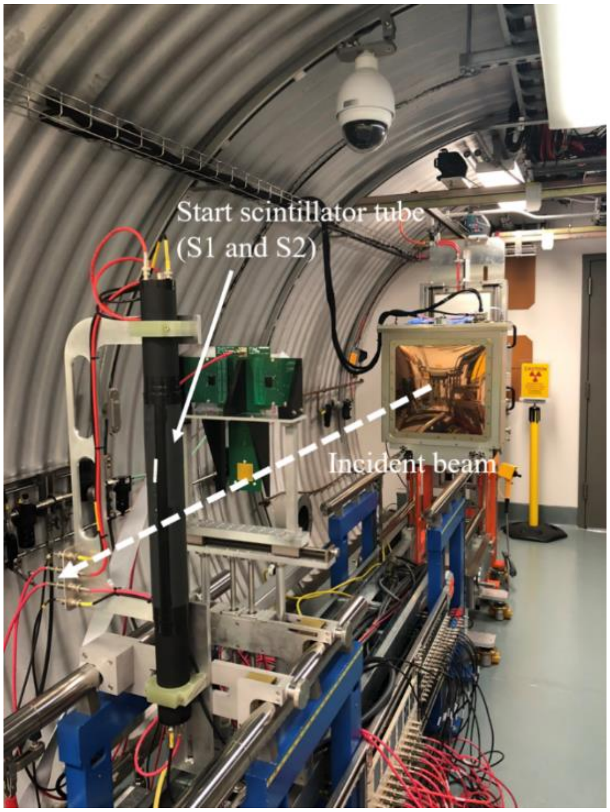

Figure 3.3. Start scintillator tube with two thin EJ-228 plastic scintillator detectors inside.

Table 3.3. Summary of detector properties.

Detector	Detector model	Material Properties	Dimensions
Beam start scintillator (S1 and S2)	EJ-228	Polyvinyl toluene Density: 1.023 g/cm^3	S1: 1 x 1 x 0.2 cm^3 S2: 1.4 x 1.4 x 0.2 cm^3
Organic liquid scintillator	EJ-301 (10°, 30°, and 45°)	Xylene, naphthalene, POPOP, and activators Density: 0.874 g/cm^3	12.7 cm in diameter 12.7 cm in depth
	EJ-309 (60°, 80°, and 135°)	Solvent xylene Density: 0.959 g/cm^3	
Veto detector	EJ-204	Polyvinyl toluene Density: 1.023 g/cm^3	12.7 x 12.7 x 0.635 cm^3

beam axis are shown in Figure 3.4. After all the detector stands were positioned, the flight paths were measured from the middle of the upstream target to the front face of the active OLS volume and the values are listed in Table 3.4.

3.1.3 Shadow Bar System

For the background neutron spectra, two iron shadow bars with a diameter of 12.7 cm (91 cm and 182 cm in length) placed between the upstream target and the OLS were utilized to separate background neutrons by blocking particles originating from the upstream target to the OLS. Those liquid scintillators with shadow bar in the front were considered "shadowed", which means only the background neutrons could be detected in the shadowed liquid scintillators. Four shadow bar configurations were used for each beam and target combination (configuration A: no shadow bars; configuration B: shadow bars at 10° and 60°; configuration C: shadow bars at 30° and 80°; configuration D: shadow bars at 45° and 135°). The liquid scintillator arrays and shadow bar configuration C can be seen in Figure 3.5. This shadow bar system was utilized to help the background neutron separation during the neutron measurement analysis. For the charged particle analysis, only non-shadowed runs were considered. The double-differential thick-target charged particle yields from shadowed runs were generally two orders of magnitude less than the double-differential thick-target charged particle yields measured from non-shadowed runs, which means the background subtraction would not contribute to significant differences in experimental double-differential thick-target charged particle yields [27].

3.2 Data Acquisition System

A data acquisition system logic diagram used for the experiments is shown in Figure 3.6. The logic equipment is presented in Table 3.5. The data acquisition system was triggered by the coincidence signal firing from the start scintillators (S1 and S2) and a subsequent signal from an event detected in an organic liquid scintillator (OLS) or a charged scintillator (CS) paddle and was stopped with a delayed signal ("STOP" signal) firing from the OLS or CS paddle that fired the subsequent signal. The trigger logic setup is shown in Figure 3.7. During this time, the timing and charge deposition information of all the

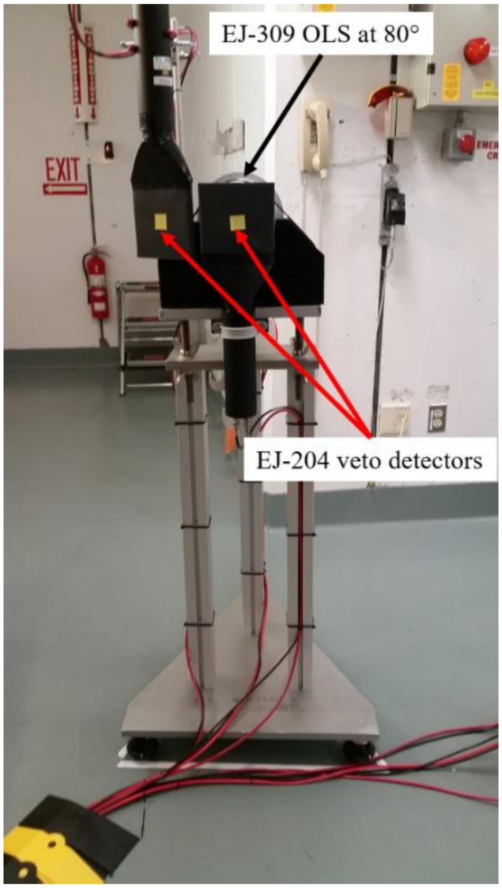

Figure 3.4. Organic liquid scintillator array at 80° on the detector stand.

Table 3.4. Flight paths from the middle of the upstream target to the front face of the active OLS volume.

Detector (angle)	Flight Path (cm)	
	November 2016	November 2017
10°	301.72	301.45
30°	301.28	301.98
40°	301.33	301.59
60°	251.31	252.09
80°	251.35	251.78
135°	201.93	201.31

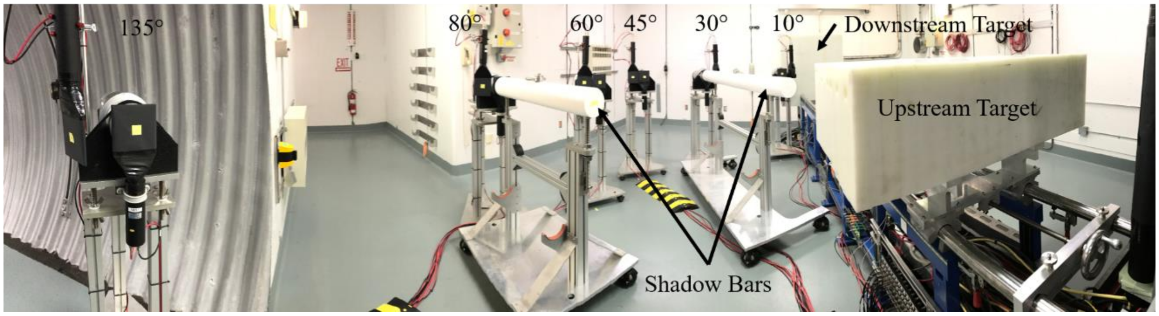

Figure 3.5. Six liquid scintillator arrays in position with shadow bar configuration C.

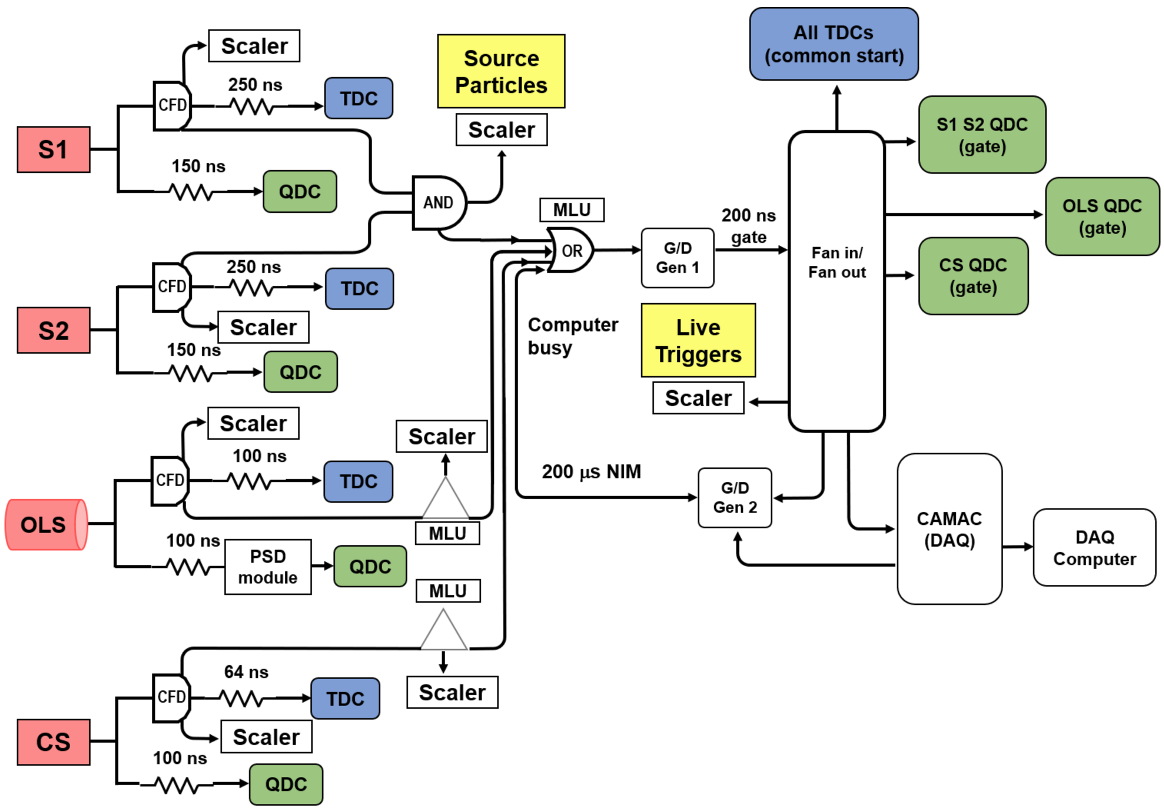

Figure 3.6. Data acquisition system logic diagram [30].

Table 3.5. Logic units used in the experiments relevant to data analysis in this dissertation.

Module	Model	# BITS
TDC	LeCroy 2228A	10
QDC	LeCroy 2249W	12
ADC	Ortec AD811	11
	LeCroy 2249A	12
Scaler	LeCroy 2551	24

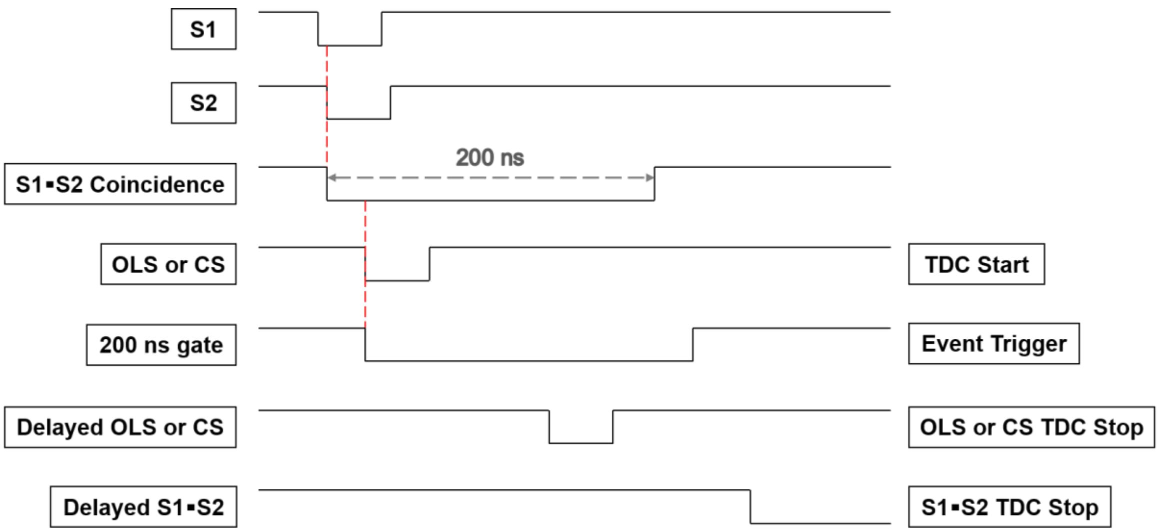

Figure 3.7. Trigger logic setup and relative timing.

detectors in the system was recorded using time-to-digital converters (TDCs) and charge-to-digital converters (QDCs). This trigger logic setup resulted in reverse timing information, which means that the time in the TDC histograms increases from right to left. The higher TDC channel numbers would represent the faster timing events, so the energy of particles increases from left to right. Figure 3.8 shows an example of reversing timing in the proton TDC histogram at 10° for the 400-MeV/n C on HDPE target.

When an incident particle passed through the start scintillators, the signal registered by each start scintillator was split. One signal was delayed and sent to a QDC to record the pulse height information, while the other signal was sent to a constant fraction discriminator (CFD). If the second signal surpassed the internal threshold, the CFD would output two logic NIM signals. One signal was delayed and sent to a TDC as a “STOP” signal. The other signal was sent to an “AND” coincidence gate, which fired a logic NIM signal if the signals from two start scintillators were in coincidence. Then, this logic NIM signal was sent to a MLU “OR” module. Other inputs sent into the MLU “OR” module were from OLS and CS which will be described in the following paragraph. The MLU “OR” module fired a signal when two out of three signals (OLS, CS, and S1·S2) came into the module.

The signal of each OLS was split. One signal was sent to a CFD to output one signal with a delayed to a TDC and another signal to the MLU “OR” module. Another signal from OLS was delayed and fed into a pulse shape discrimination (PSD) module. The PSD module then produced two attenuated signals (total attenuated signal and head attenuated signal) and two un-attenuated signals (total signal and head signal). The two head signals were produced by integrating the charge deposition within the first 20 to 35 ns (short gate) of the total 200 ns integration gate (long gate). The two attenuated signals were produced by dividing the un-attenuated signals by an internal factor to handle higher pulse height events. These four signals were then sent to a QDC. A similar electronic setup was also applied to each CS paddle, except no CS signal was sent to PSD module. In this thesis, the

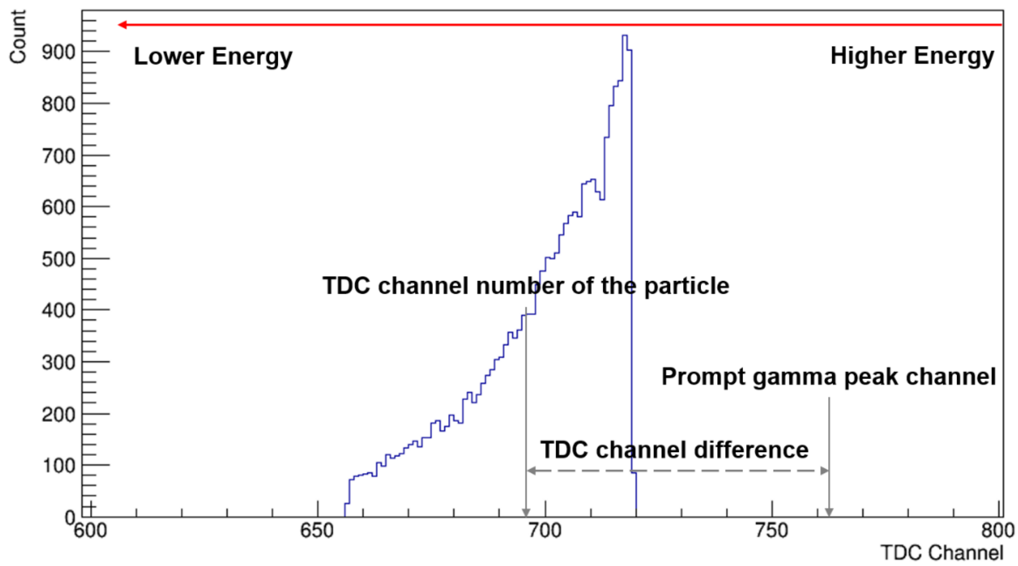

Figure 3.8. Proton time-of-flight spectrum at 10° for the 400-MeV/n C on HDPE target.

information from CS paddles was not used but CS paddles were included in the whole trigger logic in the data acquisition system.

The coincidence signal from S1 and S2 theoretically arrives at the MLU “OR” module first, so any subsequent signal from either the OLS or CS paddle will trigger the MLU “OR” module, firing a logic pulse to create a 200 ns gate. This 200 ns gate was used as the “START” signal for the TDCs and the charge deposition integration gate for the QDCs.

The raw event-by-event information recorded by the QDCs and the TDCs for each triggered event in each run was transferred to the data acquisition laptop (DAQ computer) from the CC-USB CAMAC Crate controller (CAMAC(DAQ)). The DAQ computer was installed with the SpecTcl analysis software developed by the National Superconducting Cyclotron Laboratory at Michigan State University. The acquisition system was used to monitor the data online and write the raw data to a single file for each run [29].

3.3 Monte Carlo Simulations

3.3.1 PHITS

The Monte Carlo simulation code, Particle and Heavy Ion Transport Code System (PHITS) version 2.88 [31] was used to calculate secondary light charged particle production to compare with experimental results. As described in reference [31], PHITS utilizes nuclear reaction models and data libraries to simulate nuclear and atomic collisions and transport particles between collisions. Figure 3.9 shows the physics models and data libraries used in the default setting but Electron Gamma Shower version 5 (EGS5) [32] in PHITS version 2.88. The Liège Intranuclear Cascade model (INCL) 4.6 [33] is utilized to simulate proton-, pion- and light-ion-induced reactions on nuclei at intermediate energies. Heavy ion interactions and nucleon-induced reactions are handled by using JAERI Quantum Molecular Dynamics (JQMD) [34], but for deuteron-, triton-, ^{3}He-, and ^{4}He-induced reactions in the intermediate energy, INCL4.6 is used. Additionally, the generalized evaporation and fission model (GEM) [35] is used to simulate the static stage of hadron-

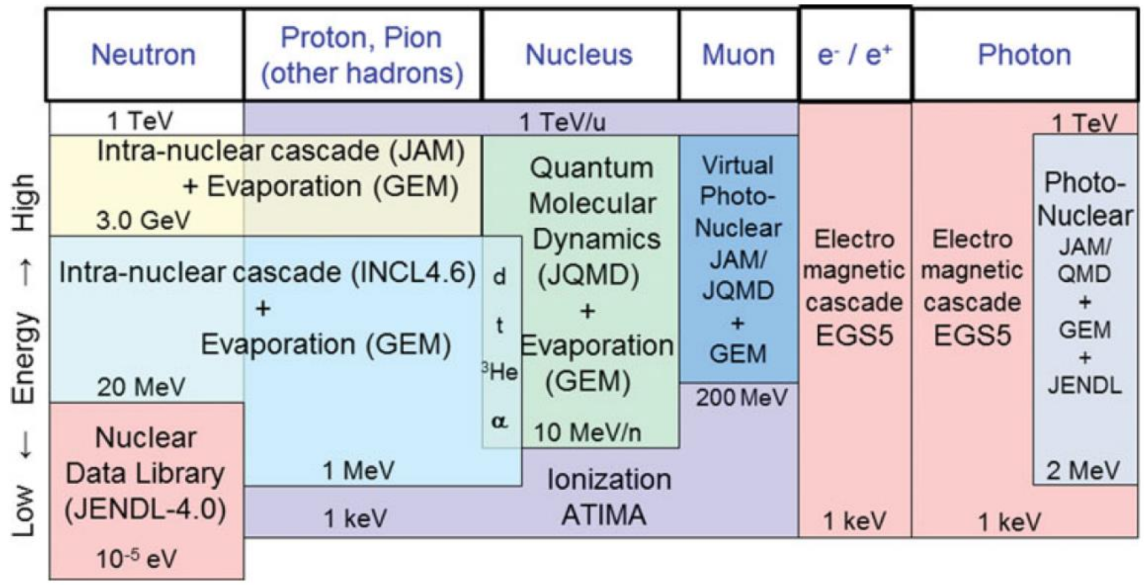

Figure 3.9. Map of PHITS physics models and data libraries in PHITS version 2.88 [36].

and nucleus-induced reactions. For the PHITS simulations presented in this work, a cutoff energy at 1 keV for protons, neutrons, photons, and heavy ions and a cutoff energy at 100 keV for electrons and positrons were used. Two geometry configurations were used in PHITS for each beam and target combination system conducted in November 2016 and November 2017 experiments.

The first configuration was a to-scale target room design ("room simulation"), where the room entrance, tunnel, rail system, detector stands, beam dump, floor, ceiling, and walls were considered. The modeled geometries of the upstream and downstream targets, veto detectors, and the liquid scintillators were identical to the experimental dimensions. To consider reactions of particles with air, the target room was filled with air. The liquid scintillator arrays (including the veto detector and the detector stand) were positioned according to their flight paths at 10°, 30°, 45°, 60°, 80°, and 135° with respect to the beam direction. The source term was set as a monoenergetic and monodirectional beam with a diameter of 2.5 cm bombarding on the center of the front face of the upstream target. The proton, deuteron, triton, helium-3, and helium-4 fluxes as a function of energy (#/source particle/MeV) were calculated by using the T-Cross tally in PHITS. In this tally, the fluxes of proton, deuteron, triton, helium-3, and helium-4 particles crossing the aluminum housings of the liquid scintillators and then entering the active detector volumes were calculated. PHITS simulation results were then normalized by the solid angle of each liquid scintillator to generate double-differential thick-target charged particle yields which were in units of # / (source particle-steradian-MeV).

The ring-type detectors were modeled in the second configuration ("ring simulation") because it is difficult to obtain good statistics for charged particles with the small detection crossing area in the room simulations. The ring-type detectors with the same width and depth to the active detector volume have the same distances and equivalent angles according to the experimental setup. While the target room geometry (e.g., the floor and walls) was not considered in the ring simulations, the upstream and downstream targets and six ring-type detectors were surrounded by air to take reactions between charged particles and air into account. The source term was set as in the room simulations. In the ring simulation, the upstream target geometry was simulated using squared geometry to better approach the experimental setup at 60° and 80° detectors. The T-Cross tally was also used to calculate proton, deuteron, triton, helium-3, and helium-4 fluxes crossing the air-filled region in front of ring-type detector and then entering the ring-type detector. The same simulation result normalization described above in the room simulations was utilized. The ring-type detectors and targets used in the ring simulations are illustrated in Figure 3.10.

The purpose of the room configuration was to compare with the ring configuration to make sure it was appropriate to use the ring configuration to get better statistic in the simulated results.

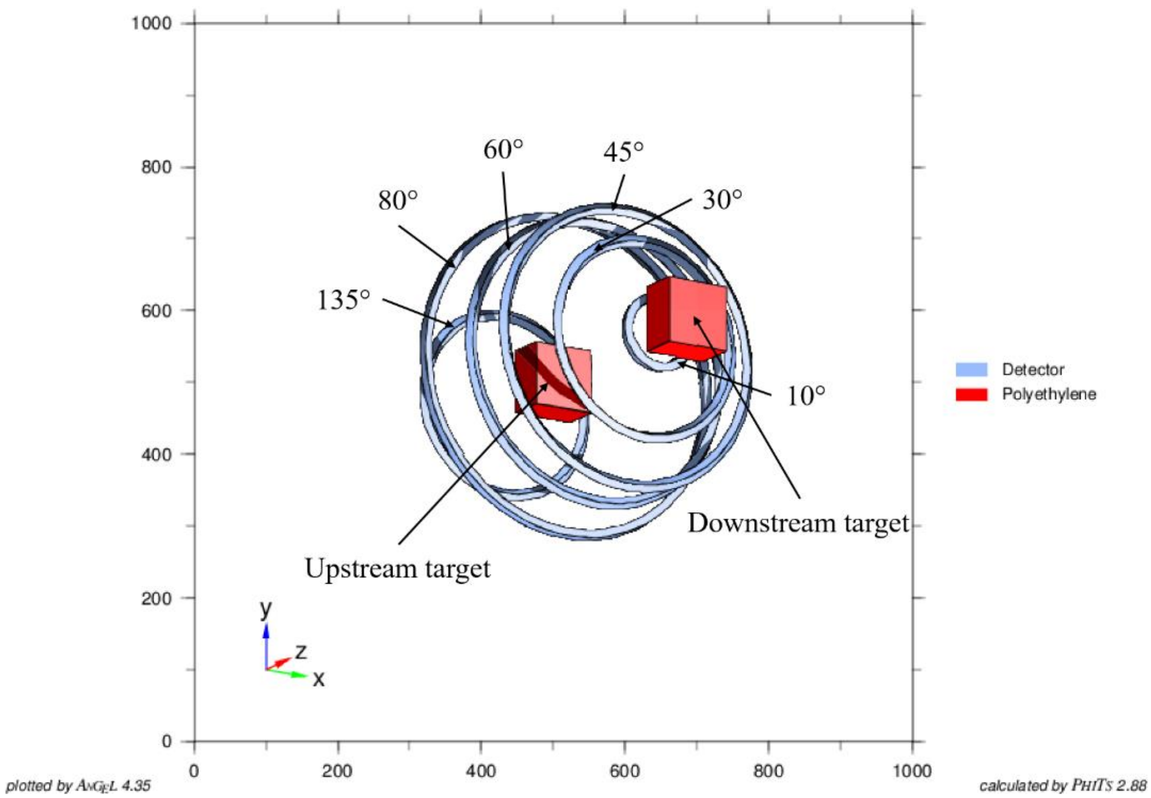

Figure 3.10. 3-dimensional image of PHITS ring-type detectors with HDPE targets.

3.3.2 MCNP

Additional Monte Carlo simulations were executed using Monte Carlo N-Particle Transport code (MCNP) for each beam and target combination system in November 2016 and November 2017 experiments to compare with PHITS ring simulations. The MCNP geometry configuration was similar to the PHITS room configuration. These MCNP simulations were first designed by Luis Castellanos, a former fellow graduate student in Department of Nuclear Engineering at UTK, and then were executed by Hunter Ratliff, another fellow graduate student in Department of Nuclear Engineering at UTK. The MCNP simulation results were normalized to generate double-differential thick-target charged particle yields in units of # / (source particle-steradian-MeV) for comparisons to PHITS room simulations and experimental results.

Figure 3.11 shows the map of particle types, energy ranges, and interaction physics used in MCNP6 [37]. The proposed regions indicated in Figure 3.11 are the potential features that might be incorporated into MCNP6. The proposed model will be similar to EGS for high-energy photons, electrons, and positions transportations. For low-energy charged particles, it will be similar to SRIM. As described in reference [37], MCNP utilizes Cascade-Exciton Model (CEM03.03) [38], [39] and the LANL version of the Quark-Gluon String Model (LAQGSM03.03) [39], [40] event generators. Both CEM and LAQGSM use their own models to describe the pre-equilibrium, evaporation, and fission reactions, but they use the same models to consider coalescence of nucleons into complex particles up to ^{4}He and Fermi breakup of excited or unstable nuclei with mass number less than 13 [37]. CEM was used for nucleon, pion and photon induced reactions up to 5 GeV for heavy mass targets and up to 1 GeV for light mass targets, while LAQGSM was used for heavy ion interactions up to approximately 1 TeV/n and photon induced interactions above 1.2 GeV, as well as reactions induced by projectiles not considered in other models [37]. Another default option used in MCNP6 was the ISABEL INC [41]. ISABEL was used for deuteron-, triton-, ^{3}He-, ^{4}He-, and antinucleon-induced reactions at energies up to 1 GeV/n [37].

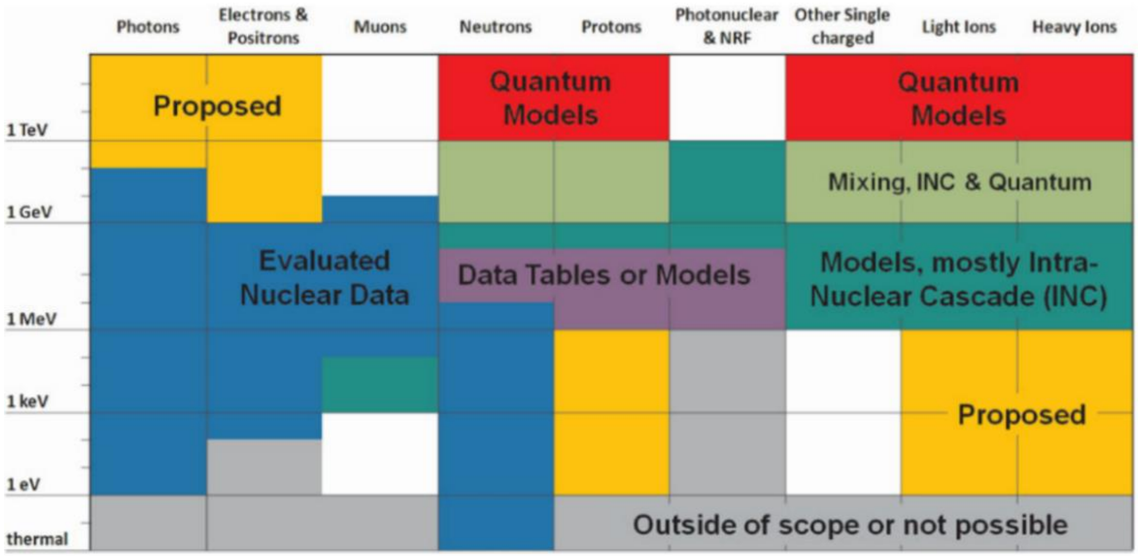

Figure 3.11. Map of MCNP6 particle types, energy ranges, and interaction physics [37].

CHAPTER FOUR
DATA ANALYSIS METHODOLOGY

4.1 Double-Differential Thick-Target Yield Analysis Methodology

The raw experimental data were converted and analyzed with ROOT Data Analysis Framework [42], which is developed by the European Organization for Nuclear Research (CERN). Each ROOT file included triggered event information in each run for the six liquid scintillator arrays. The information utilized in charged particle analysis was TDC (timing information), and QDC (charge deposition) of veto detectors and OLSs. This work focuses on secondary charged particle production measured by the liquid scintillators in the thick target measurements. To determine the double-differential thick-target (DDTT) secondary charged particle yields, a series of steps were required, including 1) good beam cut, 2) self-time gate, 3) charged and neutral particle separation, 4) charged particle identification, 5) time-of-flight calculation and energy conversion, 6) time walk and efficiency corrections, and 7) uncertainty calculation.

4.1.1 Good Beam Cut

Good beam cuts were used to select the valid beam particles that were directed along the center of the beam axis incident on the upstream target for each beam and target combination system. Good beam cuts were made by plotting the charge deposition in the S1 and S2 against each other and then drawing a graphical contour around the primary beam spot. An example of the good beam cut can be seen in Figure 4.1. The events that excluded by applying good beam cuts were 1) beam projectiles fragmented in the air column between the beam exit window and start scintillator tube (the lower left diagonal portion), 2) beam projectiles fragmented after hitting S1 but before arriving S2 (the horizontal portion), 3) two beam projectiles hit the beam start scintillators simultaneously and considered as a single event but the energy deposition was twice the amount (the upper

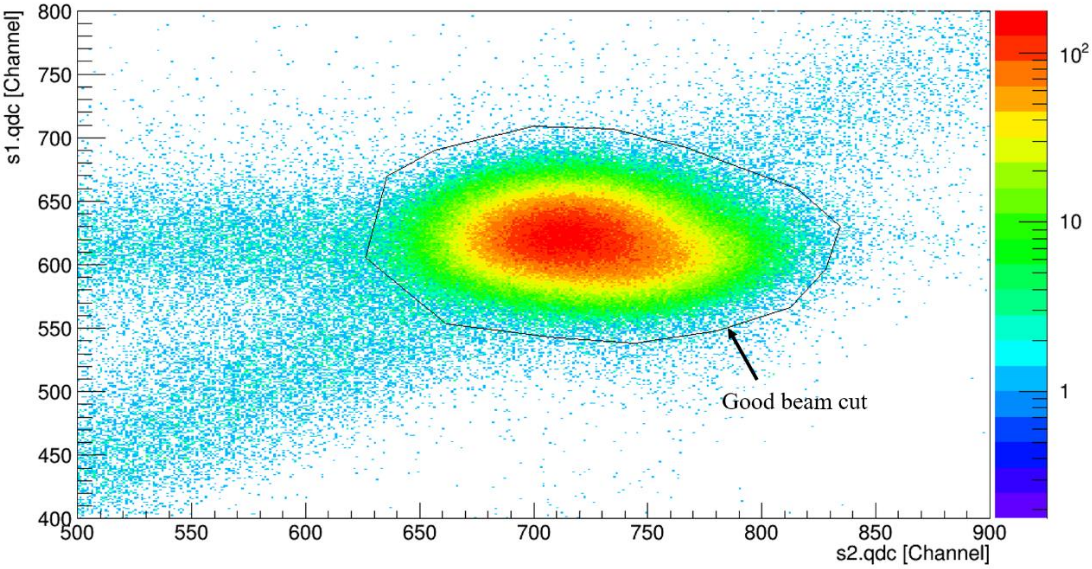

Figure 4.1. Charge deposition in the two start scintillators plotted versus each other for the 1470-MeV/n Fe on Al target. The contour drawn around the central spot was used to select the valid beam particle events that were directed along the center of the beam axis.

right portion), and 4) beam projectiles missed S1 but struck S2 since S1 had smaller cross sectional area.

4.1.2 Self-Time Gate

Events were triggered when charged and neutral particles were detected in the liquid scintillators. The signals from the OLS were used to generate a delayed timing signal which was then subsequently recorded in TDC histograms. Since the OLS signal also generated the start of TDC, the difference between the TDC "START" and delayed OLS "STOP" signals was fixed. Thus, any valid event from a detector would fall into a fixed position in each TDC histogram. Figure 4.2 shows the one-dimensional TDC histogram of the liquid scintillator at 10° for 1470-MeV/n Fe beam on Al target. "Self-time" gates selected the events that triggered in each liquid scintillator and in coincidence with the start signal fired by S1 and S2. By applying the self-time gates for each liquid scintillator, events that were recognized as mistimed or events that were triggered in one of the six liquid scintillators but did not set off the coincidence signal with the two start scintillators, which showed up outside the self-time peak in the TDC histogram, were ignored.

4.1.3 Charged and Neutral Particle Separation

Since both charged and neutral particles could set the coincidence trigger in the liquid scintillators, the separation of charged and neutral particles is necessary. Separating between charged and neutral particles can be achieved by examining the QDC spectrum of the front veto detector that covered the front face of the liquid scintillator. Based on the neutral particle interaction mechanism in thin materials, the probability that neutral particles interact with the front veto detector is significantly lower than the probability that charged particles interact with the front veto detector [43]. In general, the ratio of neutrons to protons detected by the veto detector is 1 to 100. Also, the probability that neutrons interact with the front veto detector and produce protons which are then detected by the following OLS detector is only around 2%. Figure 4.3 shows the one-dimensional QDC histogram of the front veto detector at 10° for 400-MeV/n C beam on HDPE target. The peak on the left part of the QDC spectrum is the non-zero pedestal peak, which is occupied

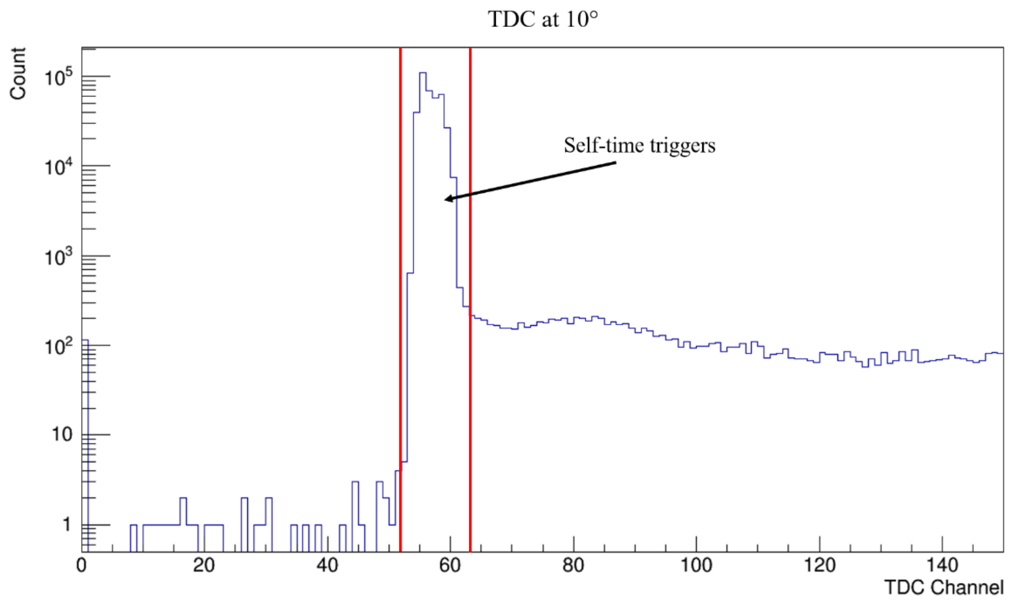

Figure 4.2. Liquid scintillator TDC spectrum at 10° for the 1470-MeV/n Fe on Al target. The lines shown were the self-time gate used to select self-time triggered events.

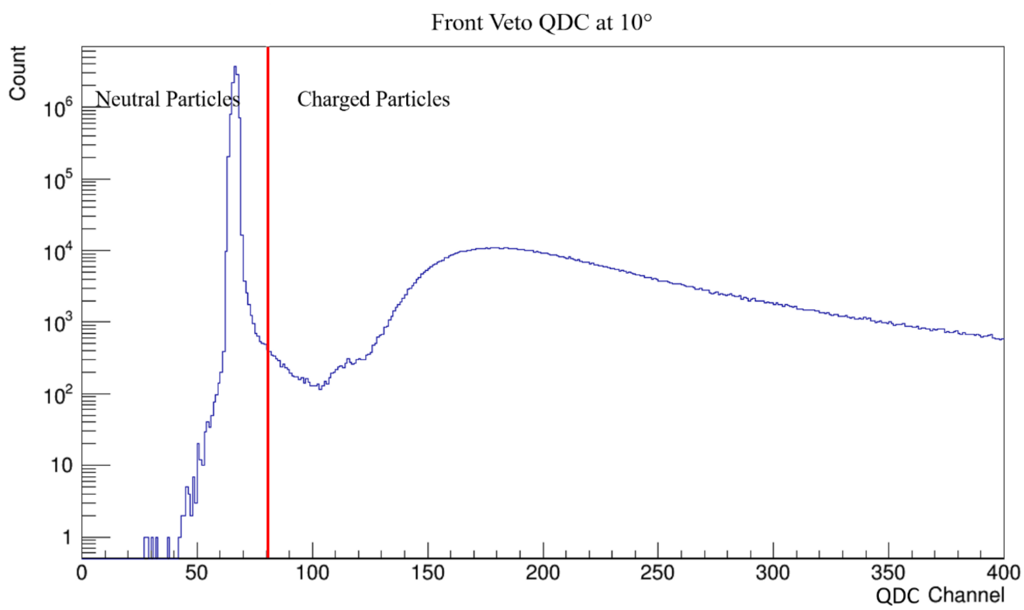

Figure 4.3. Front veto detector QDC spectrum at 10° for the 400-MeV/n C on HDPE target. The line shown was the threshold used to separate charged and neutral particles.

by neutral particle events [6], and the location of the non-zero pedestal peak depends on the electronic noise processing [43]. Therefore, those events to the right of the pedestal peak were the results of charged particles. Any event to the right of the pedestal peak and then was detected by the organic liquid scintillators was a valid charged particle event. As described earlier, this work focuses on secondary charged particle production, so that events above a certain threshold of the veto detector QDC signal were kept.

4.1.4 Charged Particle Identification

After identifying charged particle events, the energy deposited in organic liquid scintillator versus S1 TDC information (time-of-flight (TOF) technique) is considered to identify and separate charged particle species. Figure 4.4 shows a plot of energy deposition (y-axis) versus TOF (x-axis) for 400-MeV/n C beam on HDPE target at 10°. In that plot, the flight time increases from right to left, which means charged particle energy decreases from right to left. Each curve represents different charged particle species and the peak point of each curve is the "punch through point". The punch through point represents the maximum full energy of a charged particle that can deposit into a liquid scintillator detector as the charged particle ranges out in the active detector volume. Thus, events to the left of the punch through point represent that charged particles stop in the detector and fully deposit their energy into the detector, and those events to the right of the punch through point represent that charged particles penetrate the active detector volume. Isotopes with similar TOFs will have similar velocities (similar energies per nucleon). Additionally, heavier charged particles will have higher total energies and can deposit more energy in a detector, resulting in peaks locating in higher energy deposition channel numbers (y-axis).

Charged particle species that produce the well-defined lines in the TOF plots can be identified by comparing their punch through points. The proton energy at the punch through point in the 12.7 cm long organic liquid scintillator can be interpolated from range tables provided by NIST [44]. To calculate the energy per nucleon of other charged particle

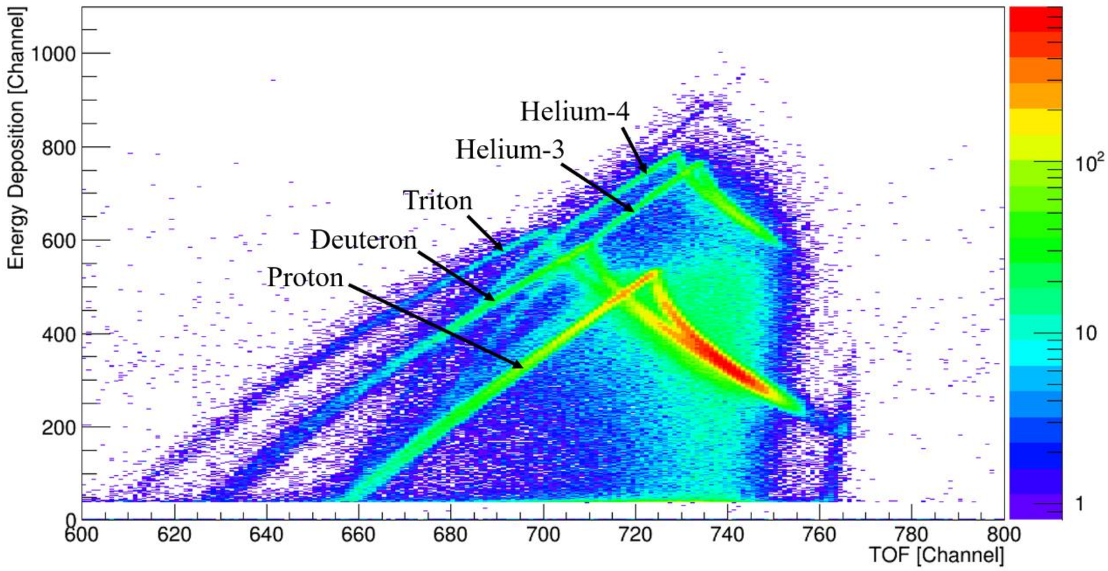

Figure 4.4. Total energy deposition in liquid scintillation detector versus time-of-flight for 400-MeV/n C beam on HDPE target at 10°. Well-defined lines corresponding to p, d, t, He-3, and He-4 events in the detector are indicated.

species at the punch through point, equation 4.1 was used, where $\left(R_{\rho}\right)_{i}$ is the range (g/cm^2) of ion with mass (A) and charge number (Z).

$$\left(R_{\rho}\right)_{i} = \left(R_{\rho}\right)_{proton} \times \left(\frac{A}{Z^2}\right)_{i} \tag{4.1}$$

After identifying different charged particle species, further separation between those ions were required to produce the double-differential thick-target yield for each ion. As illustrated in Figure 4.5, different charged particles overlap with each other at some points. To separate Z=1 and Z=2 charged particles, veto detector TOF spectrum was first utilized, as shown in Figure 4.6 (a). Figure 4.6 (a) is a 2-dimensional histogram of energy deposition in veto detector versus time-of-flight for 400-MeV/n C beam on HDPE target at 10°. There are two clear separated areas in the veto detector TOF spectrum, which are Z=1 charged particles (lower left portion) and Z=2 charged particles (upper right portion). Applying the graphical contour cuts around each of these two areas to the liquid scintillator TOF spectrum allows separation between Z=1 and Z=2 charged particles, as shown in Figure 4.6 (b) and (c). However, veto detector TOF cut method could not separate isotopes.

After separating charged particles with different atomic numbers (Figure 4.6 (b) and (c)), the pulse shape discrimination (PSD) method can be used to further separate intersections between isotopes. As illustrated in the study conducted by Kurosawa et al. [22], PSD method utilize the energy loss (*dE/dx*) differences in the OLS between different charged particles. The energy loss (*dE/dx*) of the charged particle creating the signal in the OLS affects the pulse height output of the OLS as a function of time. Charged particles with energies that stop in the OLS have increasing charge deposition in the slow components of the OLS when the *dE/dx* increases. The charged particles with energies that can punch through the OLS have less charge deposition in the slow components of the OLS than those charged particles stop in the OLS since those faster charged particles have smaller *dE/dx*. This feature creates a larger charge deposition collected in the short gate from those

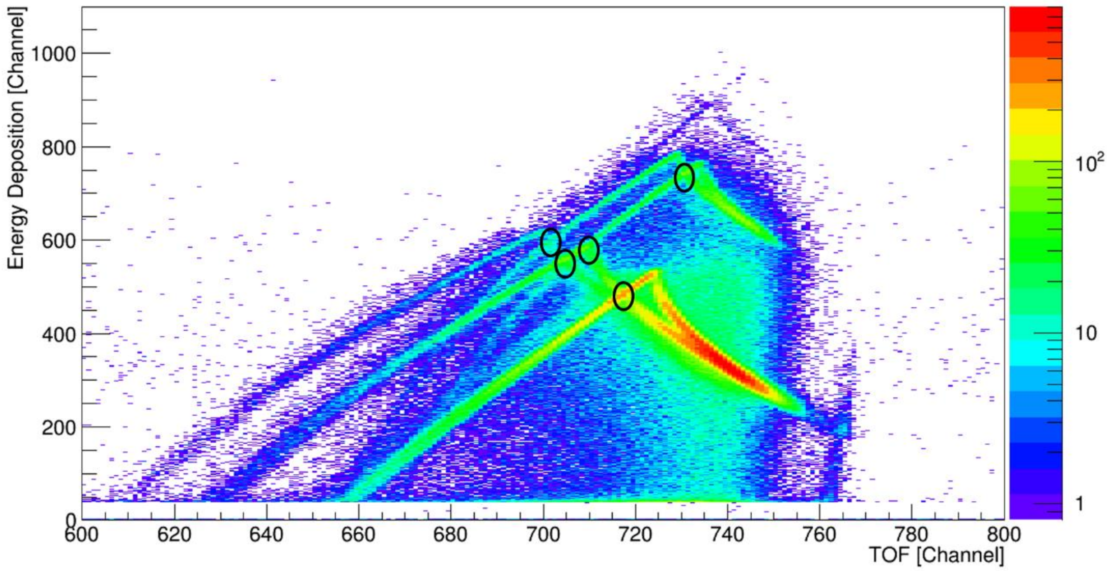

Figure 4.5. Liquid scintillator TOF spectrum with overlapped points shown for 400-MeV/n C beam on HDPE target at 10°.

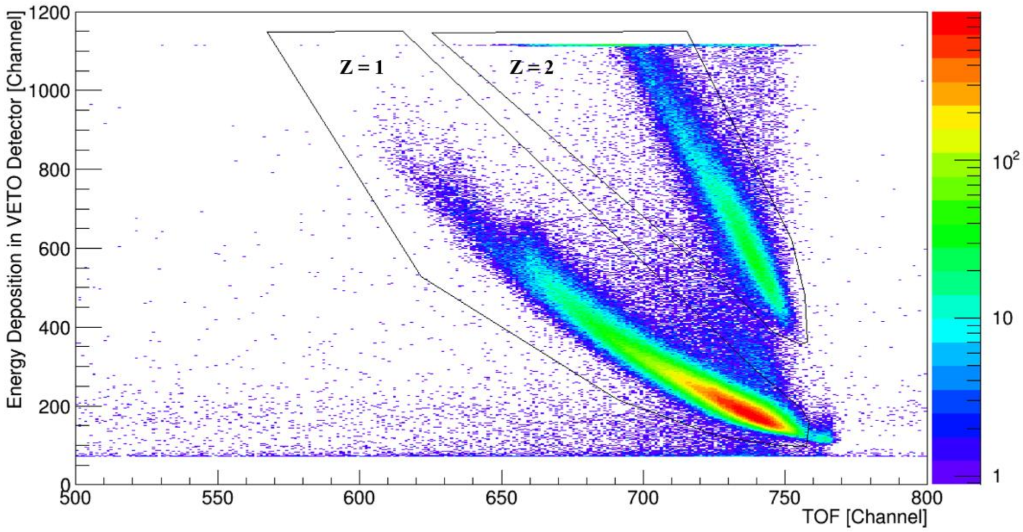

a)

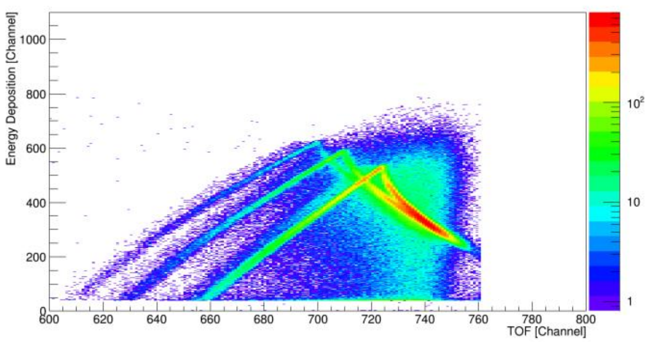

b)

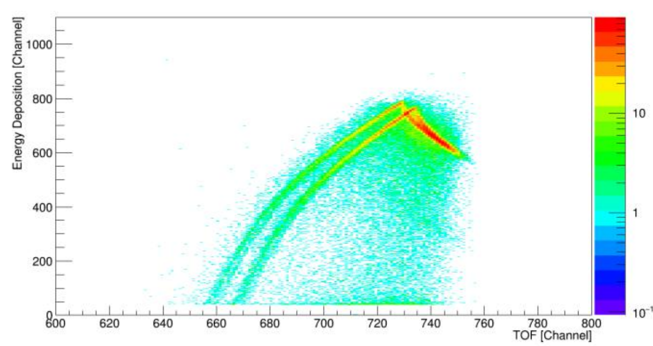

c)

Figure 4.6. (a) Energy deposition in veto detector versus time-of-flight for 400-MeV/n C beam on HDPE target at 10°. The contours showed in (a) were applied to liquid scintillator TOF spectrum (Figure 4.5) to separate Z=1 and Z=2 charged particles, which are shown in (b) and (c) accordingly.

charged particles stopping in the OLS [22]. The short gate was the shorter charged integration timing gate utilized in the PSD module, which was described in section "3.2 Data Acquisition System".

Therefore, the PSD method in this study is based on the charge deposition differences between integration over the first 20 to 35 ns of the signal (short gate) and over the full live time (200 ns) of the signal (long gate) created by the PSD module. A 2-dimensional histogram of Z=1 particle PSD for 400-MeV/n C beam on HDPE target at 10° is presented in Figure 4.7 (a). As shown in Figure 4.7 (a), the upper line is the charged particles that punched through the OLS and the lower line is the charged particles that stopped in the OLS. The PSD graphical cuts were used to separate charged particles that stopped in or punched through the OLS so that the intersections between isotopes can be resolved. Figure 4.7 (b) and (c) show Z=1 isotope separation after applying the PSD graphical cuts.

With veto detector TOF graphical cuts and PSD graphical cuts, the liquid scintillator TOF spectra for proton, deuteron, triton, helium-3 and helium-4 particles can be obtained separately by assigning charged particle events to the correct ion species at overlapped regions and then making the graphical contours around each ion line. The charged particle events selected by these graphical cuts were converted to one-dimensional S1 TDC histograms to generate charged particle counts versus TOF channel number histograms for further TOF to energy conversion.

4.1.5 Time-of-Flight Calculation and Energy Conversion

The TOF technique not only helps the identification between different charged particle species but also allows for conversion from TOF to energy. Measured TOF spectra were binned into histograms with the calibrated TDC channel width of 0.251 ns. The calibrated TDC channel width was determined at the end of November 2017 experiment by sending signals to the data acquisition system and adding known amount of timing delay repeatedly.

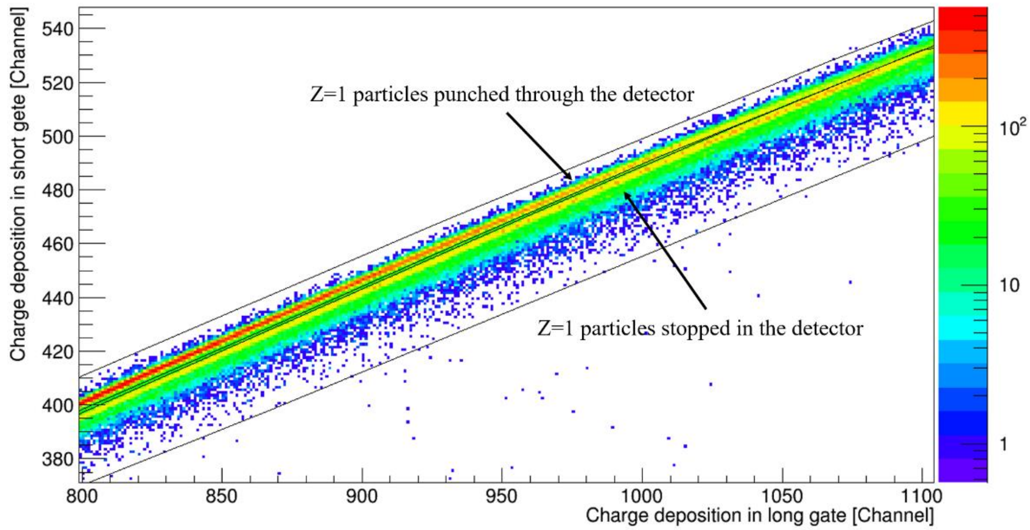

a)

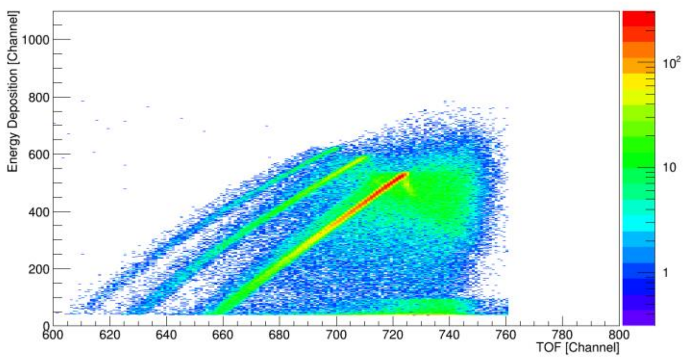

b)

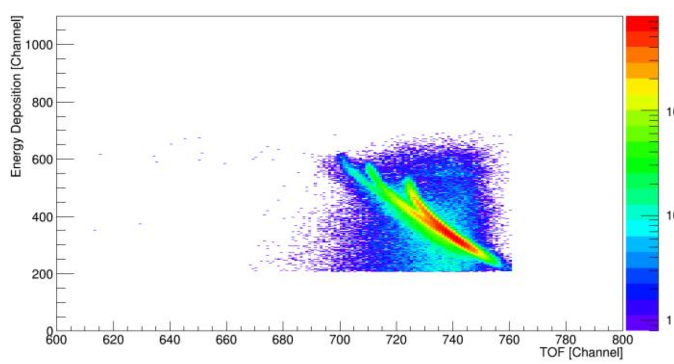

c)

Figure 4.7. (a) Z=1 particle PSD for 400-MeV/n C beam on HDPE target at 10°. The contours showed in (a) were applied to liquid scintillator TOF spectrum (Figure 4.6 (b)) to further separate isotopes' overlapped points, which can be seen in (b) and (c).

The known amount of timing delay and the TDC channel numbers recorded created a calibration curve. The linear fitting slope of this curve is the calibrated TDC channel width, which is illustrated in Figure 4.8.

The TOF values for each channel number can be calculated by using prompt gamma peak channel as a reference timing point and using the flight paths between the front face of each active OLS volume and the middle of the target (Table 3.4). Prompt gamma peak channel information for each beam and target combination system was identified by Hunter Ratliff, a fellow graduate student in Department of Nuclear Engineering at UTK. Since the prompt gamma park channel number and the calibrated TDC channel width (0.251 ns) are known, the TOF values can be calculated with the following equation:

$$TOF_{ch} = \left(tdc_{ch\_\gamma} - tdc_{ch}\right) \times 0.251 + \frac{d}{c}, \tag{4.2}$$

where tdc_{ch_γ} is the prompt gamma peak channel number, tdc_{ch} is the channel number in question, d is the flight path (cm) for each liquid scintillator, and c is the speed of light (30 cm/ns). Figure 3.8 shows proton time-of-flight channel spectrum and the identified prompt gamma peak channel number for the 400-MeV/n C on HDPE target at 10°.

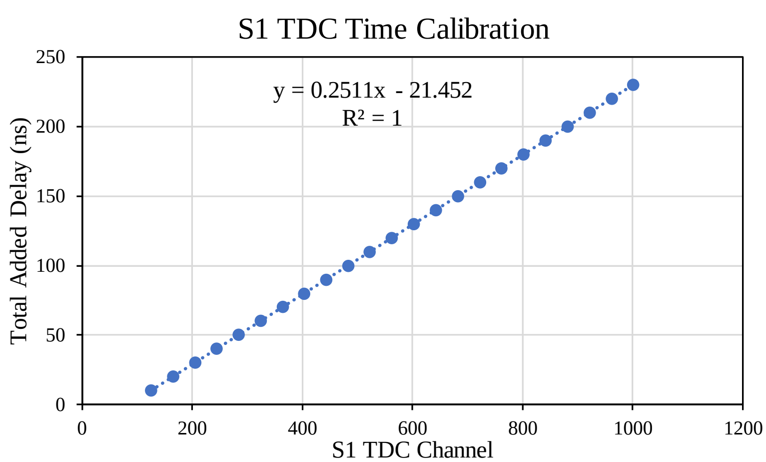

Figure 4.8. S1 TDC calibration curve.

For the purpose of generating double-differential thick-target secondary charged particle yield spectra, the TOFs need to be converted to energies at the point of charged particles entering the active volume of the liquid scintillators. The energy loss as the secondary charged particles penetrate materials before arriving the detector, such as the upstream target, the air column between the upstream target and the detector, the veto detector, and the OLS's aluminum housing, needs to be considered. The energy loss computer code was first written by Luis Castellanos, a former fellow graduate student in Department of Nuclear Engineering at UTK. The computer code was then modified to be able to apply to this study. The modifications included the implementation of Al+HDPE hybrid target, which complicated the energy loss calculations at the interface of Al and HDPE materials, and also the consideration of different assumed production points according to beam projectile's range in three types of targets (Al, HDPE, and Al+HDPE), which will be discussed in the following paragraph.

This code takes all the materials that the secondary charged particles produced in the upstream target at their production points will traverse into consideration. The flight paths from the secondary charged particle production point to the front face of the active OLS volume were divided into thousands of distance steps (*dx*). The input energies of each charged particle type considered in this code was from the initial secondary charged particle energy that certain type of secondary charged particle has a range roughly equal to the amount of the upstream target material up to 1000 MeV/n. The time for each secondary charged particle to transport through each distance step was calculated, and then the new particle energy and the new stopping power (*dE/dx*) were calculated at the end of each distance step. The code kept calculating until the secondary charged particle arrived the front face of the active OLS volume, and then the TOF value and the final energy were recorded. These calculations were repeated for protons, deuterons, tritons, helium-3, and helium-4 produced from three assumed production points for each liquid scintillator, and each upstream target material and thickness. The three assumed production points are the beginning, the middle, and the end of the beam projectile's range in the target if beam projectiles stop in the upstream target. If beam projectiles penetrate the upstream target, the three assumed production points are the middle, the upstream surface, and the downstream surface of the target. The TOF calculations of the three assumed production points were later applied to the energy uncertainty calculation.

The code calculations generated TOF versus energy (charged particle's total energy when it arrives the front face of the active OLS volume) tables for each ion from three assumed production points. These data tables allowed the double-differential thick-target secondary charged particle yields versus energy spectra to be produced.

4.1.6 Time Walk and Efficiency Corrections

In the TOF measurements, the constant fraction discriminator (CFD) timing outputs were affected by the amount of charge deposition in the signal, which caused events with more charge deposition having incorrectly faster TOF values (time walk). The time walk correction procedure was developed by Heilbronn *et al.* [45]. The time walk correction method implemented in ROOT was completed by Luis Castellanos [27] and Matthew Beach, a collaborator on the thick GCR shielding project.

Another correction applied to the measured results was the energy-dependent charged particle detection efficiency in the liquid scintillators since the OLS TOF graphical contours drawn around each ion line only selected the charged particle events having a complete energy deposition. The efficiency correction factor's calculation was conducted by Luis Castellanos [27] using PHITS versions 2.82 and 2.88. The simulation was that monoenergetic planar source particles bombard on a cylindrical xylene encased by Al, which is a similar geometry to the active liquid scintillator volume. In the simulation results, the fraction of events that produced a complete energy deposition was used as the efficiency correction factor for that input source particle energy.

4.2 Uncertainty Calculations for Experimental DDTT Yields

4.2.1 Statistical Uncertainties

The statistical uncertainties in the experimental double-differential thick-target charged particle yields were from the number of counts measured in that energy bin. The statistical uncertainties were calculated by taking the square root of counts in each energy bin in ROOT. They were then divided by the particle counts in that bin to get fractional uncertainties. After getting fractional uncertainties, the data would be rebinned to achieve a predetermined statistical uncertainty criterion. In general, statistical uncertainties varied by detector angle, energy, beam projectile, and the upstream target thickness. In this study, the rebinning process would continue until the fractional statistical uncertainty was below 10%. For the larger angles (60°, 80°, and 135°), the statistical uncertainties were not able to achieve this criterion at times due to the lack of counts. However, within those results which could not achieve the criterion, most of them still had statistical uncertainties below 20%. Table 4.1 shows a summary of the median fractional statistical uncertainties for experimental charged particle results.

Table 4.1. Median fractional statistical uncertainties for experimental charged particle results.

Secondary Particle	Detector (angle)					
	10°	30°	45°	60°	80°	135°
Proton	0.033	0.045	0.060	0.070	0.130	0.138
Deuteron	0.069	0.103	0.133	0.148	0.317	
Triton	0.108	0.147	0.224	0.382		
Helium-3	0.094	0.243				
Helium-4	0.065	0.419				

4.2.2 Systematic Uncertainties

The systematic uncertainties resulted from the normalization of converting counts to the double-differential thick-target yields for units of # / (source particle-steradian-MeV). The systematic uncertainties included uncertainties in solid angle, graphical cuts, and charged particle detection efficiency.

The solid angle uncertainty came from the uncertainty of the charged particle production point in the upstream target. The three assumed production points, mentioned in section "4.1.5 Time-of-Flight Calculation and Energy Conversion", had different flight paths to the assumed detection point. The assumed detection point was the center of the front face of the active OLS volume. The solid angles were calculated for these three flight paths and the true solid angle was the one calculated using the middle production point. The fractional difference of solid angles for the upstream and downstream production points was calculated. The solid angle uncertainties ranged from 0.2 to 15.9%.

The graphical cut uncertainty came from the subjective judgement with which the graphical contour cuts were made, including the good beam cuts and OLS TOF cuts for each ion. Therefore, two sets of the good beam cuts and the charged particle identification cuts were made for each beam and target combination system. These two sets of graphical cuts went through the same analysis process. Then, the percent differences between two double-differential thick-target yields for each energy bin were calculated and were used as the graphical cut uncertainties for each energy bin. Approximately 90% of the experimental data presented in this dissertation had the graphical cut uncertainty below 20%. Most of the data point with graphical cut uncertainty over 20% were those points at lowest energy bin. Since the rebinning process started from the highest energy bin, the uncertainty of the lowest energy bin was generally the worst. Table 4.2 shows a summary of the median fractional graphical cut uncertainties for experimental charged particle results.

Table 4.2. Median fractional graphical cut uncertainties for experimental charged particle results.

Secondary Particle	Detector (angle)					
	10°	30°	45°	60°	80°	135°
Proton	0.012	0.012	0.013	0.017	0.026	0.016
Deuteron	0.016	0.019	0.024	0.033	0.072	
Triton	0.016	0.013	0.021	0.127		
Helium-3	0.015	0.009				
Helium-4	0.012	0.041				

The charged particle detection efficiency uncertainty was the statistical uncertainty of the charged particle detection efficiency factor from the PHITS simulations mentioned in section “4.1.6 Time Walk and Efficiency Corrections”. The charged particle detection efficiency uncertainties for each charged particle were below 0.2%.

4.2.3 Energy Uncertainties

The energy uncertainty is related to the uncertainty of the secondary charged particle production point in the upstream target. Since the exact production point is unknown, the TOF to energy conversions from three assumed production points in the energy loss code were applied to quantify the energy uncertainty. The three assumed production points, mentioned in section “4.1.5 Time-of-Flight Calculation and Energy Conversion”, had different flight paths to the assumed detection point, which means charged particles produced at different production points traversed different amount of the upstream target. This resulted in three TOF to energy conversion tables. The TOF to energy conversion calculated using the middle production point was considered true TOF to energy conversion. The other two sets of TOF to energy conversion tables were then used to calculate the percent differences between true energy as the energy uncertainty per energy bin. Table 4.3 presents a summary of the median fractional energy uncertainties for experimental charged particle results.

Table 4.3. Median fractional energy uncertainties for experimental charged particle results.

Secondary Particle	Detector (angle)					
	10°	30°	45°	60°	80°	135°
Proton	0.053	0.045	0.027	0.026	0.073	0.037
Deuteron	0.051	0.043	0.025	0.024	0.093	
Triton	0.041	0.034	0.022	0.031		
Helium-3	0.049	0.043				
Helium-4	0.043	0.037				

4.3 Dose Equivalent Calculations

After determining the double-differential thick-target (DDTT) secondary charged particle yields, the dose equivalents were then calculated based on the experimental yield results. Since the double-differential thick-target secondary charged particle yield is in units of # / (source particle-steradian-MeV), the first step was converting DDTT yield to fluence in units of # / (source particle-cm^2) for each secondary charged particle measured. Then, using the following equation to calculate the absorbed dose per energy point in the fluence spectrum for each charged particle type ($D(Z,E)$).

$$D(Z,E) = \frac{LET(Z,E)}{\rho} \times \Phi(\mathrm{Z,E}), \tag{4.3}$$

where the units are D (Gy), LET ($keV/\mu m$), ρ (g/cm^3), and Φ (# / cm^2).

With the absorbed dose per energy point for each charged particle type data, the dose equivalent ($H(Z,E)$) was calculated by multiplying the quality factor (Q) with the absorbed dose, as shown below:

$$H(Z,E) = D(Z,E) \times Q. \tag{4.4}$$

In this study, three quality factors were taken into consideration, including ICRP 60 quality factor ($Q(LET)$), and NASA quality factors for solid tumors and leukemia. The relationship between ICRP 60 quality factor and LET is given in Table 4.4.

The NASA quality factor (Q_{NASA}) can be derived using the equations shown below with LET in units of $keV/\mu m$:

$$Q_{NASA} = \left(1 - P(Z,E)\right) + \frac{6.24 \times \left(\Sigma_0/\alpha_\gamma\right)}{LET} \times P(Z,E), \quad (4.5)$$

where

$$P(Z,E) = \left(1 - e^{\frac{-(Z^*/\beta)^2}{\kappa}}\right)^m \times P_{TD}, \quad (4.6)$$

$$Z^* = Z \times \left(1 - e^{-\left(\frac{1.25\times\beta}{Z^{2/3}}\right)}\right), \quad (4.7)$$

$$P_{TD} = \left(1 - e^{-\left(\frac{E}{E_{TD}}\right)}\right), \quad (4.8)$$

where Σ_0, α_γ, m, κ, and E_{TD} are the parameters derived from model [2]. Table 4.5 summarizes the model parameters selected to generate the NASA quality factors for solid tumors and leukemia for charged particles with $Z \leq 4$ [20].

Table 4.4. The quality factor in ICRP 60 [1].

$LET\ (keV/\mu m)$	$Q(LET)$
≤ 10	1
$> 10\ and\ \leq 100$	$0.32 \times LET - 2.2$
> 100	$300/\sqrt{LET}$

Table 4.5. Model coefficients for Q_{NASA} [2].

Coefficient	Solid cancers	Leukemia
	$Z \leq 4$	
E_{TD} (MeV/n)	0.2	0.2
α_{γ} (Gy^{-1})	6.24	6.24
Σ_0 (μm^2)	7000	1750
κ $(\frac{Z}{\beta})^2$	1000	1000
m	3	3

After calculating three quality factors for each energy point in each experimental fluence spectrum for each light charged particle, the dose equivalents for each energy point were able to be computed. The dose equivalent results presented in this thesis were integrated over the dynamic range of the energy spectra and then integrated over all the detection angles (10°, 30°, 45°, 60°, 80°, and 135°) to get the total dose equivalent for each secondary charged particle species measured per beam and target combination system.

CHAPTER FIVE
RESULTS AND DISCUSSION

5.1 Overview

The experimental double-differential thick-target (DDTT) proton, deuteron, triton, helium-3, and helium-4 yields for 39 systems of beam and target combinations (listed in Table 3.1) were measured at 6 angles (10°, 30°, 45°, 60°, 80°, and 135°). For 39 analyzed beam and target combination systems, some charged particle species were not detected in all detectors, or were observed but did not have enough particle counts to produce viable spectra. Protons were detected at all 6 angles. While deuterons were recognized at the angles not greater than 80°, tritons could be seen at 10° to 60°. On the other hand, helium-3 and helium-4 could only be possibly identified at 10° and 30°. The upper limit of analyzed charged particle energies is approximately 180 MeV/n for Z=1 particles and 200 MeV/n for Z=2 particles. The fractional statistical uncertainties for identified experimental charged particle yields are generally below 20% depending on charged particle species. In most cases, the statistical uncertainties increase at the larger detector angles.

A selection of DDTT light charged particle yield data are displayed in section "5.2 Comparisons Between Experimental and Simulated Double-Differential Thick-Target Light Charged Particle Yields" to showcase the comparison of experimental and simulated results. The rest of DDTT light charged particle yield data will be available from the Graduate School at Trace: Tennessee Research and Creative Exchange. The DDTT yield plots present the DDTT light charged particle yields as a function of particle's energy arriving the front face of the active OLS volume, with vertical error bars representing the statistical uncertainties of the measured results and horizontal error bars representing the energy uncertainties. Also, each plot includes the associated PHITS ring and MCNP room simulations for comparisons between experimental results and simulations. The Monte Carlo simulations do not include the error bars for the clarity of the comparisons in each plot. For PHITS ring simulations, the fractional statistical uncertainties for protons, deuterons, and tritons are generally below 10%, except for a few data points at larger detection angles (between 10 to 20%). Most of the PHITS simulated helium-3 results have fractional statistical uncertainties less than 20% but around 1% of the PHITS simulated helium-3 results at larger detection angles and low energy bins have fractional statistical uncertainties higher than 20%. For the PHITS simulated helium-4 results, the median fractional statistical uncertainties were less than 3% for 10° detector and were around 20% for 30° detector. A summary of the median fractional statistical uncertainties for PHITS ring simulations is shown in Table 5.1. On the other hand, since MCNP utilized the full room configuration, the fractional statistical uncertainties for MCNP simulations were generally higher than for PHITS simulations. The counting statistics for MCNP simulations are better at more forward angles. The median fractional statistical uncertainties for the MCNP simulated proton results are below 26% for all 6 angles. The median fractional statistical uncertainties for the MCNP simulated A>1 charged particle results are less than 29% at 10° detector. Also, for the MCNP simulated A>1 charged particles at angles greater than 10°, the median fractional statistical uncertainties are generally higher than 22%. Table 5.2 presents a summary of the median fractional statistical uncertainties for MCNP room simulations. Additionally, in each DDTT light charged particle yield plot, sometimes MCNP room simulations are not as smooth as PHITS ring simulations, which illustrates the main reason using ring geometry in PHITS is to get better statistics.

Table 5.1. Median fractional statistical uncertainties for PHITS ring simulations.

Secondary Particle	Detector (angle)					
	10°	30°	45°	60°	80°	135°
Proton	0.009	0.008	0.009	0.011	0.022	0.029
Deuteron	0.021	0.020	0.024	0.025	0.066	
Triton	0.043	0.070	0.081	0.078		
Helium-3	0.056	0.091				
Helium-4	0.027	0.204				

Table 5.2. Median fractional statistical uncertainties for MCNP room simulations.

Secondary Particle	Detector (angle)					
	10°	30°	45°	60°	80°	135°
Proton	0.041	0.060	0.074	0.089	0.213	0.257
Deuteron	0.145	0.228	0.309	0.339	0.991	
Triton	0.288	0.553	0.707	0.999		
Helium-3	0.251	0.619				
Helium-4	0.231	1.000				

A selection of proton and helium-4 dose equivalent results for measured DDTT light charged particle yields are displayed in section "5.3 Dose Equivalent Results". The rest of dose equivalent results for measured DDTT light charged particle yields will also be available from the Graduate School at Trace: Tennessee Research and Creative Exchange. Each dose equivalent plot shows the total dose equivalent integrated over angular distribution (where measured DDTT yields available) on the left y-axis and the ratio of dose equivalent values calculated by using $Q_{ICRP-60}$ to $Q_{NASA} Solid\ Cancers$ on the right y-axis as a function of the upstream target thickness. The error bars presented in these plots are the uncertainties of dose equivalents resulted from the energy uncertainty of each data point in the measured DDTT yields.

In the following sub-sections, section "5.2 Comparisons Between Experimental and Simulated Double-Differential Thick-Target Light Charged Particle Yields" includes the detailed discussion of carbon projectile systems and then follows with an overall discussion on the systematic trends of all DDTT light charged particle yield data analyzed for this work. Section "5.3 Dose Equivalent Results" presents the discussion of dose equivalent results for carbon projectile systems and also follows with an overall discussion on the systematic trends of all dose equivalent results calculated for this work.

5.2 Comparisons Between Experimental and Simulated Double-Differential Thick-Target Light Charged Particle Yields

5.2.1 DDTT Light Charged Particle Yields for Carbon Projectile Systems

The DDTT proton yield results for carbon projectiles are displayed in Figure 5.1 through Figure 5.9. The experimental DDTT proton yields have good agreement with the PHITS ring and MCNP room simulations in the spectral shapes for 400, 800, and 1500 MeV/n C projectiles on all three types of upstream target. The agreement in magnitudes varies from beam energy and target combination to beam energy and target combination. For all three energies of carbon projectiles on Al upstream target, the PHITS ring simulations over-predicted the magnitude of the proton yields by approximately 30-50% while the MCNP results are matched with the experimental proton yields fairly well or slightly underestimated the proton yields by about 20%. For all three C projectile energies on HDPE and Al+HDPE upstream target, the PHITS simulated results presented good agreement in spectral shape and matched the magnitude of the experimental proton yields or overestimated the proton yields by about 10-20%. Also, across three C projectile energies and three types of upstream target, MCNP room simulations predicted the proton yields relatively better than PHITS ring simulations at 135°. In general, the agreement between the experimental and simulated results improve with an increase in upstream target thickness for carbon projectiles on three types of upstream target, but there are some exceptions, such as 400 MeV/n carbon beam on Al+HDPE upstream target system. Also, the comparison of proton yields between the experimental and simulated results varies depending on the target thicknesses and materials. It seems that PHITS and MCNP simulations both overestimate proton yields most of the time but generally their spectral shapes agree with the experiments. This proton overestimation might be because the coalescence models incorporated into the cascade models in PHITS and MCNP do not coalesce enough. This might also affect the following complex light ion results.

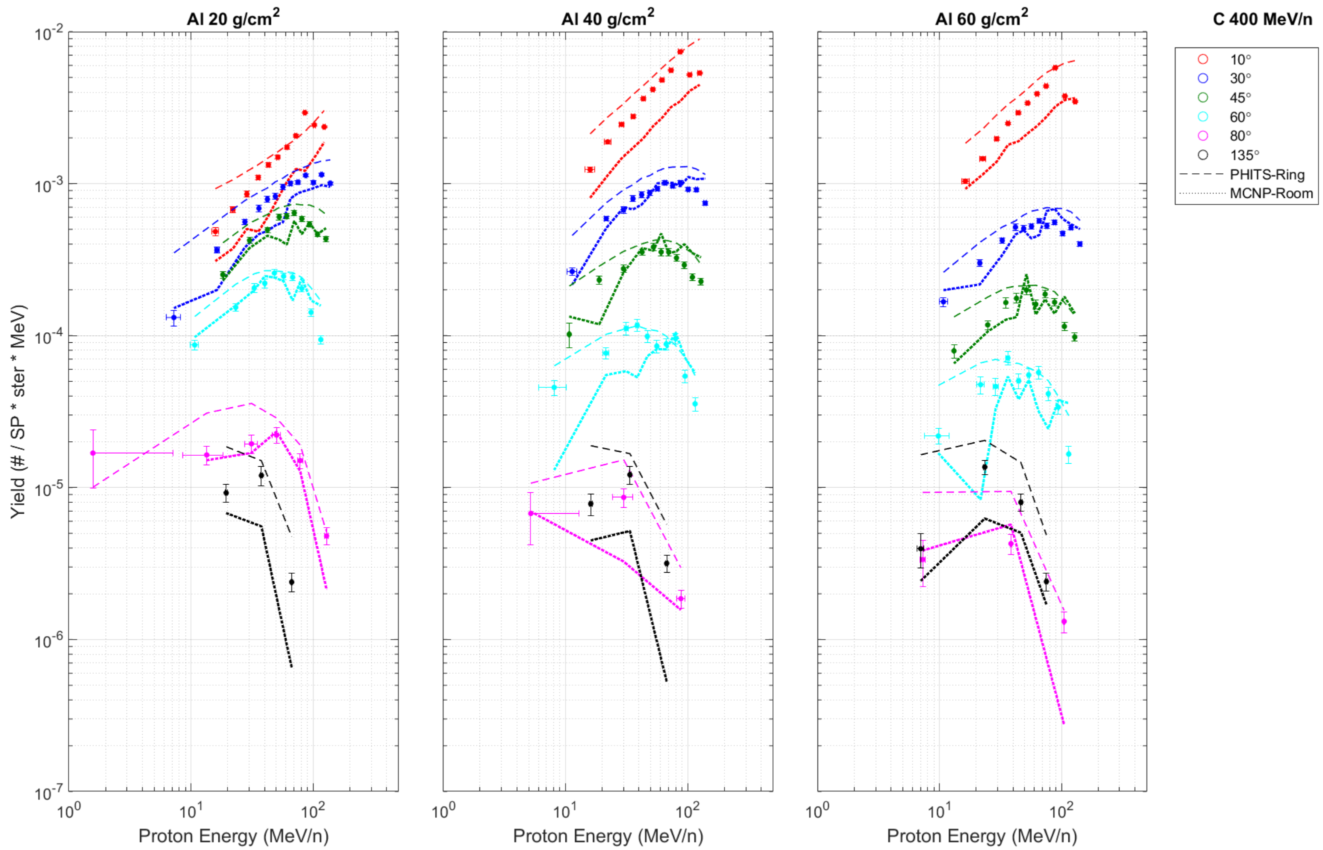

Figure 5.1. Double-differential thick-target proton yields for 400 MeV/n C beam on Al upstream target with associated PHITS ring and MCNP room simulations.

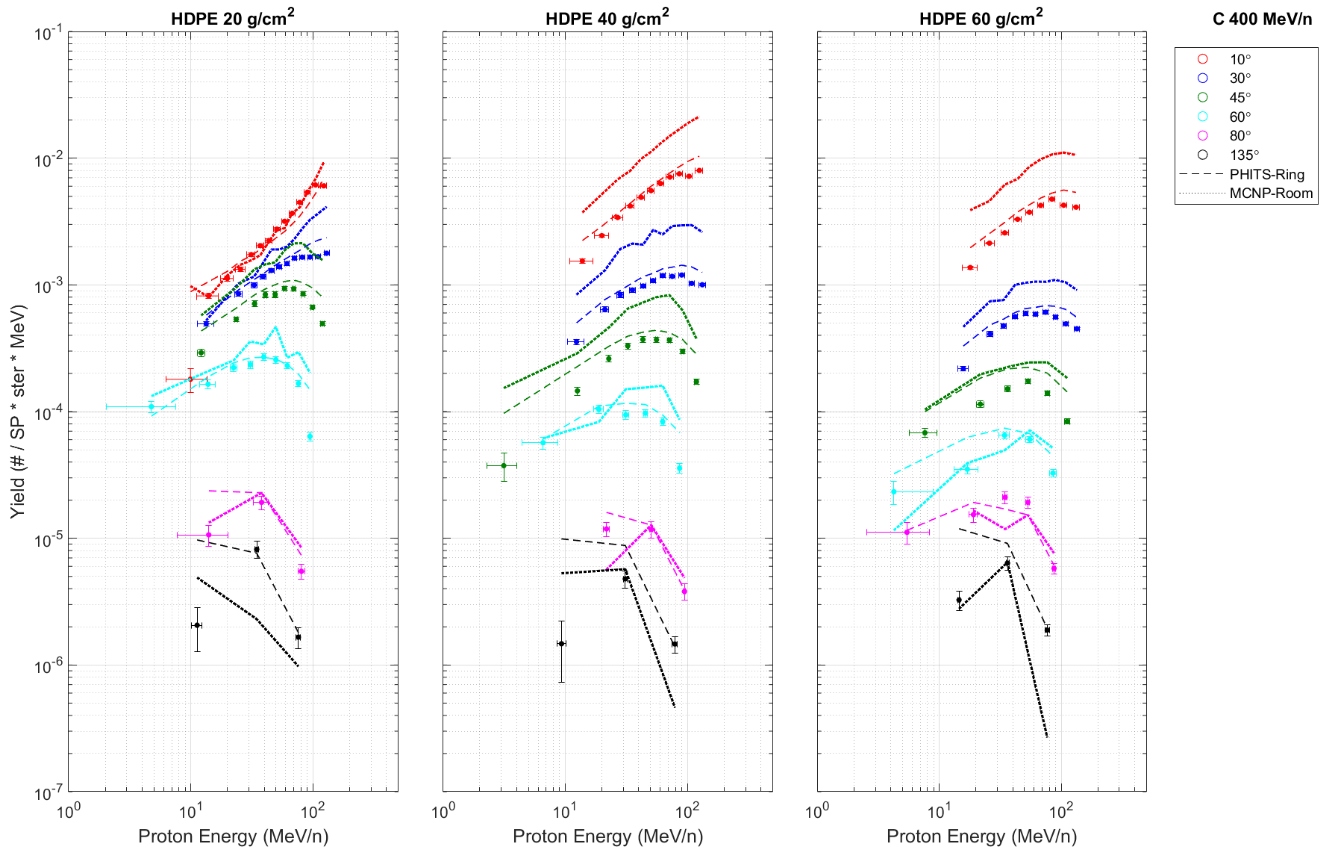

Figure 5.2. Double-differential thick-target proton yields for 400 MeV/n C beam on HDPE upstream target with associated PHITS ring and MCNP room simulations.

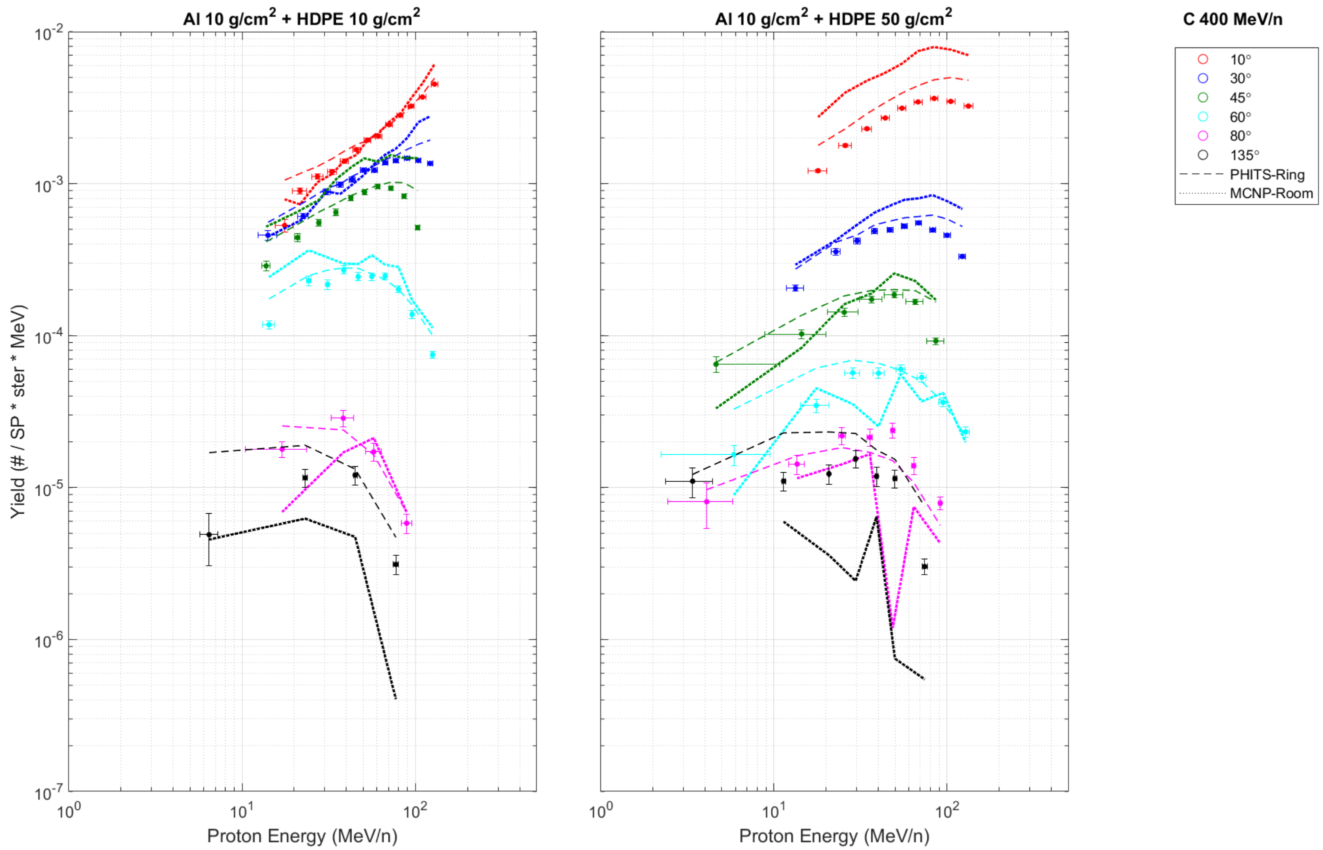

Figure 5.3. Double-differential thick-target proton yields for 400 MeV/n C beam on Al+HDPE upstream target with associated PHITS ring and MCNP room simulations.

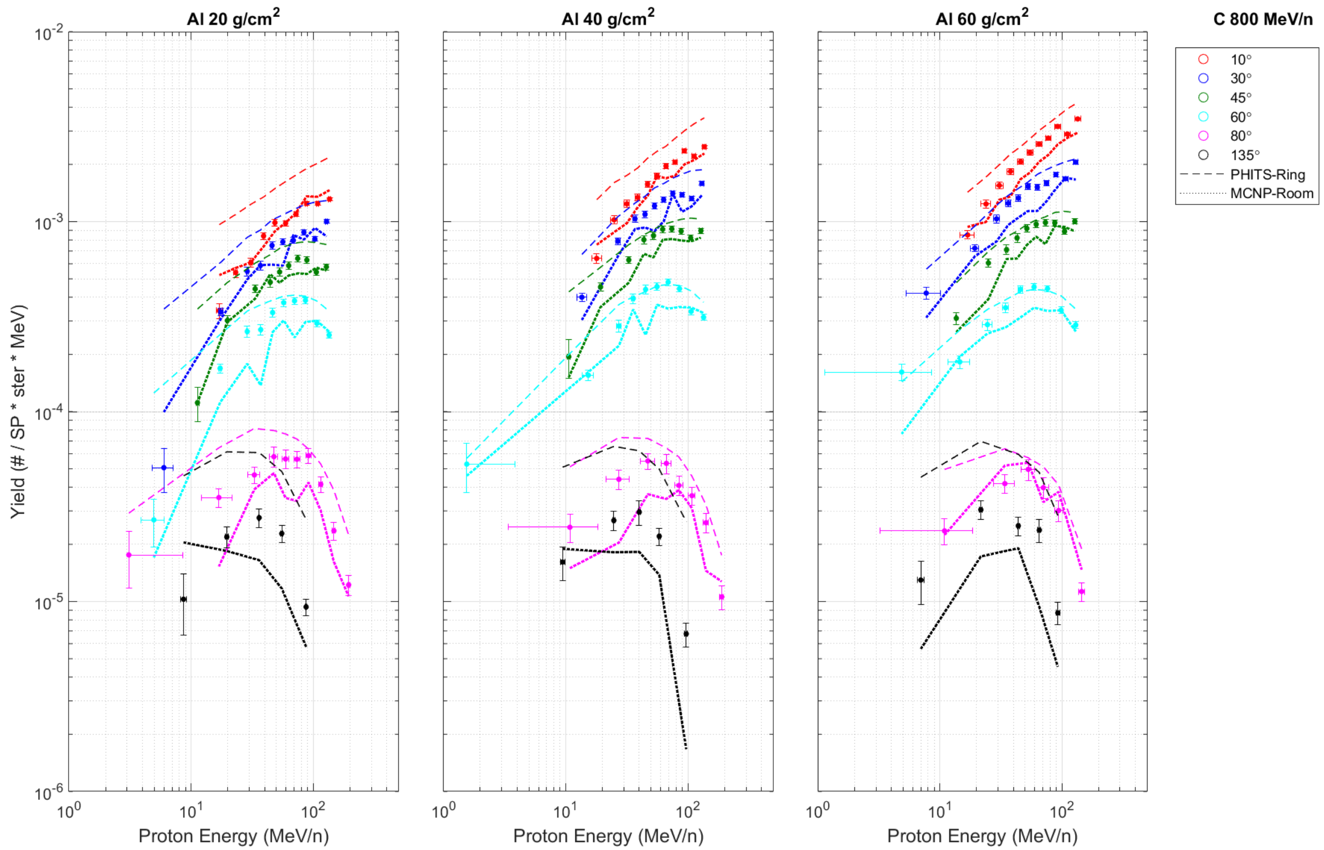

Figure 5.4. Double-differential thick-target proton yields for 800 MeV/n C beam on Al upstream target with associated PHITS ring and MCNP room simulations.

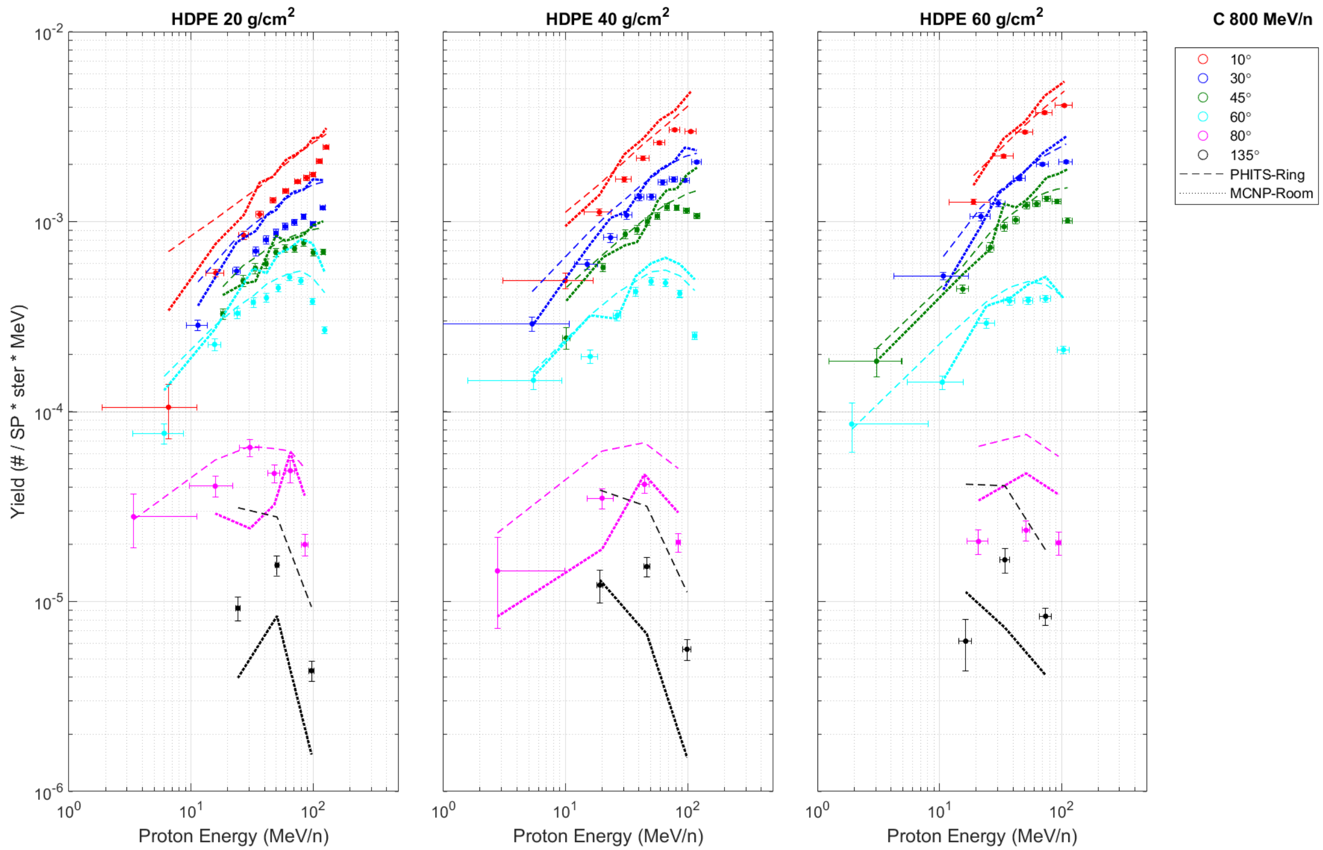

Figure 5.5. Double-differential thick-target proton yields for 800 MeV/n C beam on HDPE upstream target with associated PHITS ring and MCNP room simulations.

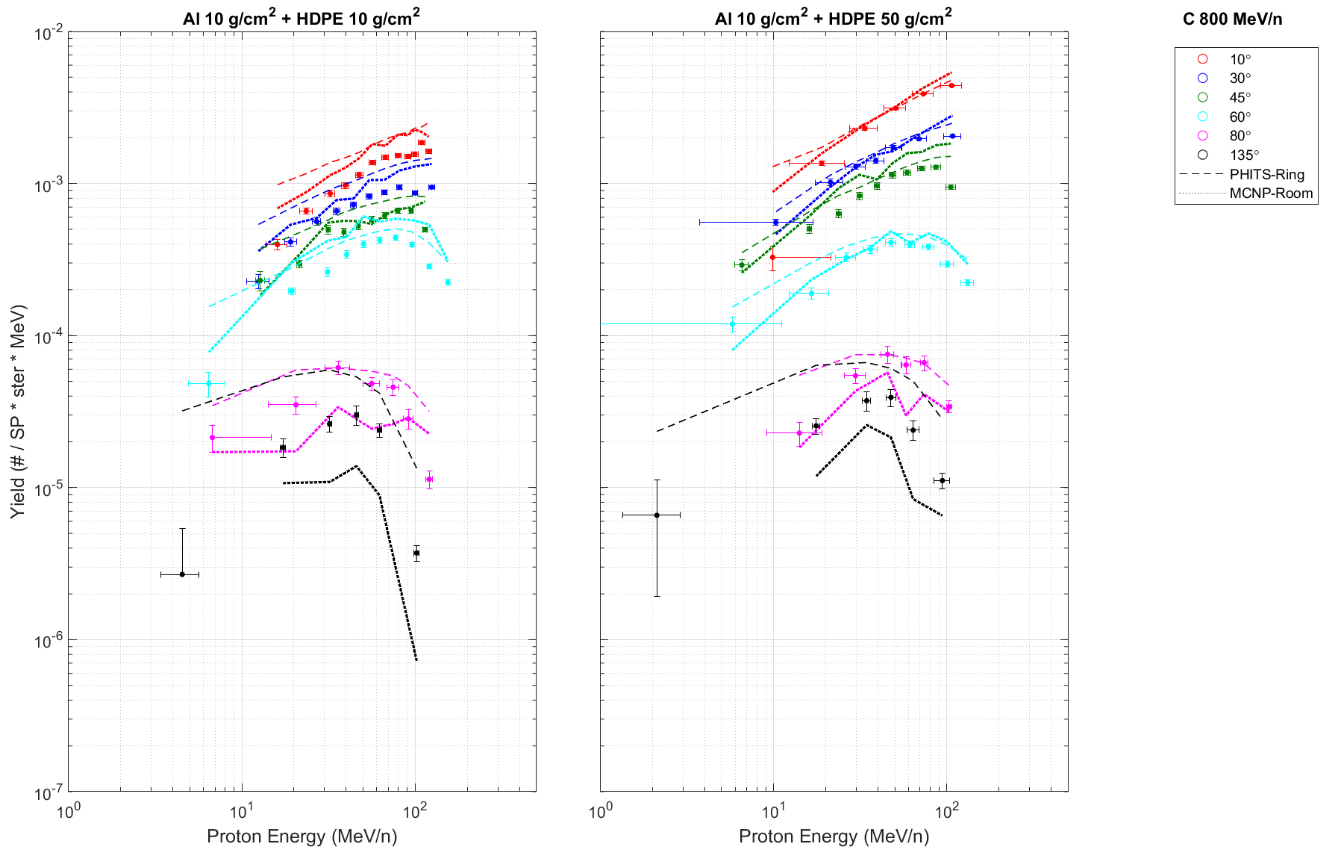

Figure 5.6. Double-differential thick-target proton yields for 800 MeV/n C beam on Al+HDPE upstream target with associated PHITS ring and MCNP room simulations.

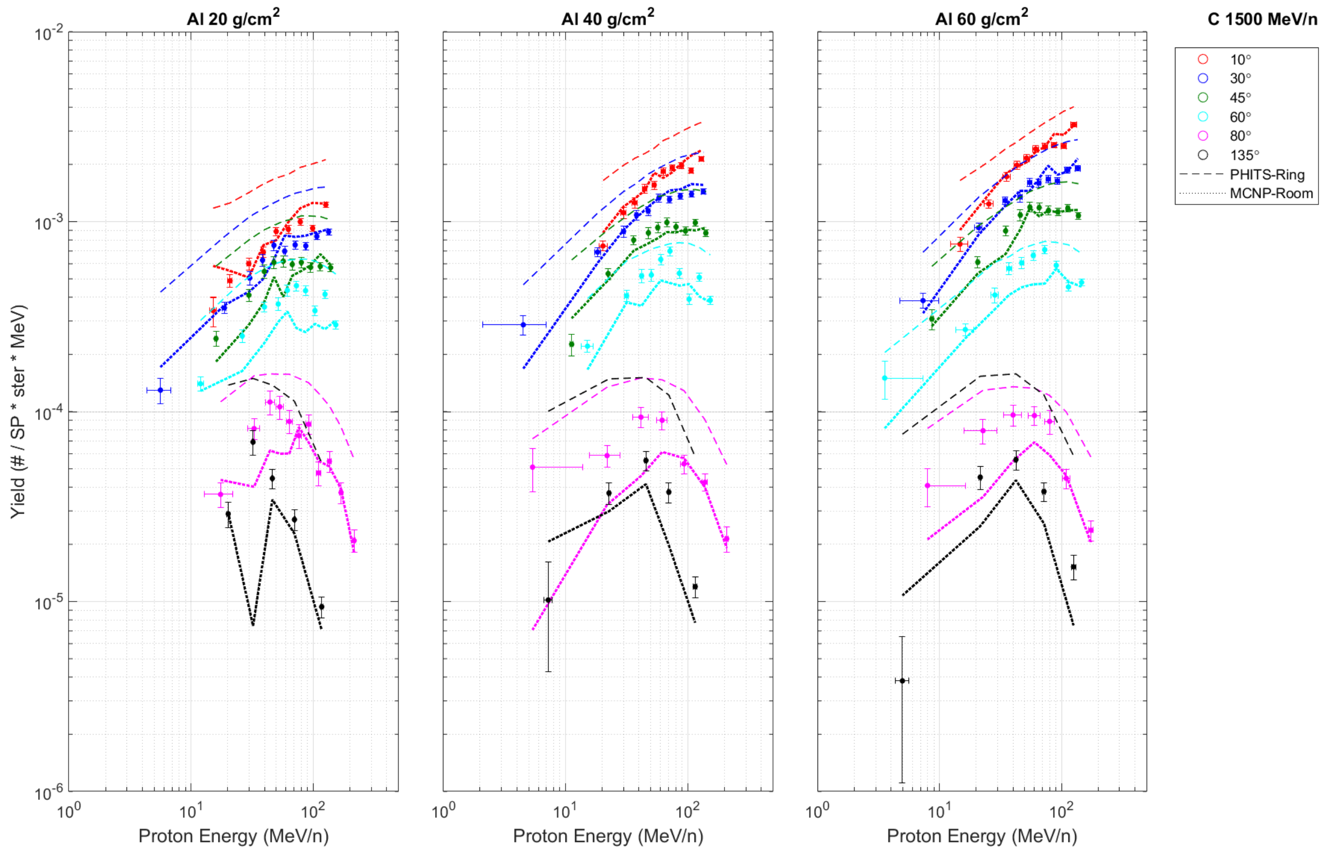

Figure 5.7. Double-differential thick-target proton yields for 1500 MeV/n C beam on Al upstream target with associated PHITS ring and MCNP room simulations.

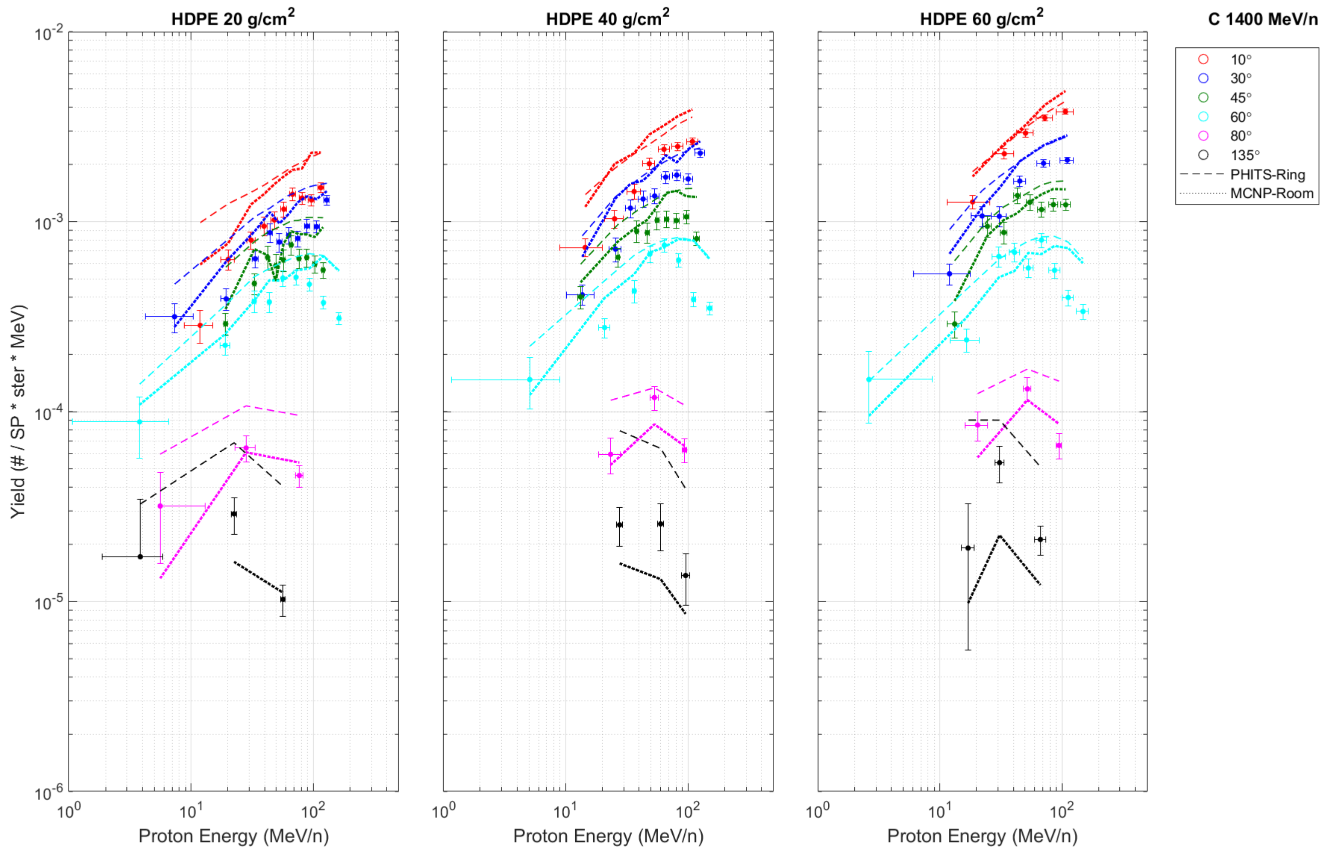

Figure 5.8. Double-differential thick-target proton yields for 1400 MeV/n C beam on HDPE upstream target with associated PHITS ring and MCNP room simulations.

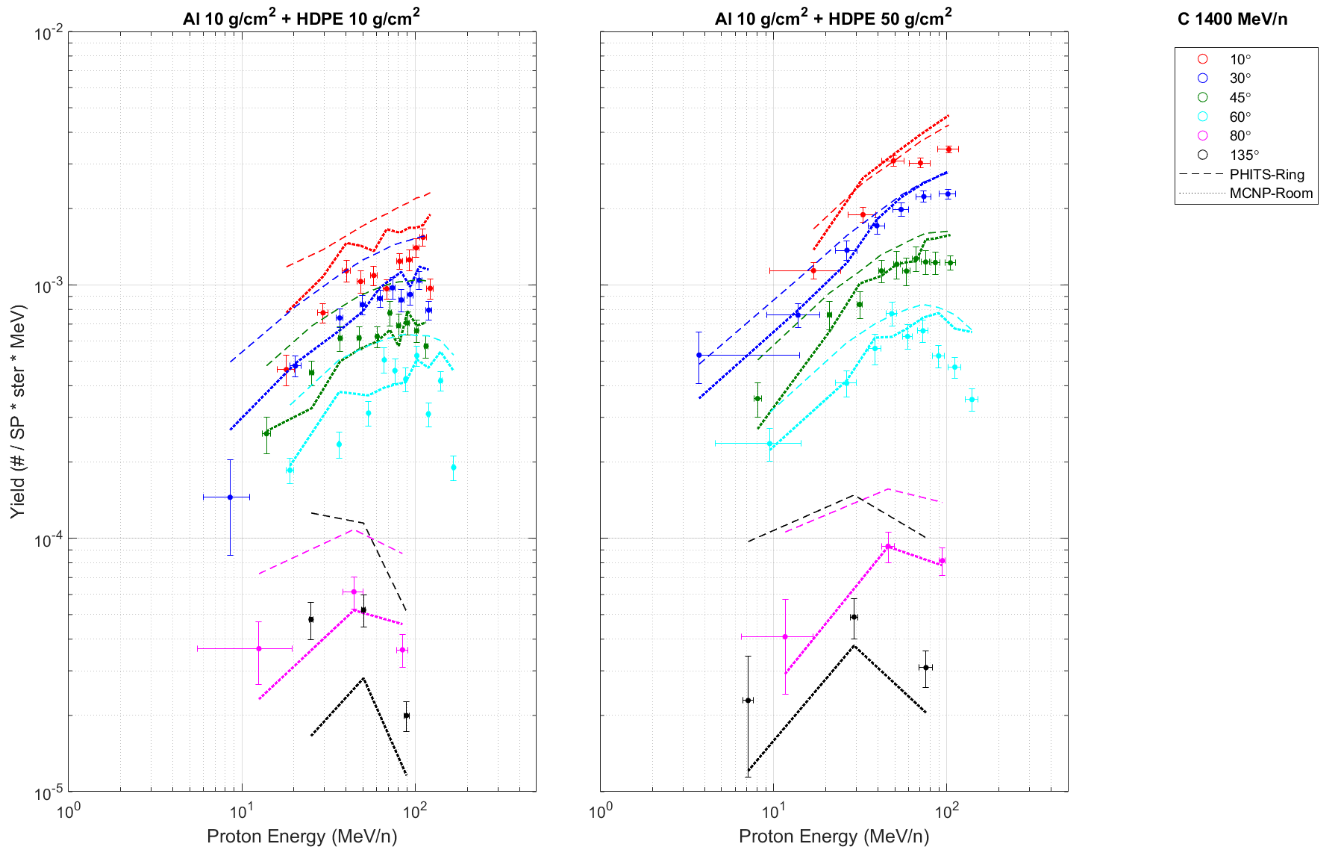

Figure 5.9. Double-differential thick-target proton yields for 1400 MeV/n C beam on Al+HDPE upstream target with associated PHITS ring and MCNP room simulations.

The DDTT deuteron yield results for carbon projectiles are displayed in Figure 5.10 through Figure 5.18. The experimental deuteron yields are predicted better by the PHITS ring simulations than by the MCNP room simulations for 400, 800, and 1500 MeV/n C projectiles on three types of upstream target. In most cases, both PHITS and MCNP under-predicted the magnitude of deuteron yields on Al upstream target by approximately 50%. For HDPE and Al+HDPE upstream targets, MCNP simulations under-estimated the deuteron yields by about 50-70%, while PHITS more closely predicted the deuteron yields. Overall, the experimental, PHITS, and MCNP simulated deuteron yields improve agreement with each other as the upstream target thickness increases for all three energies of C projectiles. Also, the experimental results for deuteron generally agree with simulations with regard to the shapes of the spectra, but the agreement in magnitudes varies from target combination to target combination. Since the coalescence model might not coalesce enough, PHITS and MCNP mostly underestimated the deuteron yields.

The DDTT triton yield results for carbon projectiles are displayed in Figure 5.19 through Figure 5.27. For 800- and 1500-MeV/n C projectiles, the experimental triton yields and the PHITS and MCNP simulated results do not present agreement either in the shapes of spectra or in the magnitude. Both PHITS ring and MCNP room simulations under-predicted the triton yields for 400 MeV/n C projectiles on all three types of upstream target by approximately at least 50%. However, the PHITS ring and MCNP room simulations approximately predicted the similar trend to the experimental triton results at the 10° detector for 400 MeV/n C projectiles on all three types of upstream target. The triton underestimation might also result from the coalescence models in PHITS and MCNP.

The DDTT helium-3 yield results for carbon projectiles are displayed in Figure 5.28 through Figure 5.36. PHITS and MCNP simulated helium-3 results for 400 MeV/n C projectiles on all types of upstream target predicted similar trend to the experimental helium-3 yield regarding the shape of spectra, but PHITS and MCNP simulations mostly underestimated the magnitude of helium-3 yields by approximately more than 50%. The

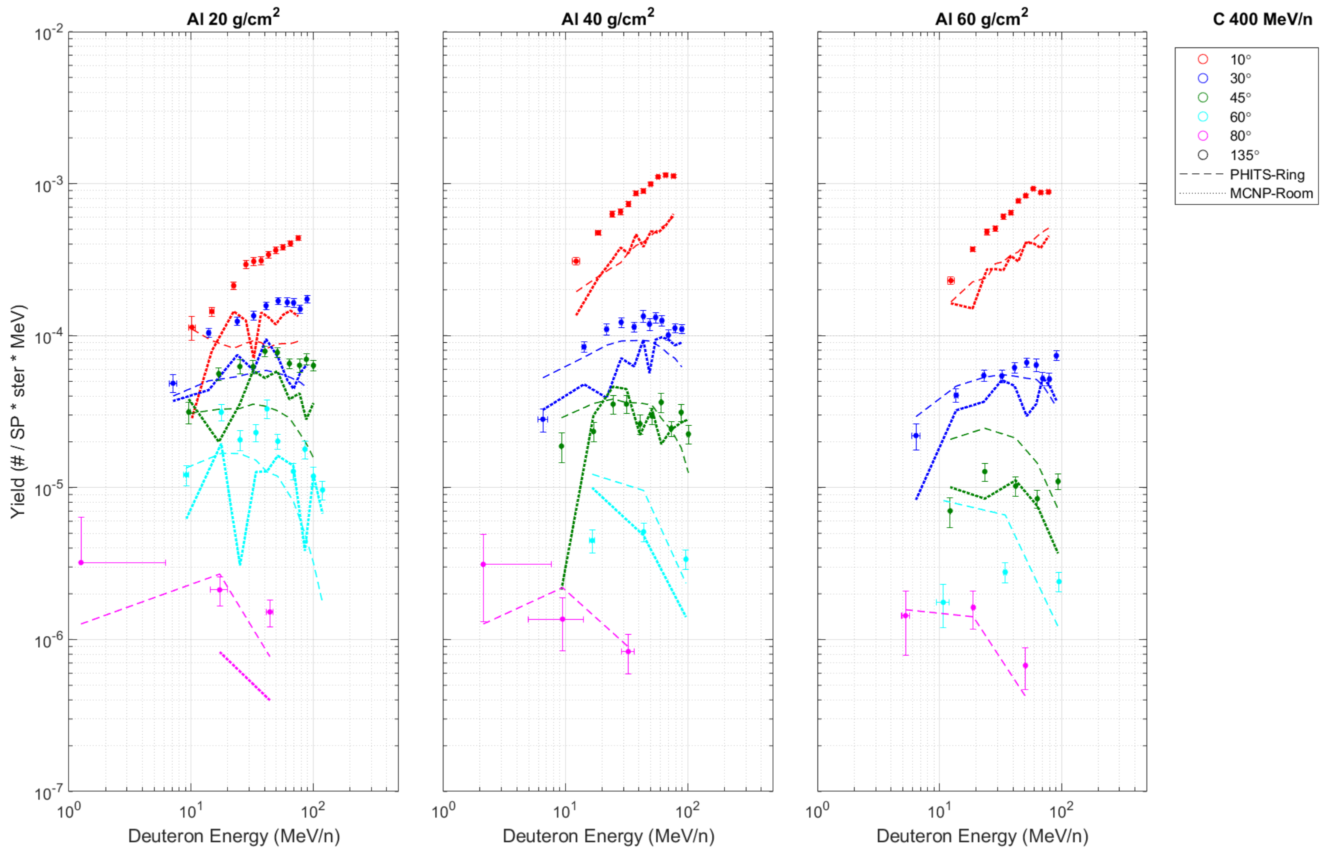

Figure 5.10. Double-differential thick-target deuteron yields for 400 MeV/n C beam on Al upstream target with associated PHITS ring and MCNP room simulations.

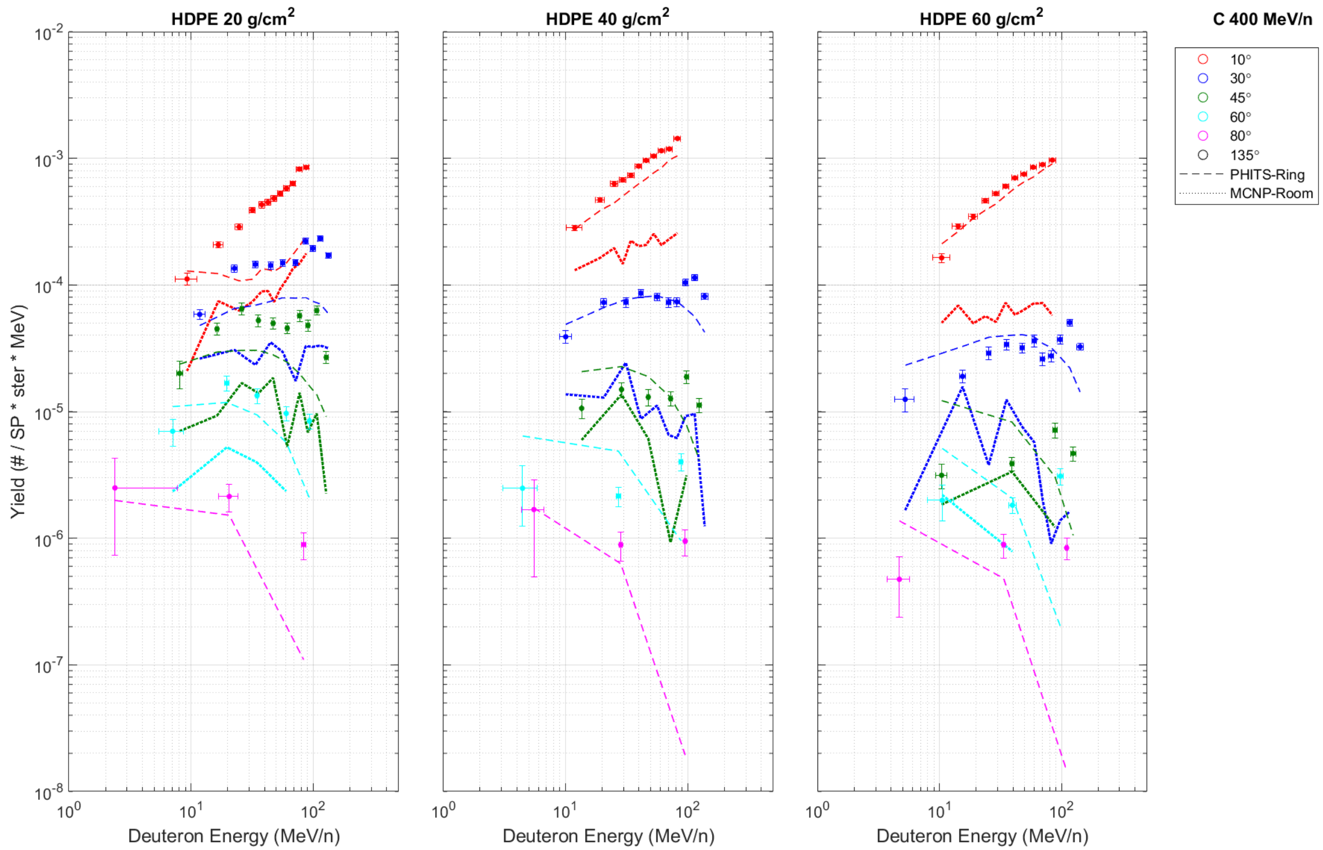

Figure 5.11. Double-differential thick-target deuteron yields for 400 MeV/n C beam on HDPE upstream target with associated PHITS ring and MCNP room simulations.

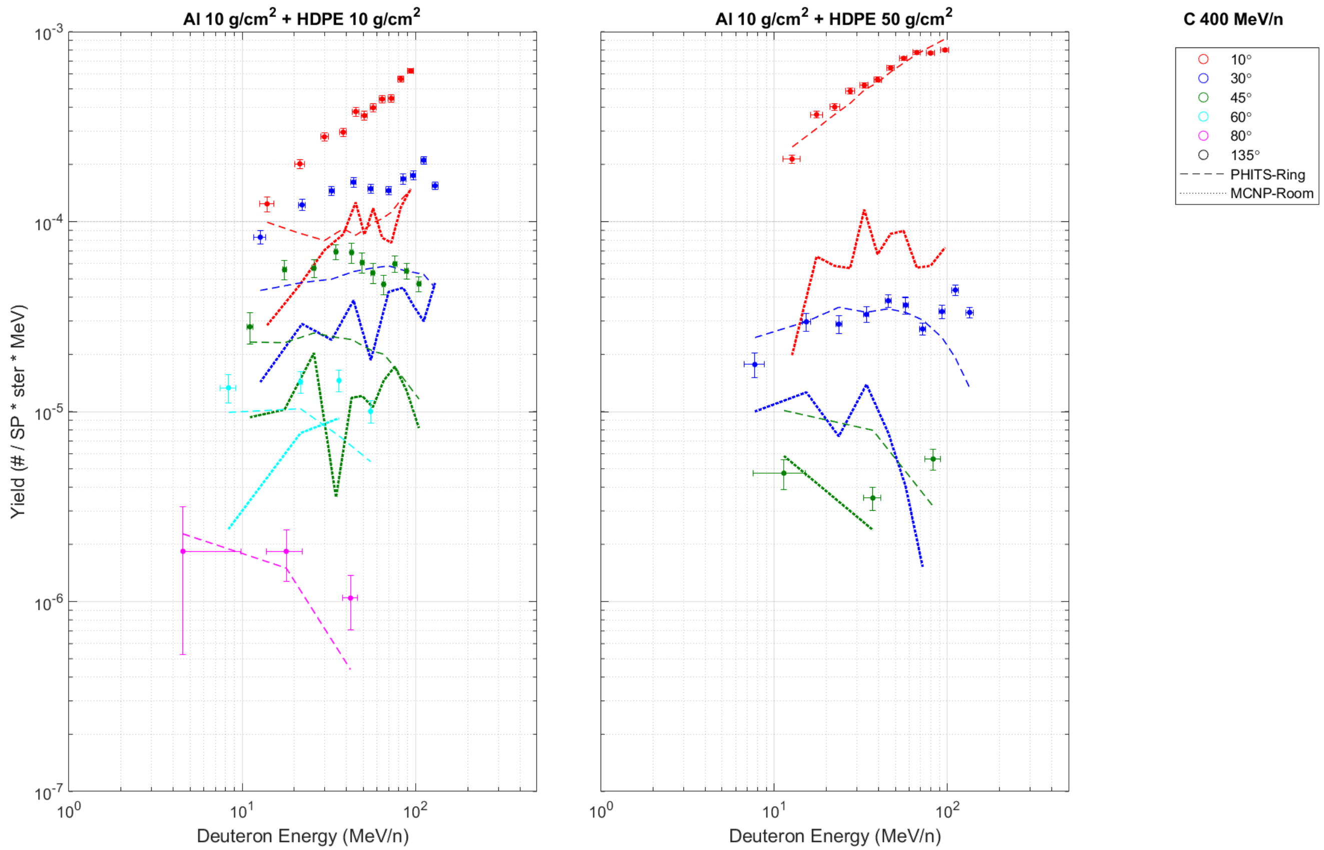

Figure 5.12. Double-differential thick-target deuteron yields for 400 MeV/n C beam on Al+HDPE upstream target with associated PHITS ring and MCNP room simulations.

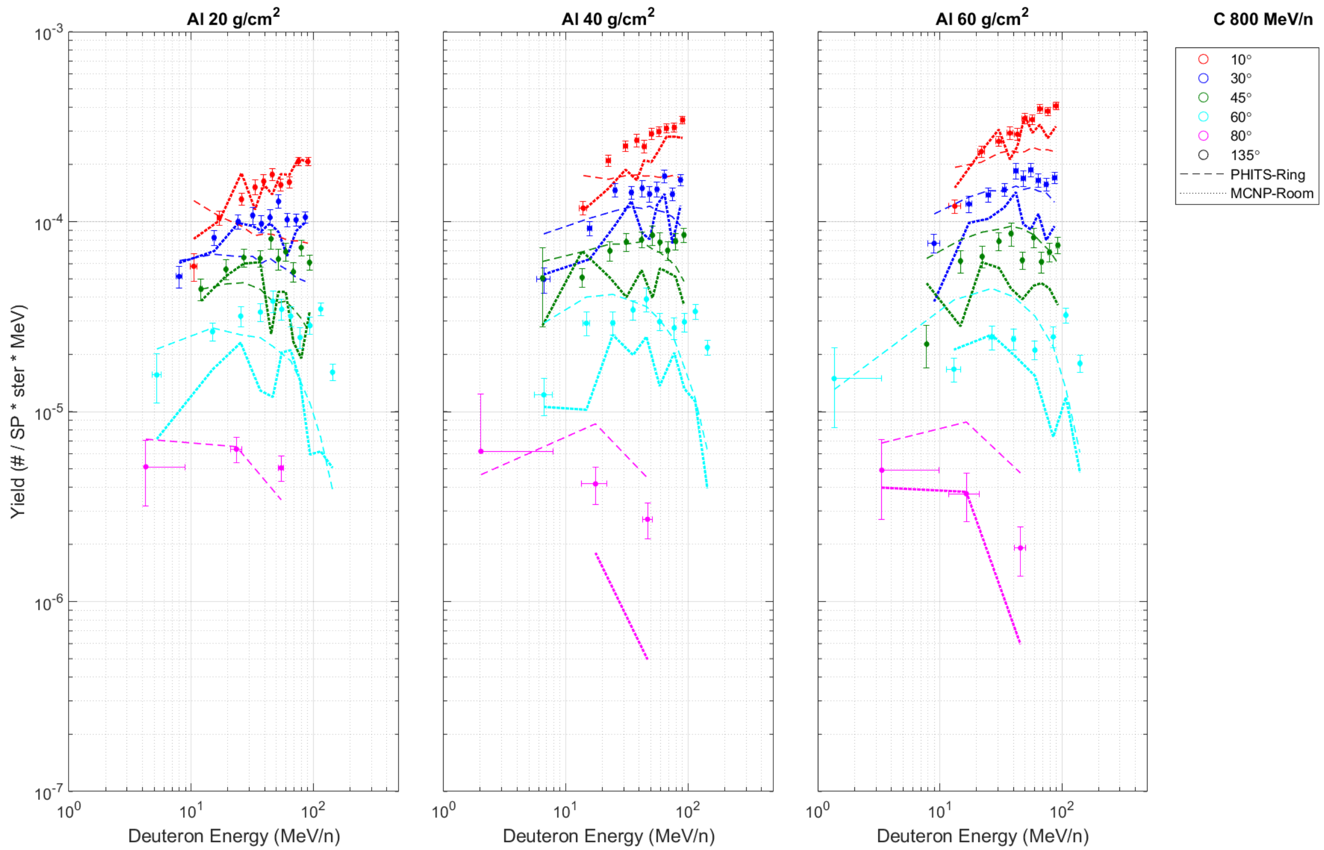

Figure 5.13. Double-differential thick-target deuteron yields for 800 MeV/n C beam on Al upstream target with associated PHITS ring and MCNP room simulations.

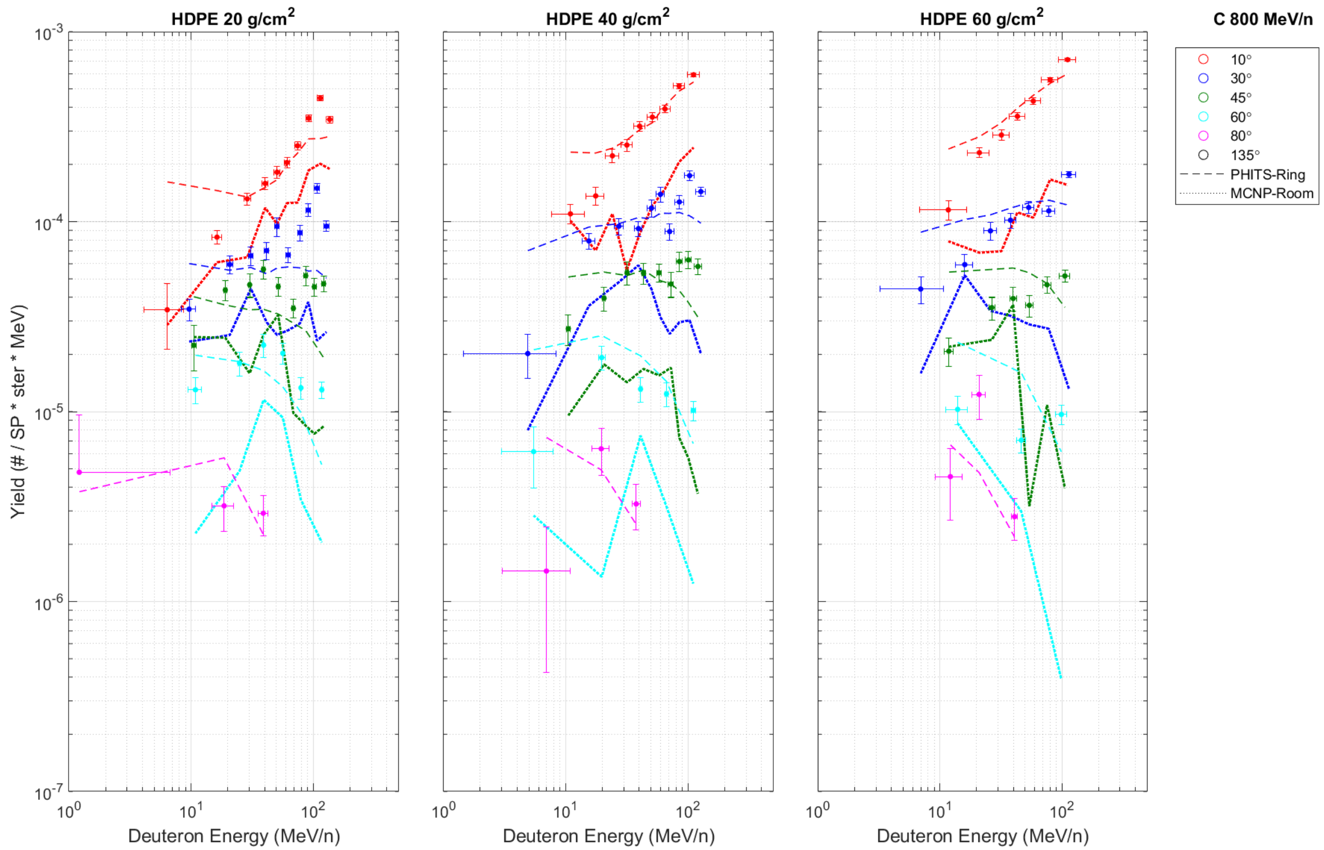

Figure 5.14. Double-differential thick-target deuteron yields for 800 MeV/n C beam on HDPE upstream target with associated PHITS ring and MCNP room simulations.

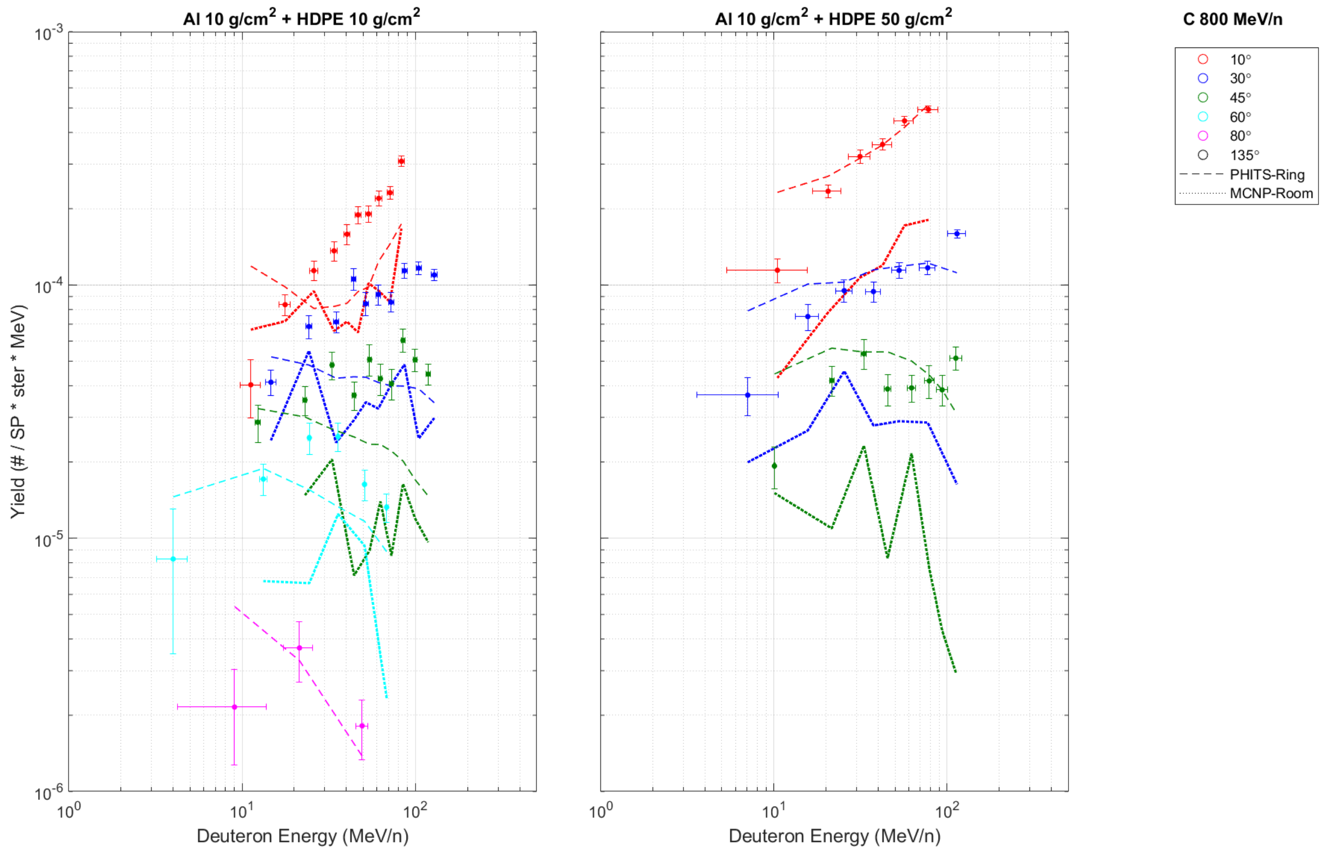

Figure 5.15. Double-differential thick-target deuteron yields for 800 MeV/n C beam on Al+HDPE upstream target with associated PHITS ring and MCNP room simulations.

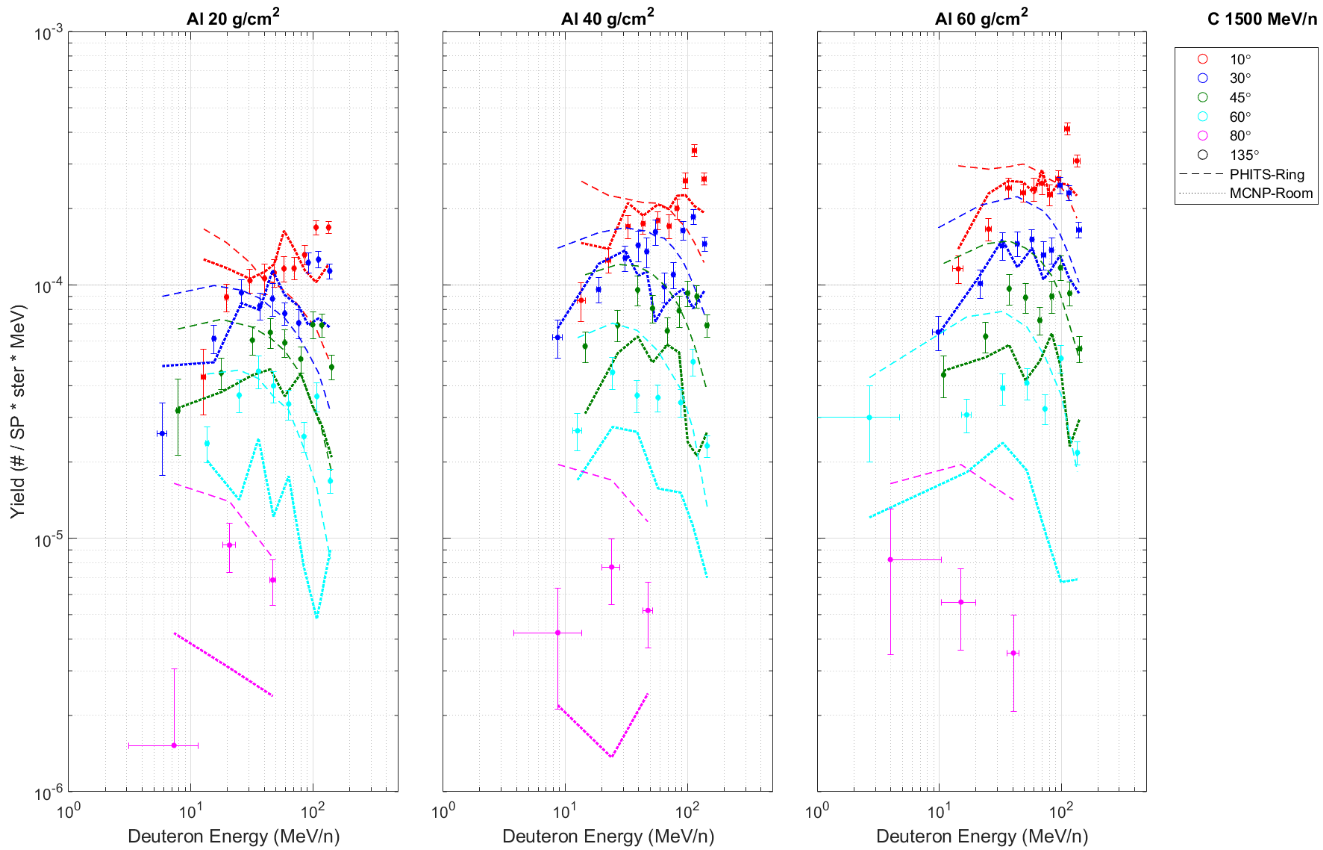

Figure 5.16. Double-differential thick-target deuteron yields for 1500 MeV/n C beam on Al upstream target with associated PHITS ring and MCNP room simulations.

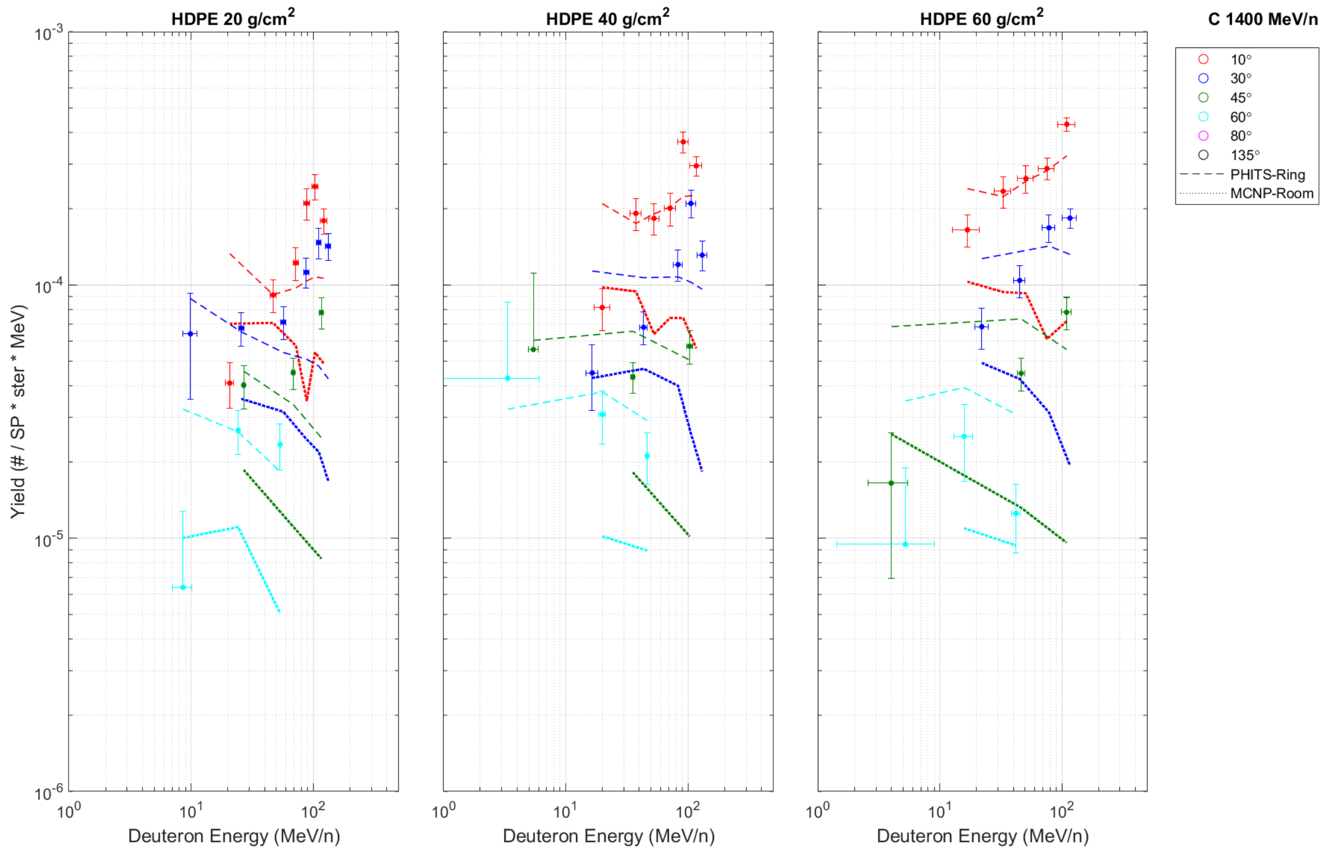

Figure 5.17. Double-differential thick-target deuteron yields for 1400 MeV/n C beam on HDPE upstream target with associated PHITS ring and MCNP room simulations.

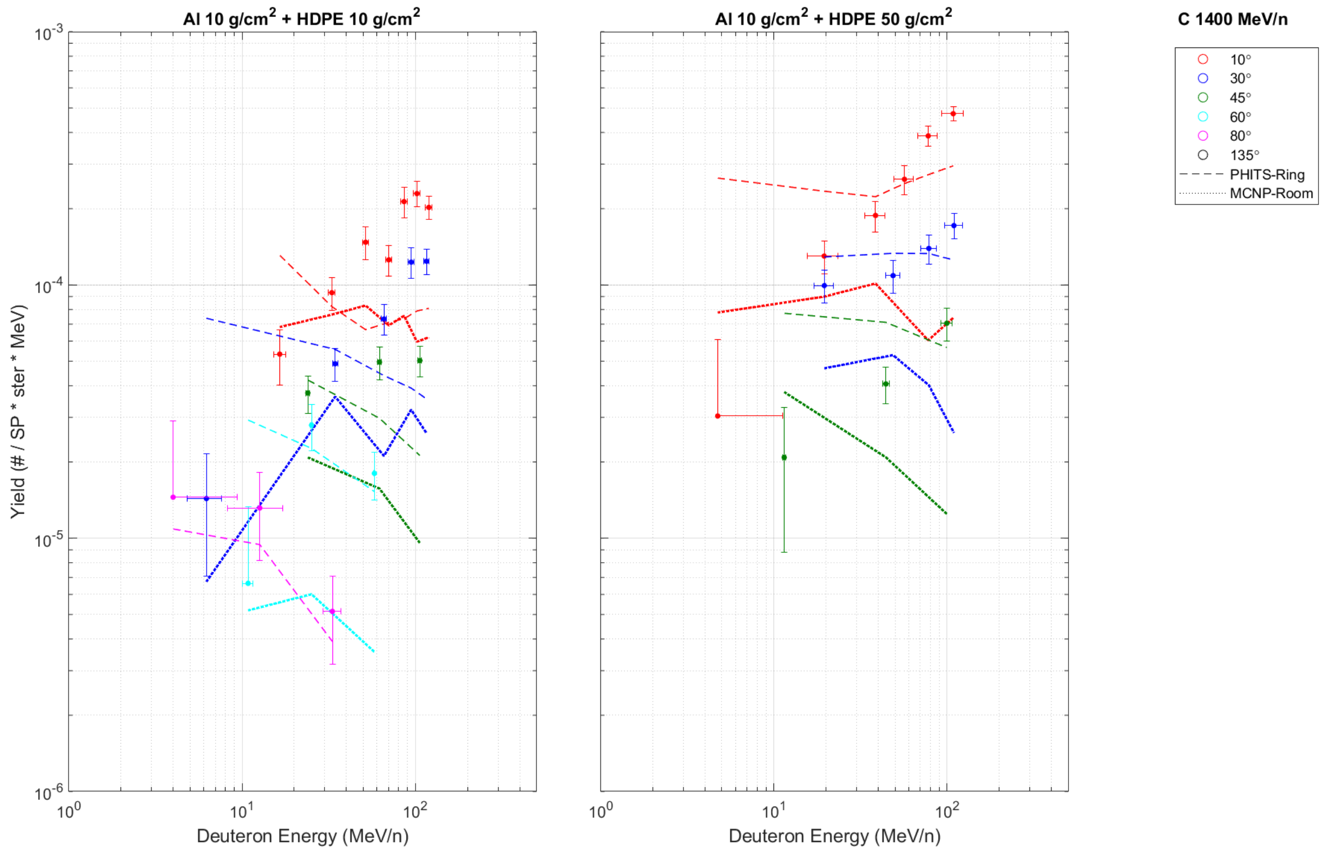

Figure 5.18. Double-differential thick-target deuteron yields for 1400 MeV/n C beam on Al+HDPE upstream target with associated PHITS ring and MCNP room simulations.

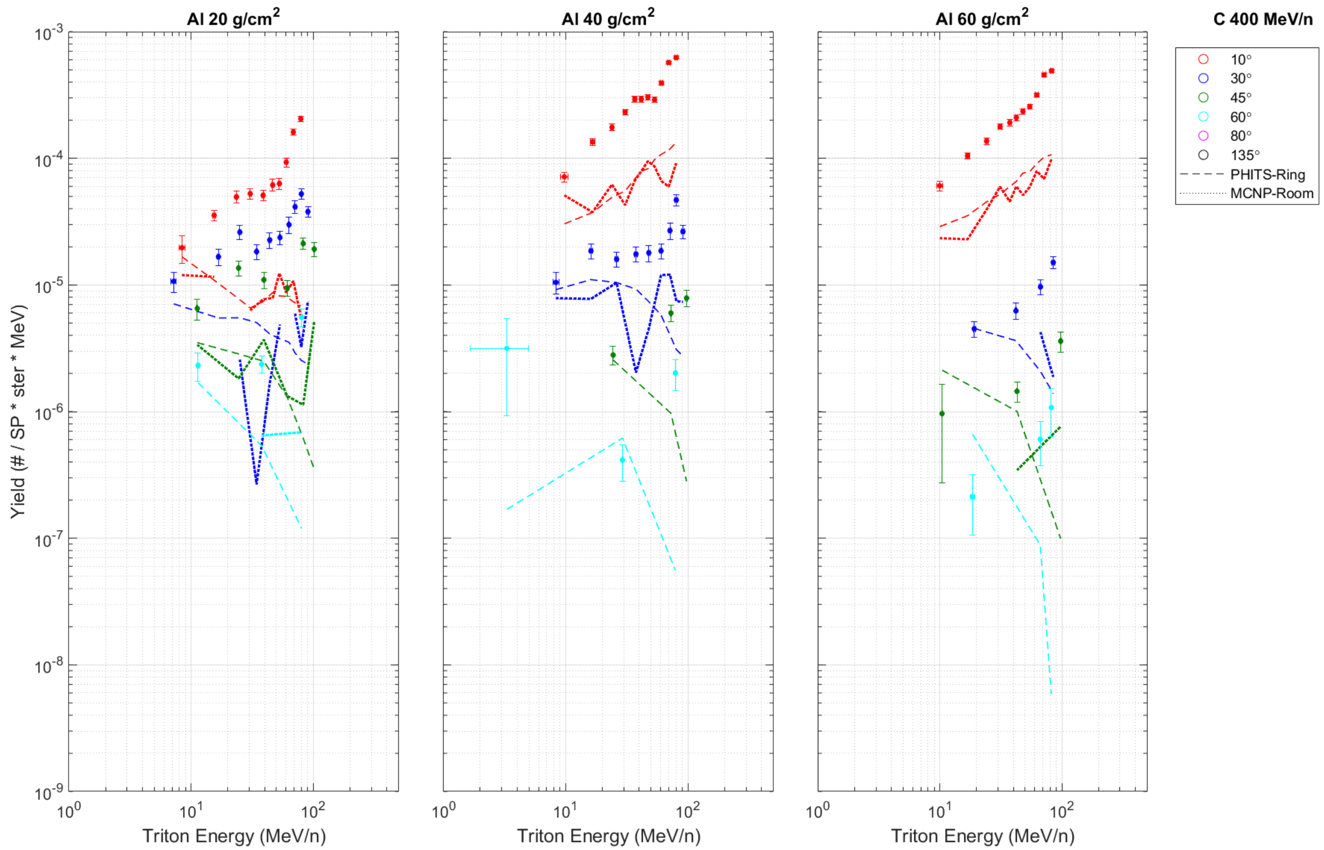

Figure 5.19. Double-differential thick-target triton yields for 400 MeV/n C beam on Al upstream target with associated PHITS ring and MCNP room simulations.

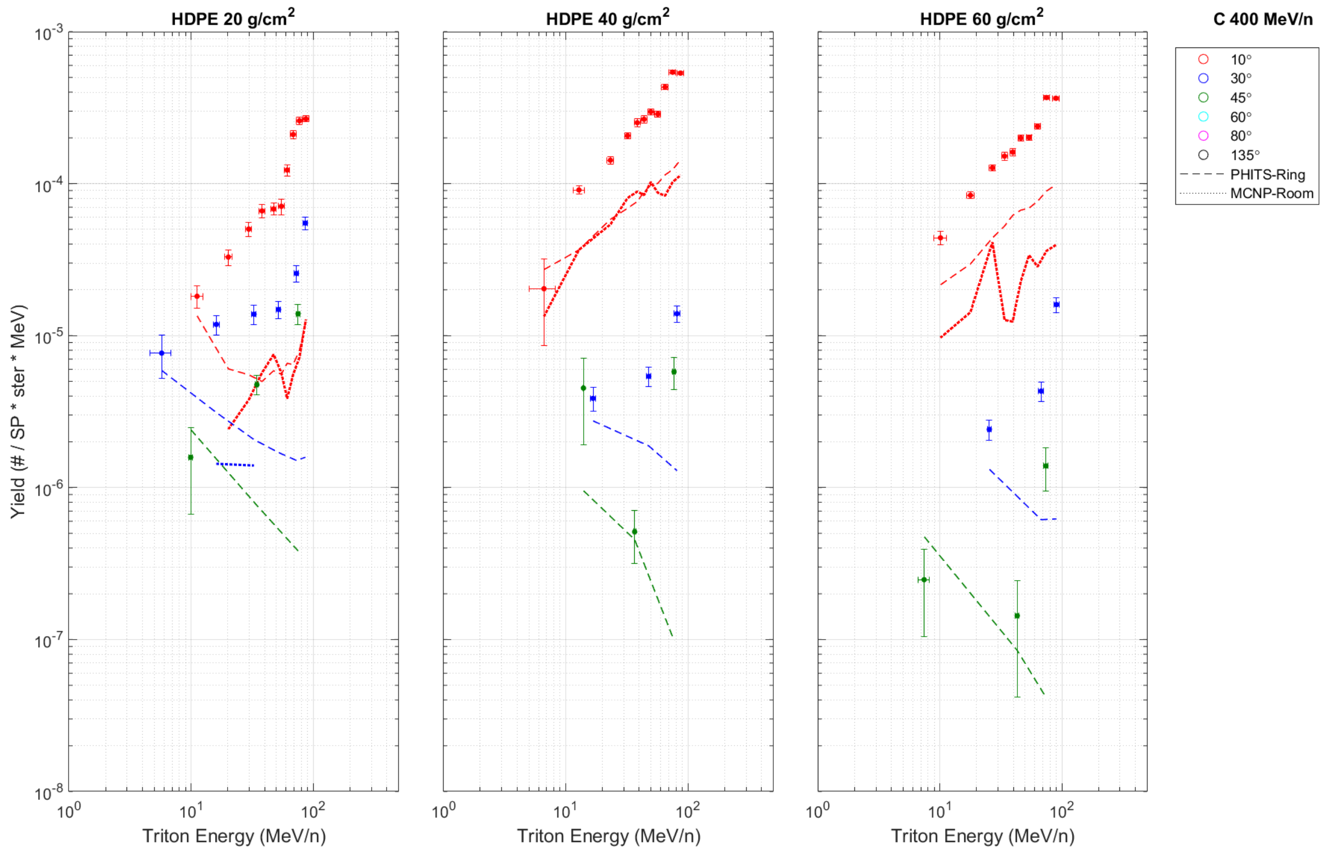

Figure 5.20. Double-differential thick-target triton yields for 400 MeV/n C beam on HDPE upstream target with associated PHITS ring and MCNP room simulations.

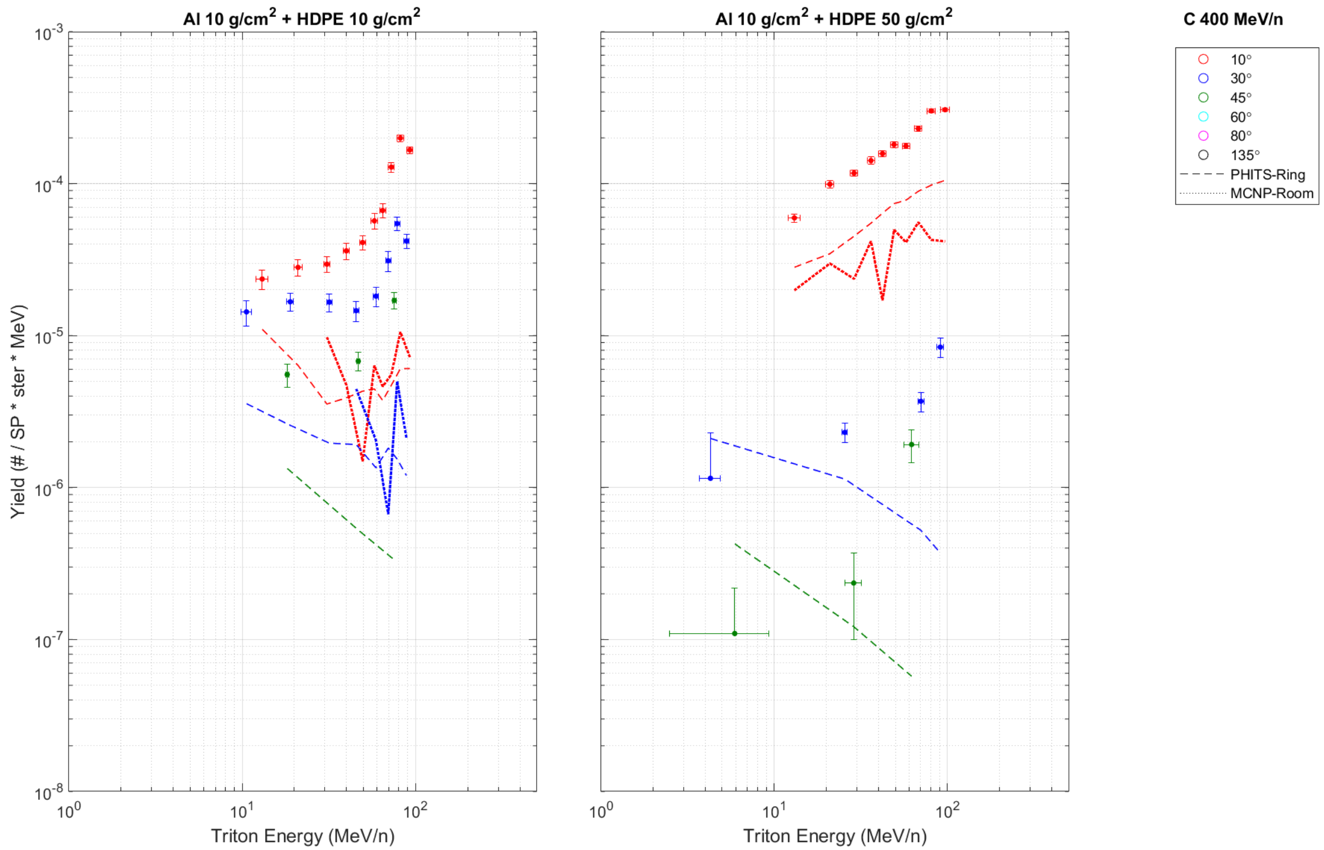

Figure 5.21. Double-differential thick-target triton yields for 400 MeV/n C beam on Al+HDPE upstream target with associated PHITS ring and MCNP room simulations.

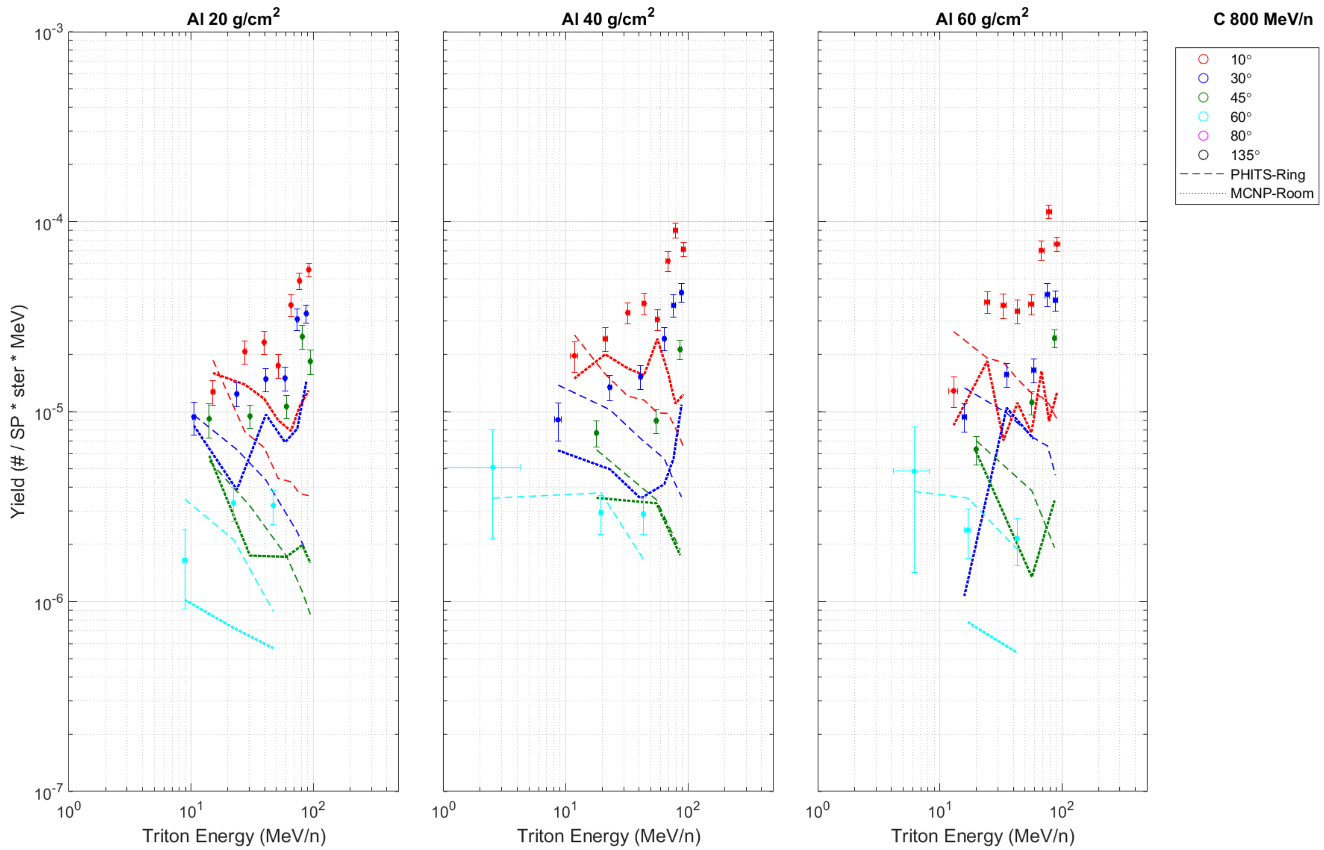

Figure 5.22. Double-differential thick-target triton yields for 800 MeV/n C beam on Al upstream target with associated PHITS ring and MCNP room simulations.

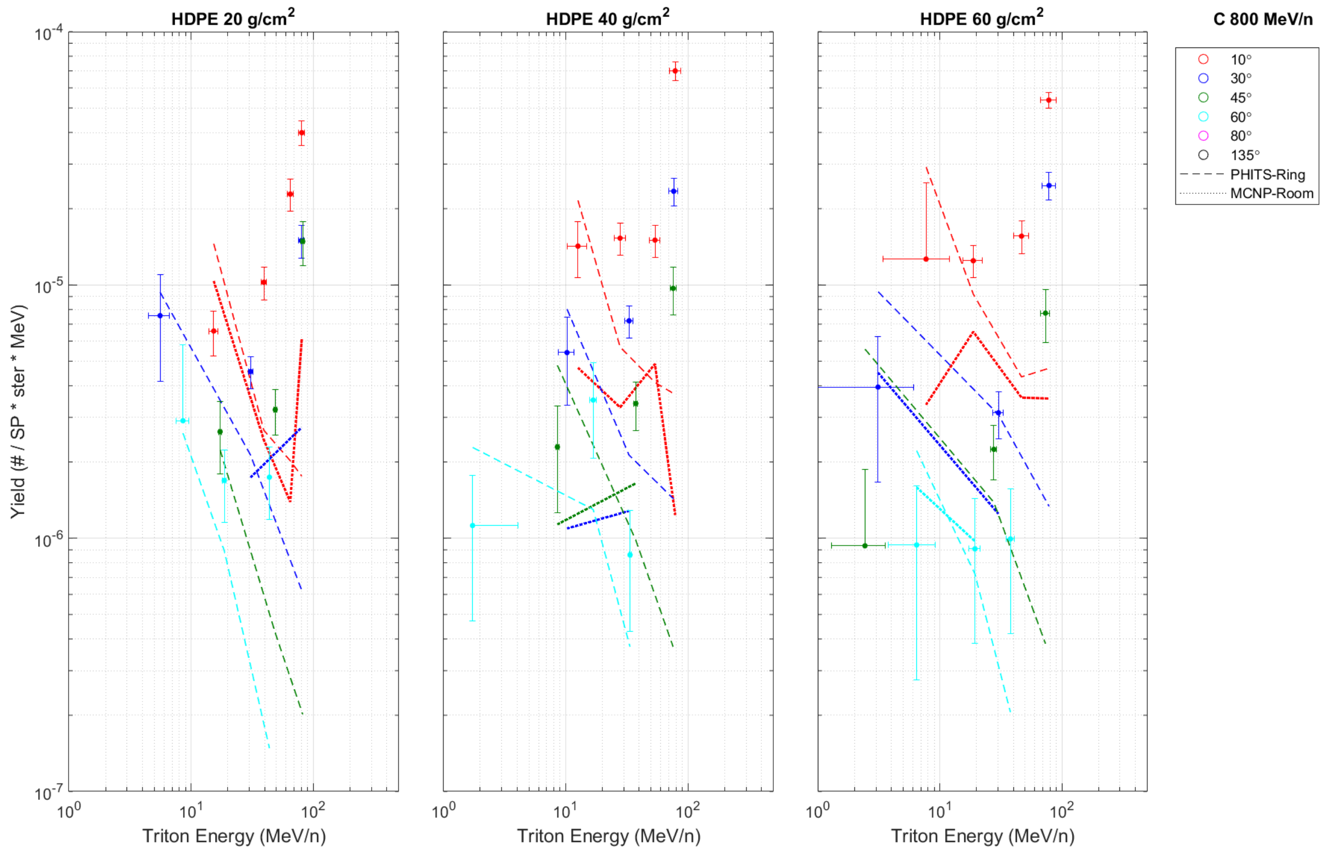

Figure 5.23. Double-differential thick-target triton yields for 800 MeV/n C beam on HDPE upstream target with associated PHITS ring and MCNP room simulations.

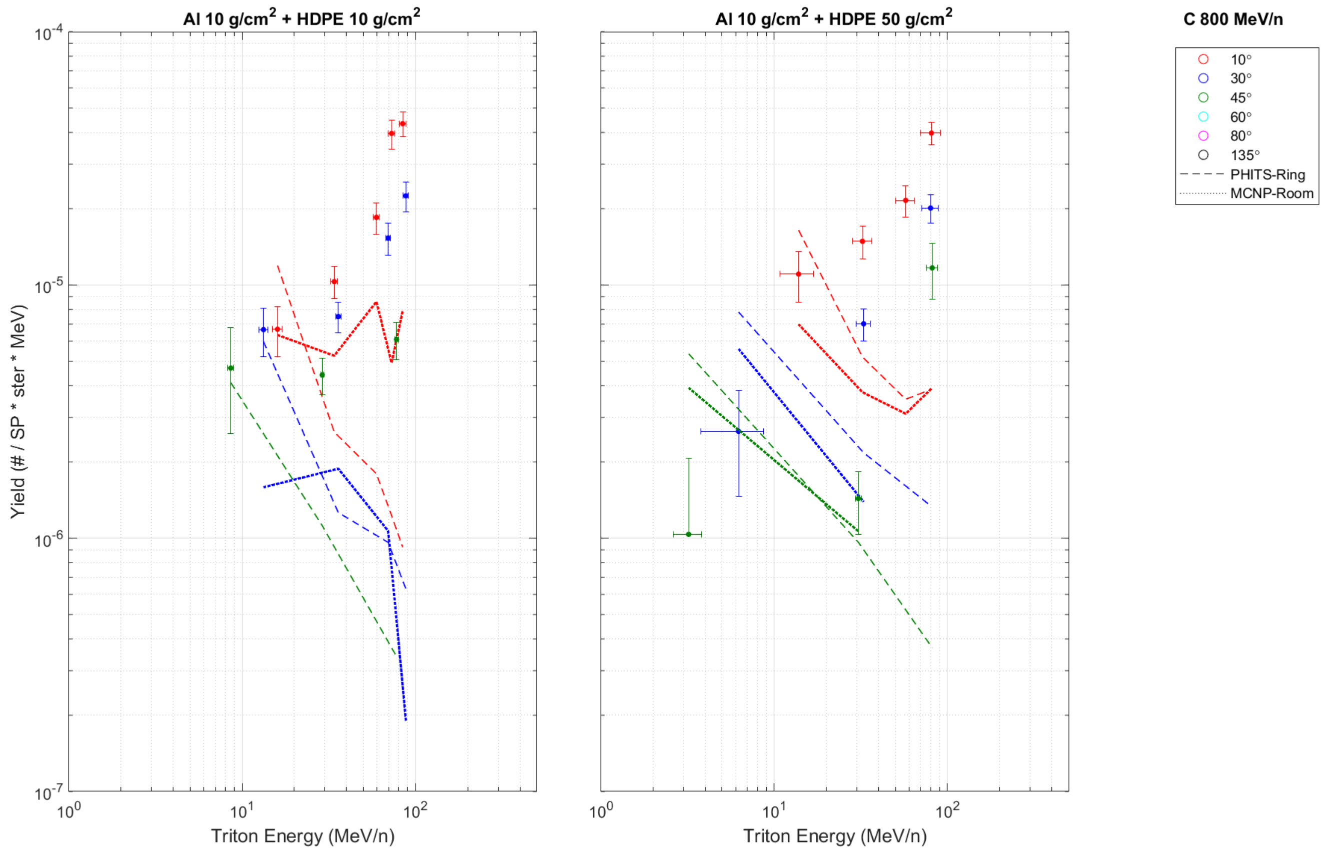

Figure 5.24. Double-differential thick-target triton yields for 800 MeV/n C beam on Al+HDPE upstream target with associated PHITS ring and MCNP room simulations.

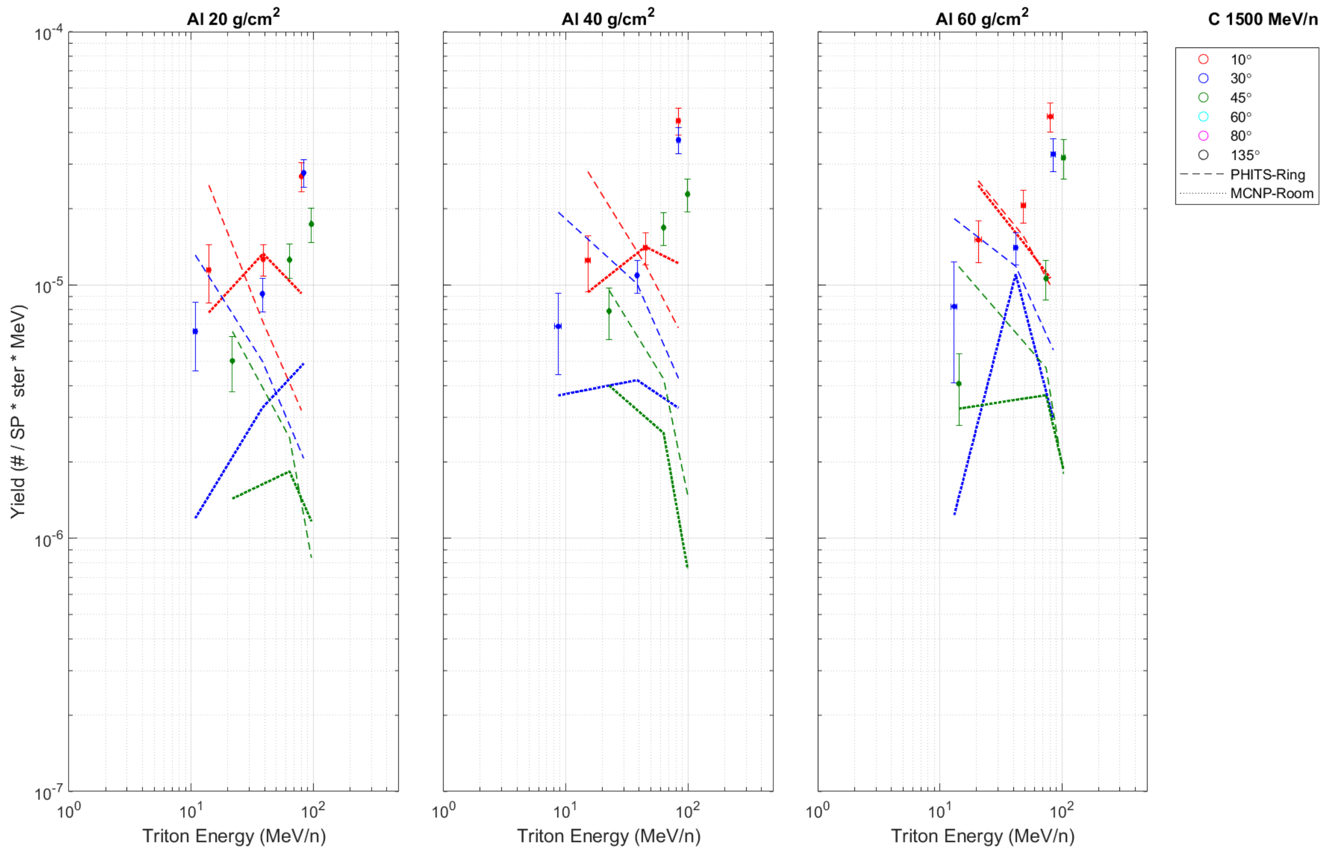

Figure 5.25. Double-differential thick-target triton yields for 1500 MeV/n C beam on Al upstream target with associated PHITS ring and MCNP room simulations.

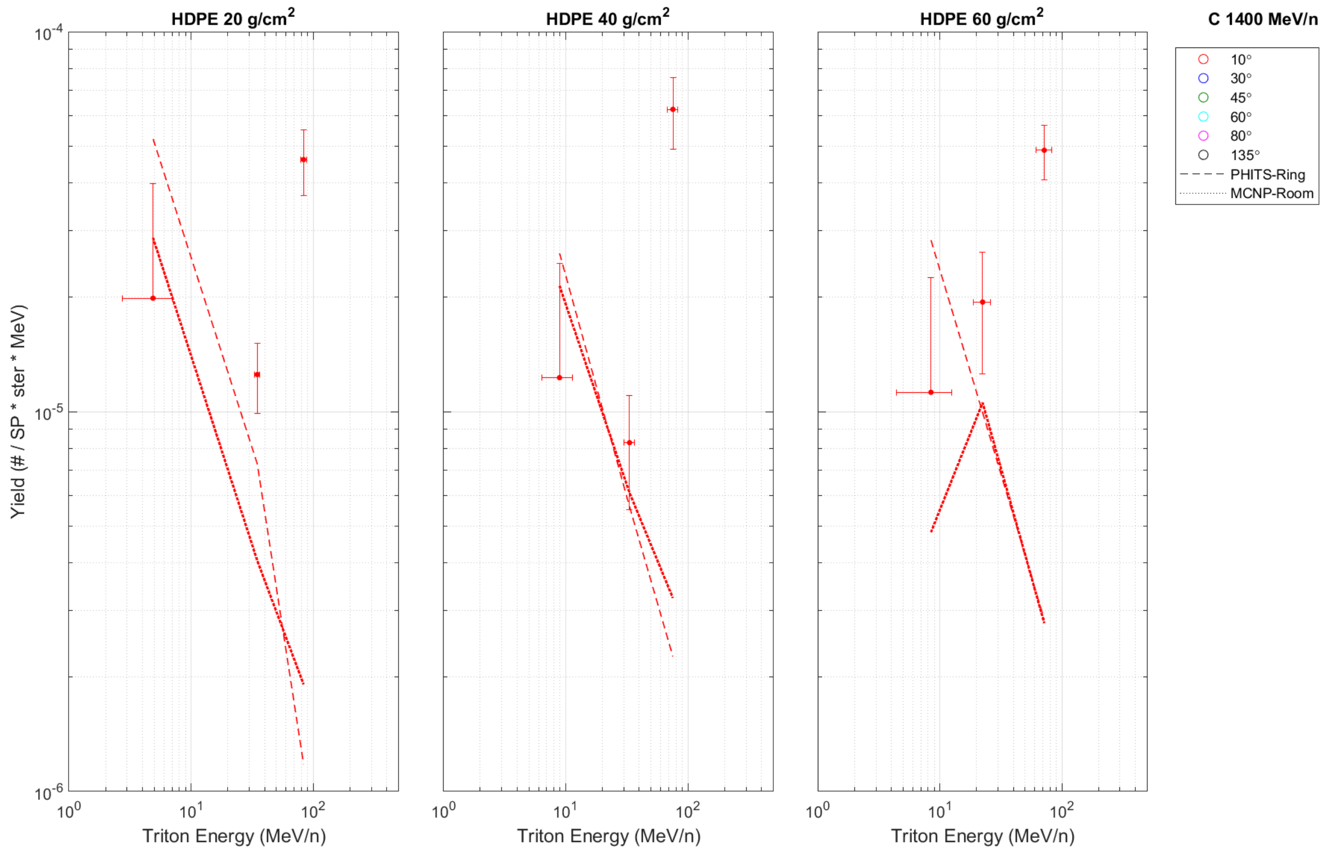

Figure 5.26. Double-differential thick-target triton yields for 1400 MeV/n C beam on HDPE upstream target with associated PHITS ring and MCNP room simulations.

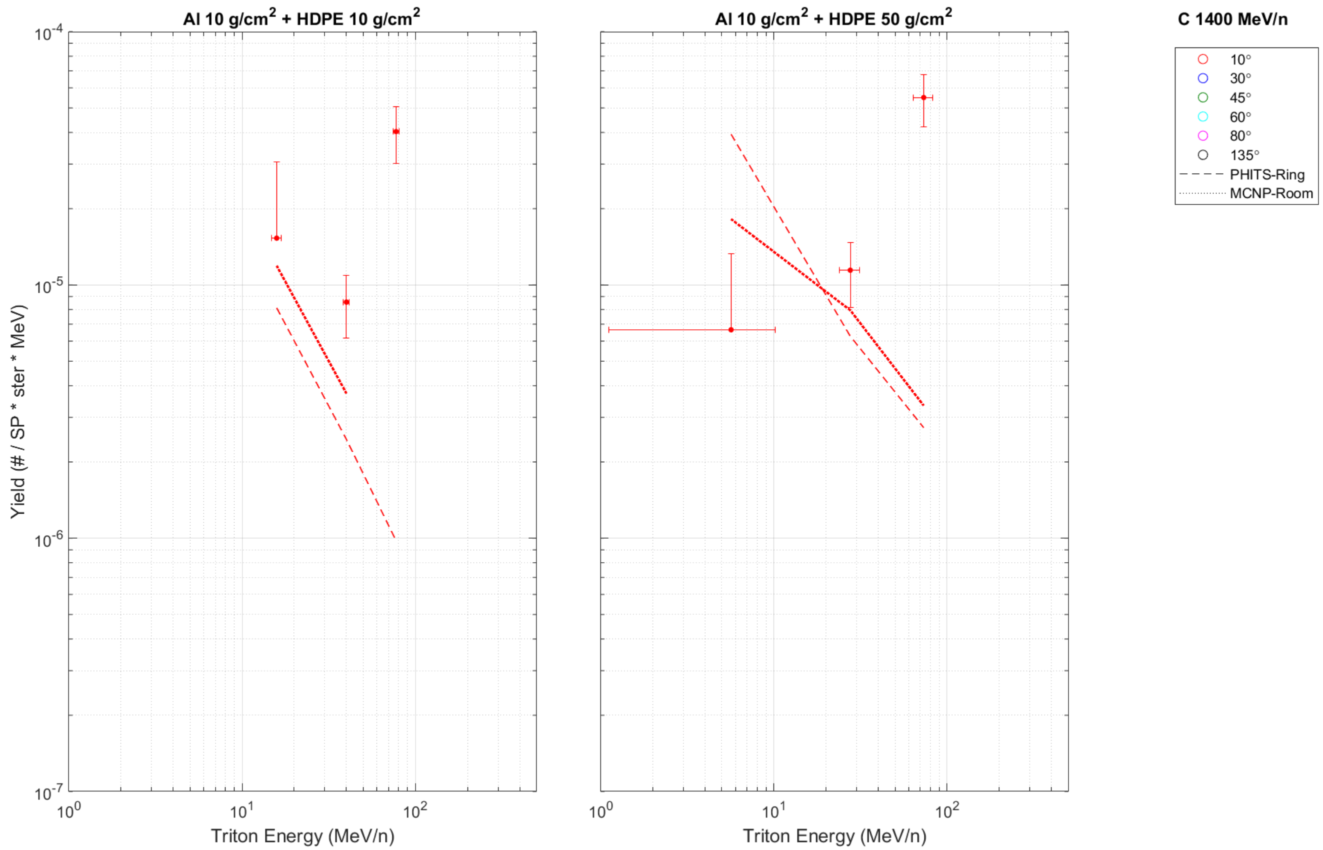

Figure 5.27. Double-differential thick-target triton yields for 1400 MeV/n C beam on Al+HDPE upstream target with associated PHITS ring and MCNP room simulations.

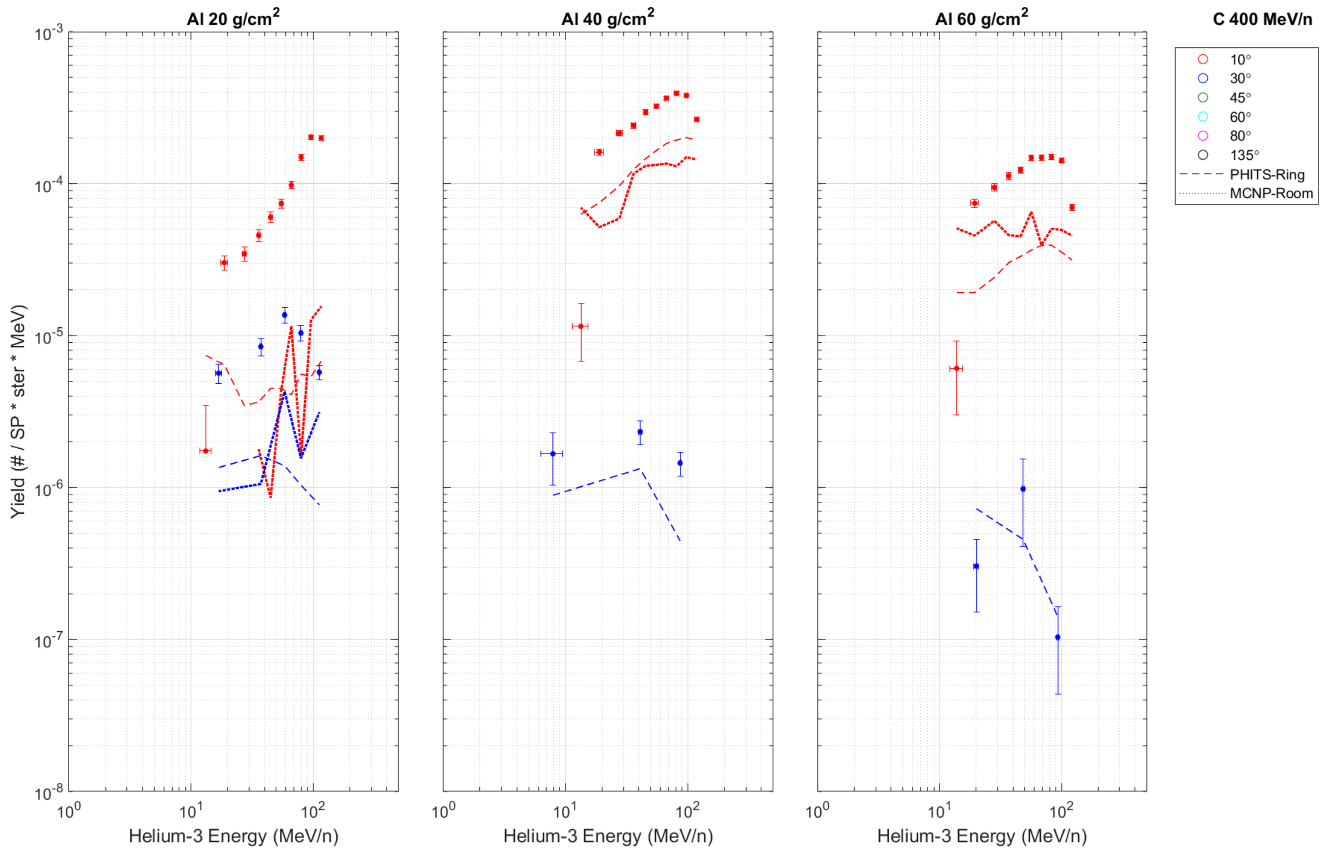

Figure 5.28. Double-differential thick-target helium-3 yields for 400 MeV/n C beam on Al upstream target with associated PHITS ring and MCNP room simulations.

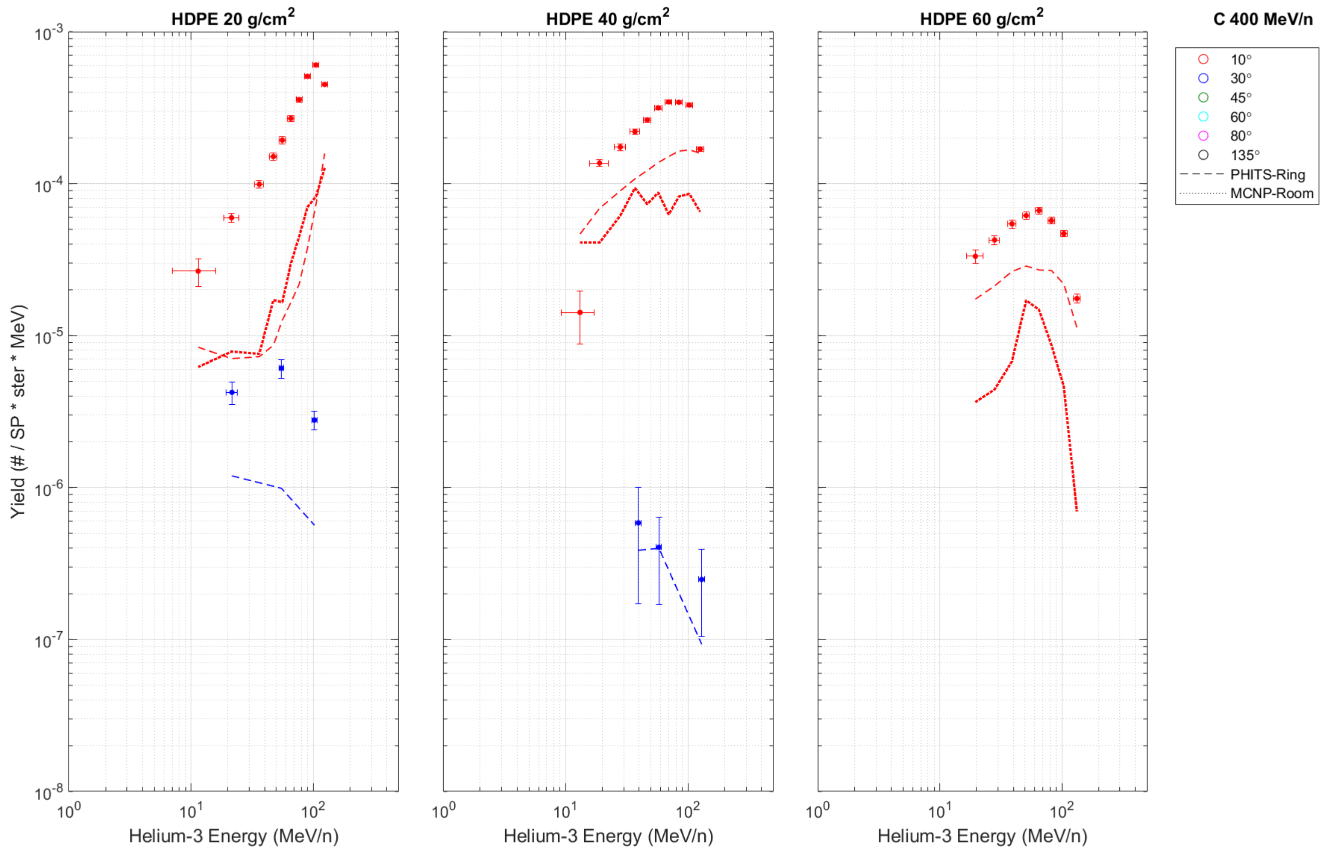

Figure 5.29. Double-differential thick-target helium-3 yields for 400 MeV/n C beam on HDPE upstream target with associated PHITS ring and MCNP room simulations.

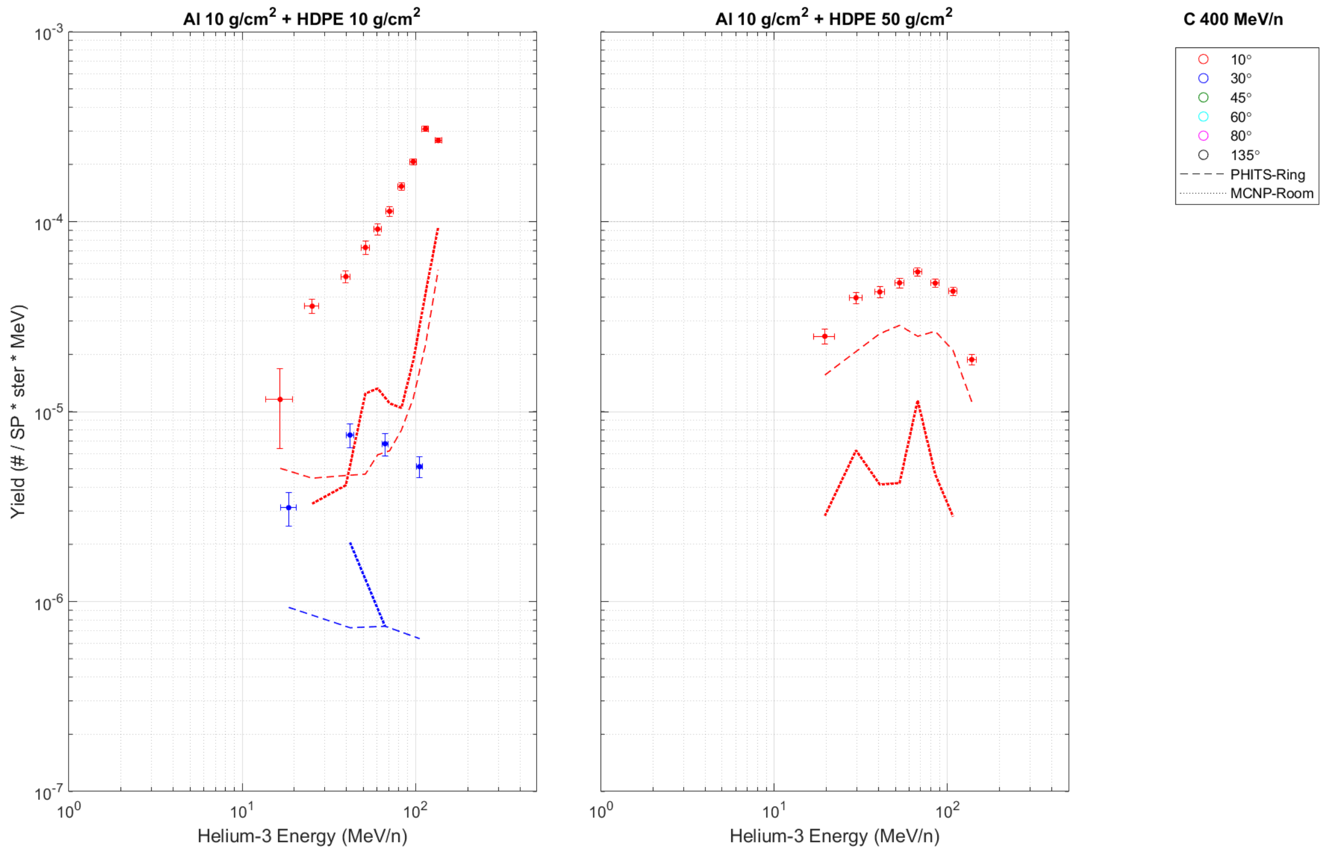

Figure 5.30. Double-differential thick-target helium-3 yields for 400 MeV/n C beam on Al+HDPE upstream target with associated PHITS ring and MCNP room simulations.

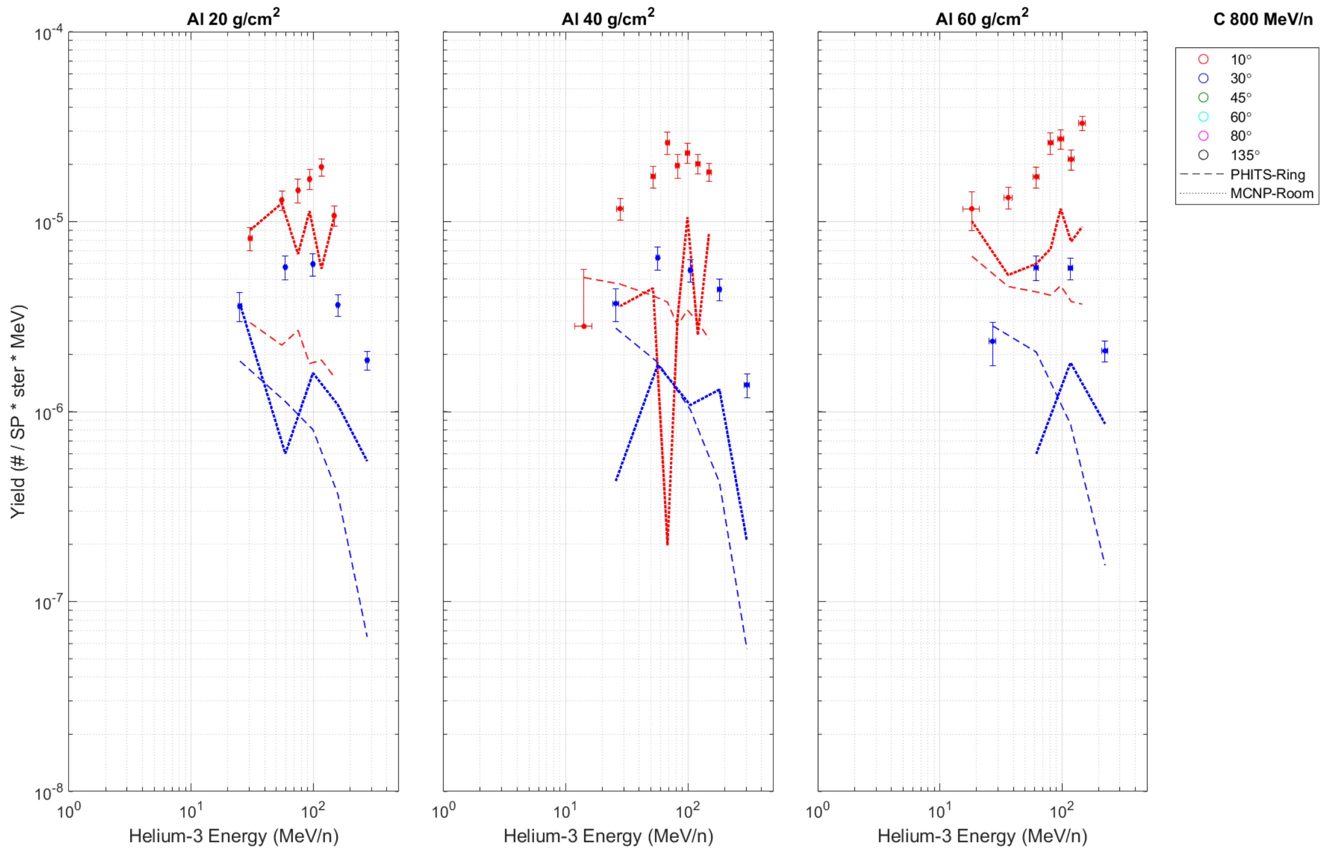

Figure 5.31. Double-differential thick-target helium-3 yields for 800 MeV/n C beam on Al upstream target with associated PHITS ring and MCNP room simulations.

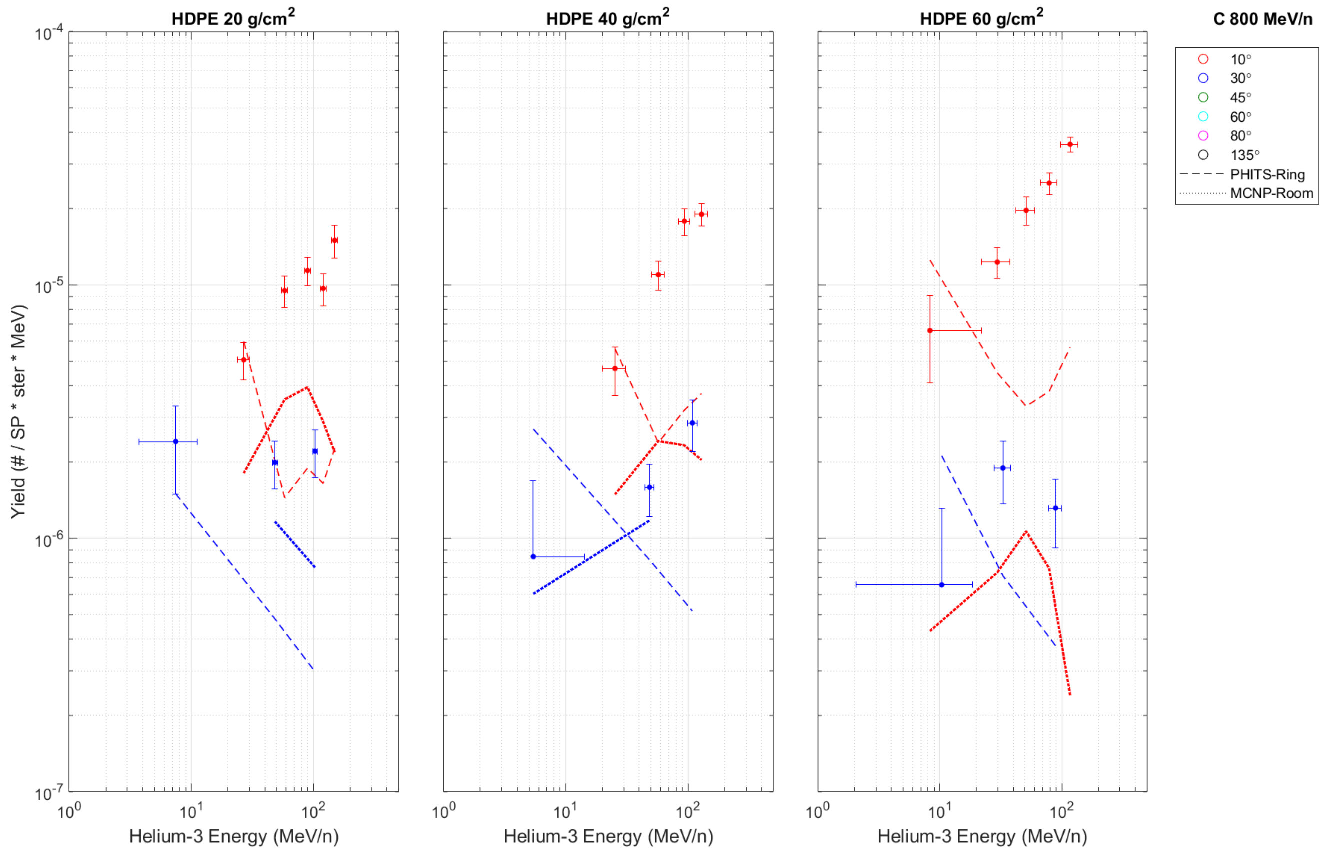

Figure 5.32. Double-differential thick-target helium-3 yields for 800 MeV/n C beam on HDPE upstream target with associated PHITS ring and MCNP room simulations.

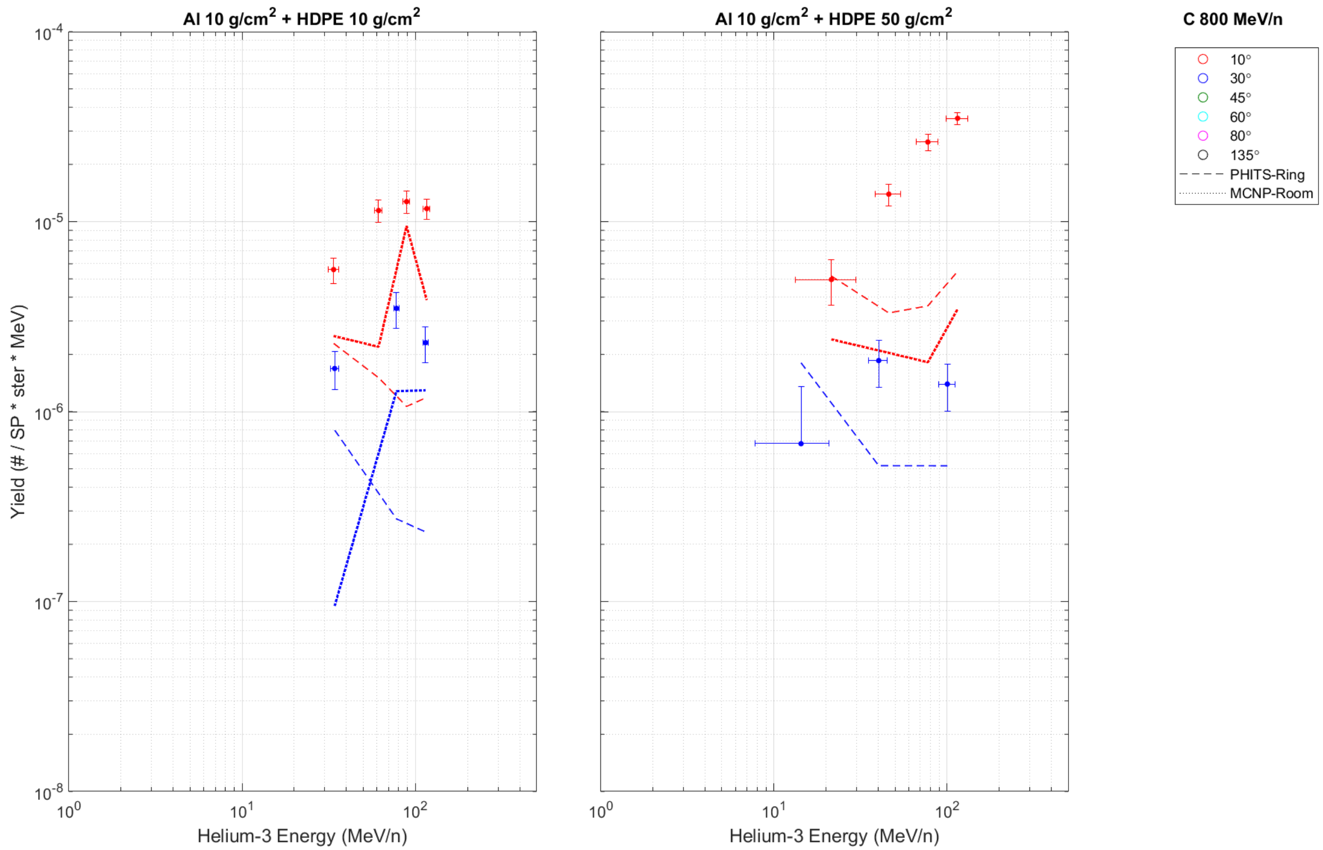

Figure 5.33. Double-differential thick-target helium-3 yields for 800 MeV/n C beam on Al+HDPE upstream target with associated PHITS ring and MCNP room simulations.

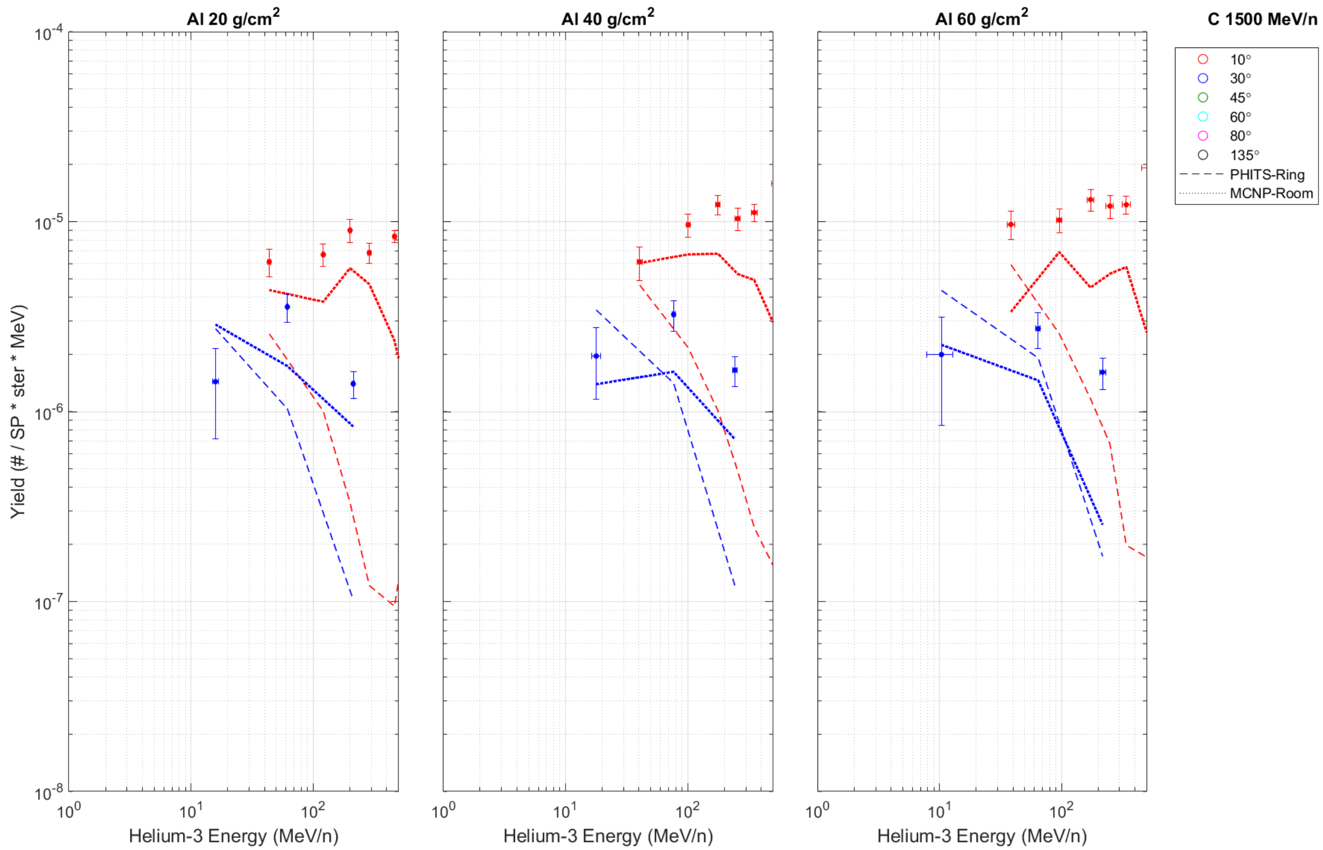

Figure 5.34. Double-differential thick-target helium-3 yields for 1500 MeV/n C beam on Al upstream target with associated PHITS ring and MCNP room simulations.

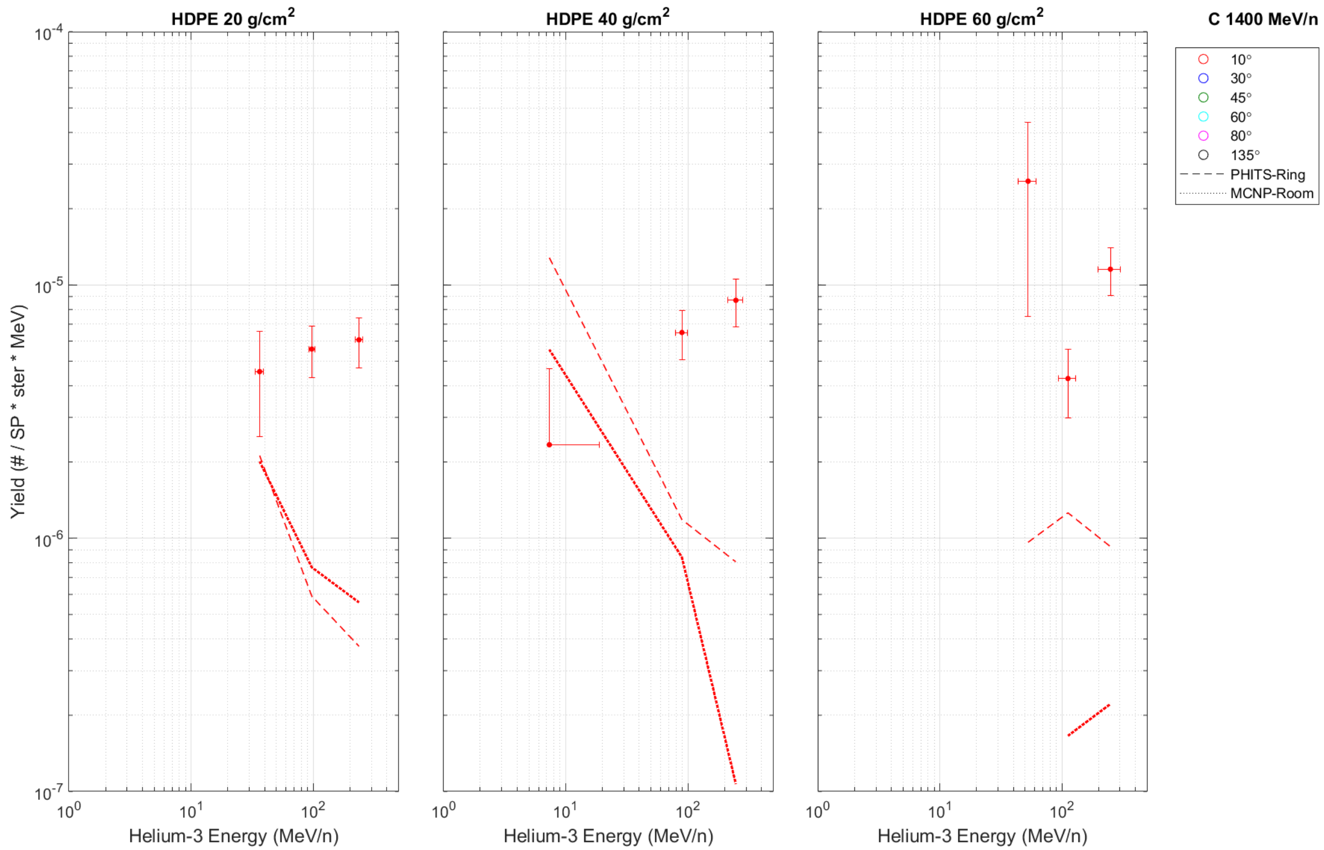

Figure 5.35. Double-differential thick-target helium-3 yields for 1400 MeV/n C beam on HDPE upstream target with associated PHITS ring and MCNP room simulations.

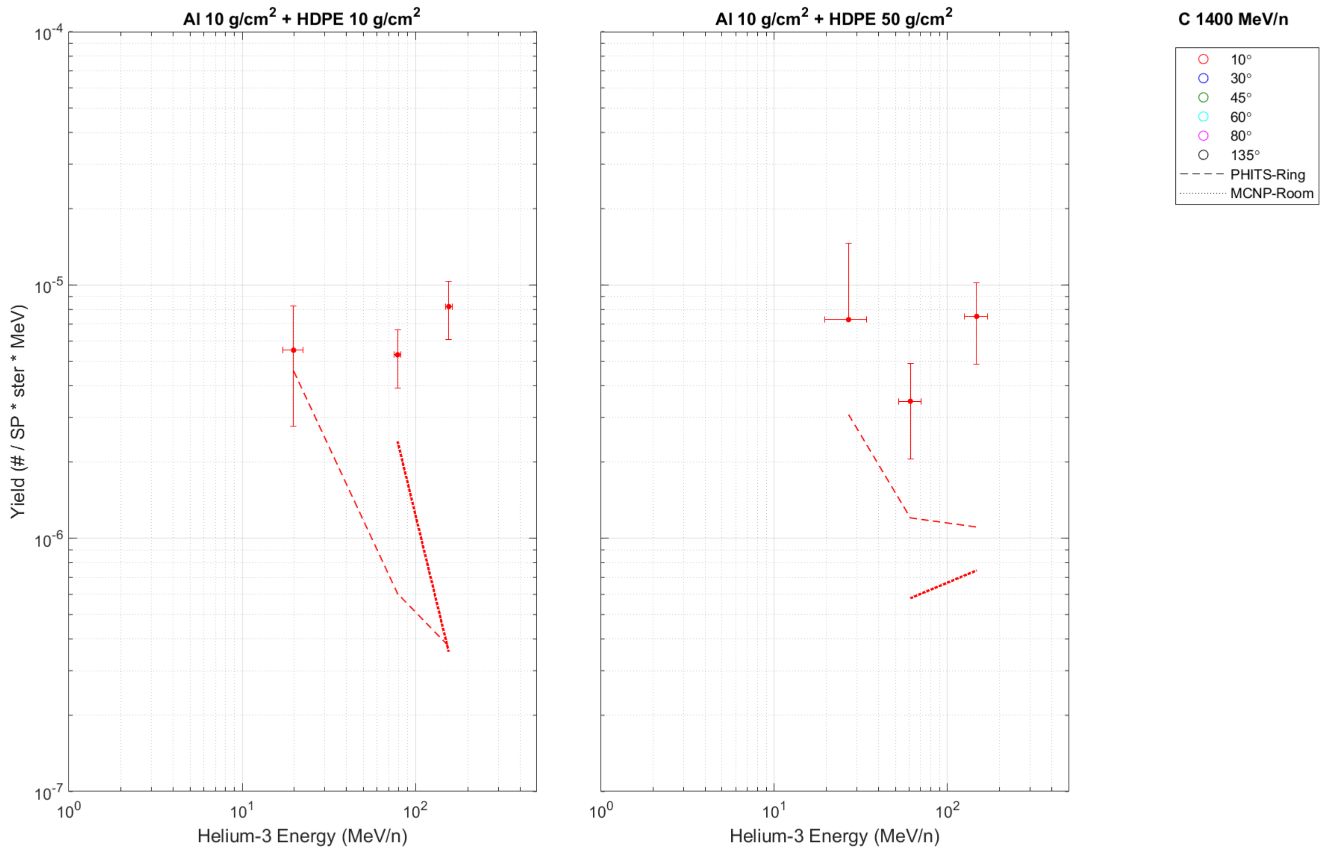

Figure 5.36. Double-differential thick-target helium-3 yields for 1400 MeV/n C beam on Al+HDPE upstream target with associated PHITS ring and MCNP room simulations.

yields for 800 and 1500 MeV/n C projectiles on three types of upstream target disagree with PHITS and MCNP simulations in either magnitude or spectral shape. It seems that PHITS and MCNP simulations both underestimated helium-3 yields most of the time but PHITS did a better job on predicting helium-3 yields for carbon projectiles on all types of upstream target than MCNP. Since carbon is a three-alpha clustering nucleus, JQMD model in PHITS might handle the breakup into helium isotopes better than LAQGSM03.03 in MCNP.

The DDTT helium-4 yield results for carbon projectiles are displayed in Figure 5.37 through Figure 5.42. For 400 MeV/n C projectiles, the PHITS ring calculations agree with the experimental helium-4 spectra in the spectral shape and magnitudes in most cases. The comparison between the experimental helium-4 yields and PHITS ring simulations for 400 MeV/n C projectiles on 20 g/cm^2 upstream target don't really agree regarding the spectral shape. Other than that, the agreement gets better in magnitudes with increasing upstream target thickness for 400 MeV/n C projectiles. For 400 MeV/n C projectiles, PHITS simulations closely predicted the experimental yields, while MCNP simulated results underestimated the magnitude of helium-4 yields by approximately 80-90%. The experimental helium-4 yields for 800 MeV/n C projectiles on three types of upstream target disagree with PHITS and MCNP simulations in either magnitude or spectral shape. For helium-4 yields from carbon projectiles on all types of upstream target, PHITS also did a better job on predicting helium-4 yields than MCNP. This might result from the same reason that PHITS predicted more closely on helium-3 yields for carbon projectiles on all types of upstream target. JQMD model in PHITS might handle the breakup of carbon nucleus into helium isotopes better than LAQGSM03.03 in MCNP.

5.2.2 Discussion

The proton yields are generally over-estimated or well-reproduced by simulations in both the spectral shape and the magnitude across each beam projectile and energy system. For

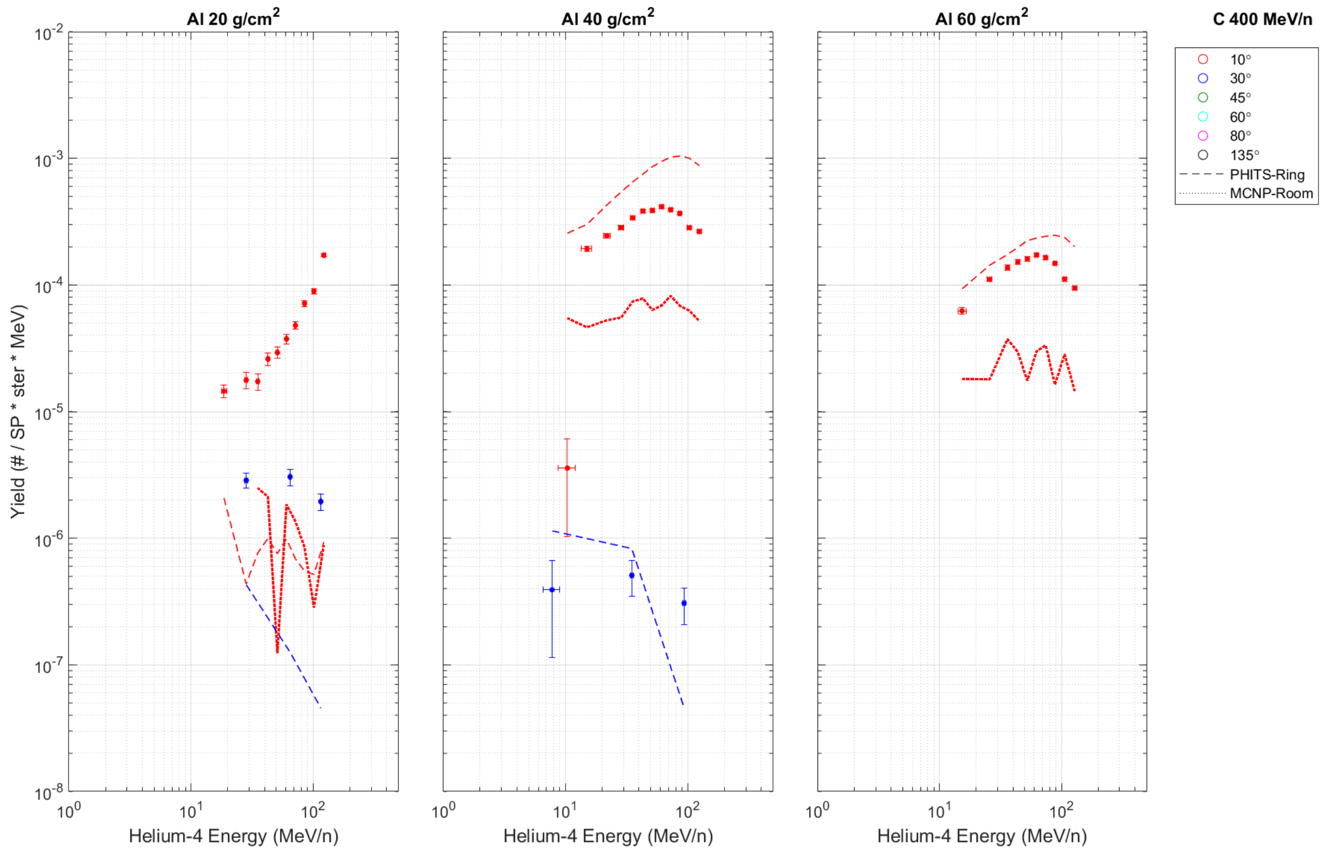

Figure 5.37. Double-differential thick-target helium-4 yields for 400 MeV/n C beam on Al upstream target with associated PHITS ring and MCNP room simulations.

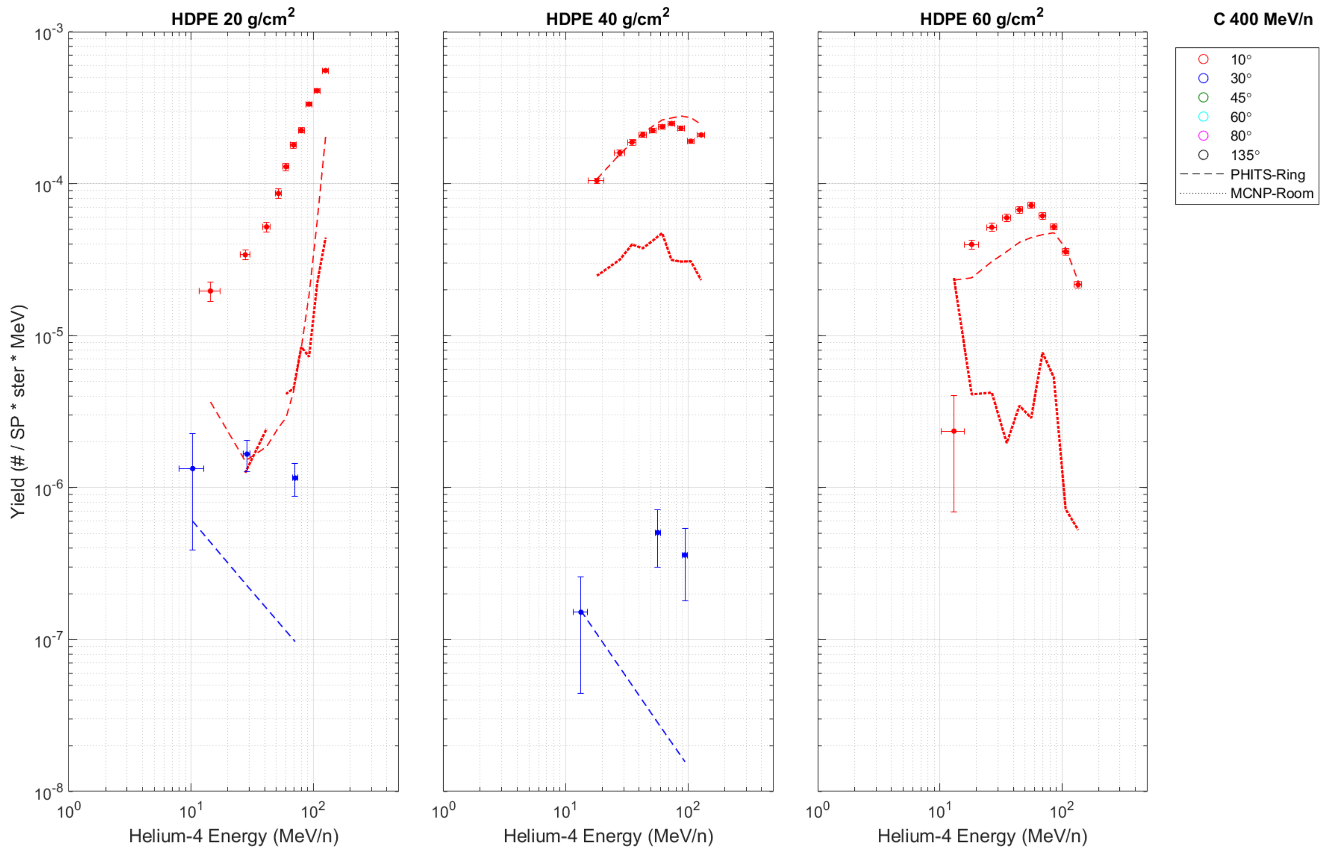

Figure 5.38. Double-differential thick-target helium-4 yields for 400 MeV/n C beam on HDPE upstream target with associated PHITS ring and MCNP room simulations.

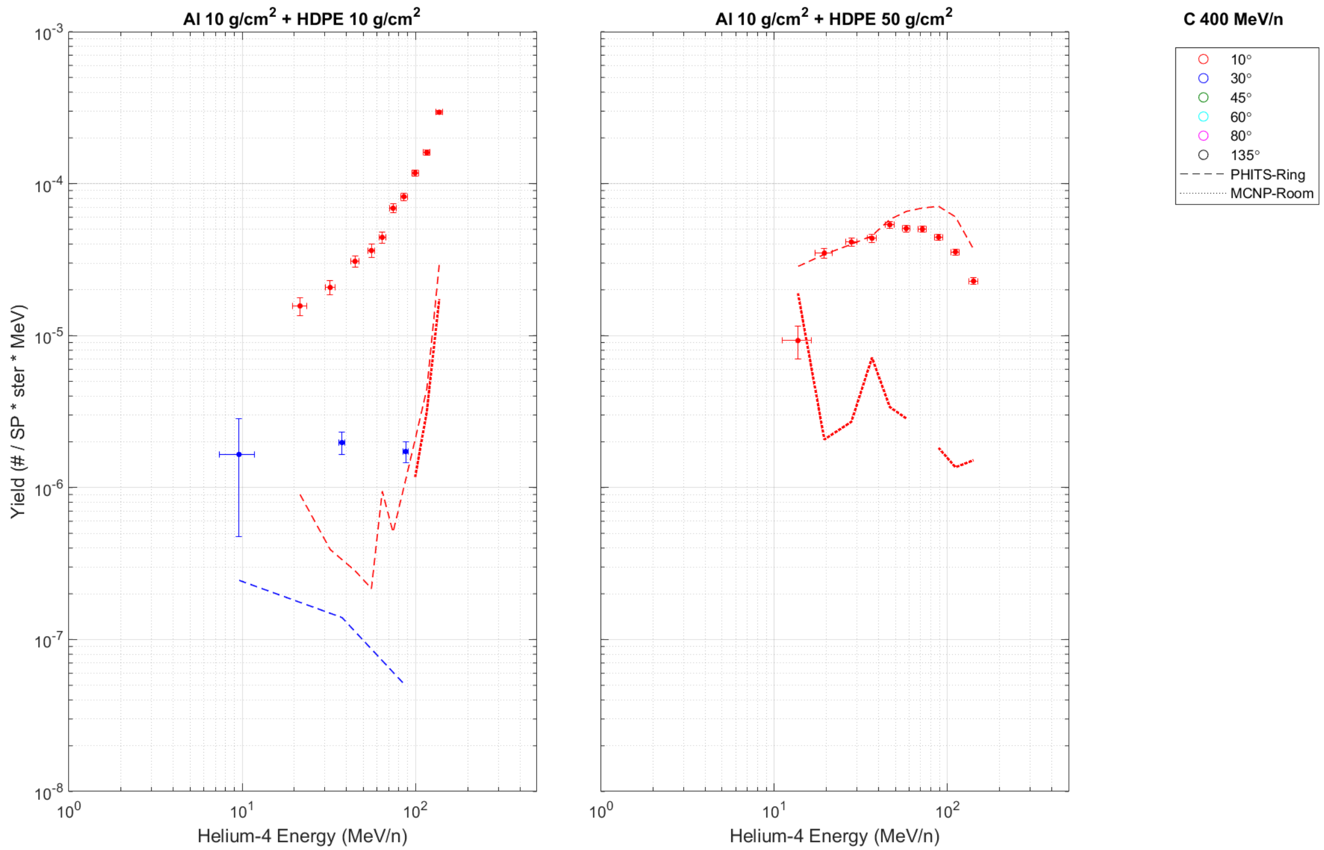

Figure 5.39. Double-differential thick-target helium-4 yields for 400 MeV/n C beam on Al+HDPE upstream target with associated PHITS ring and MCNP room simulations.

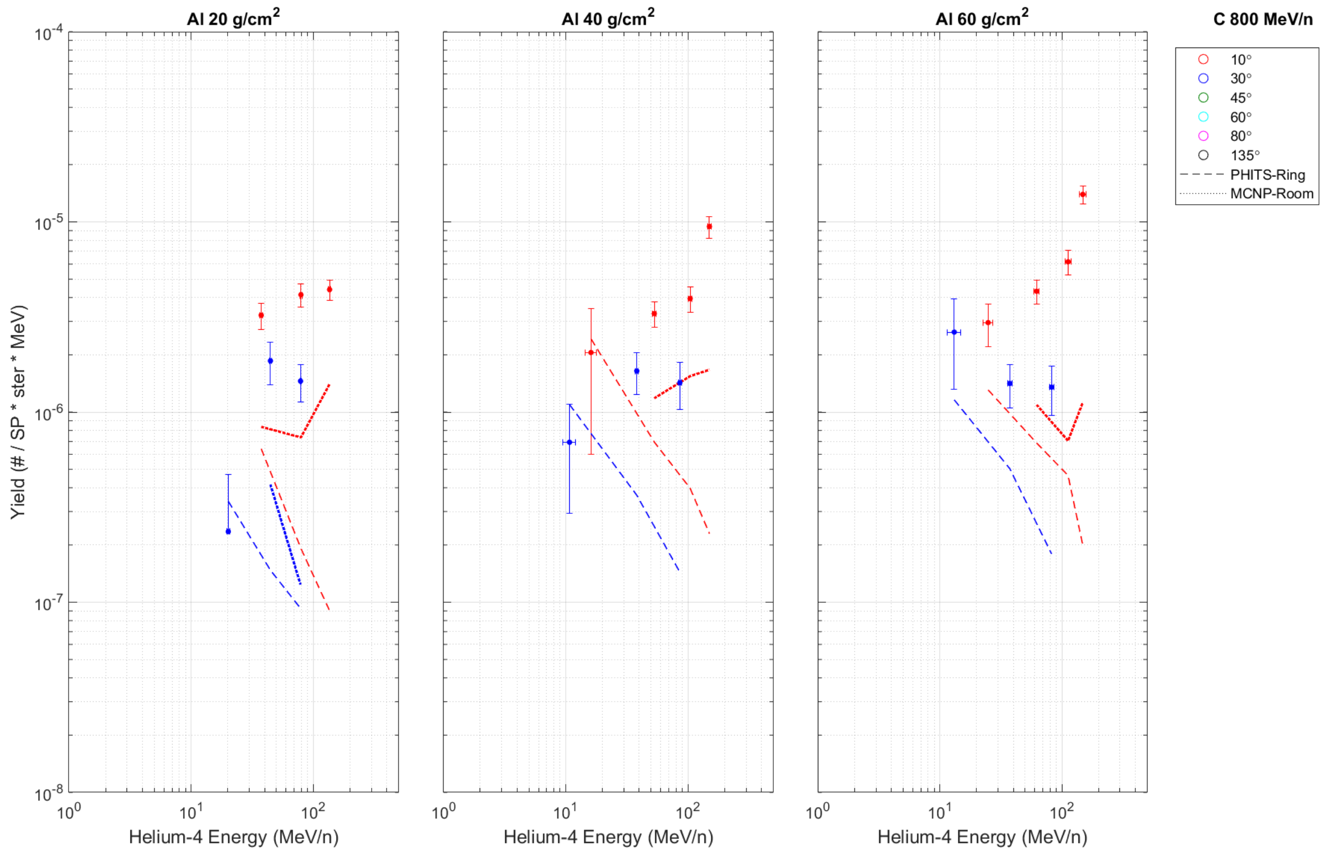

Figure 5.40. Double-differential thick-target helium-4 yields for 800 MeV/n C beam on Al upstream target with associated PHITS ring and MCNP room simulations.

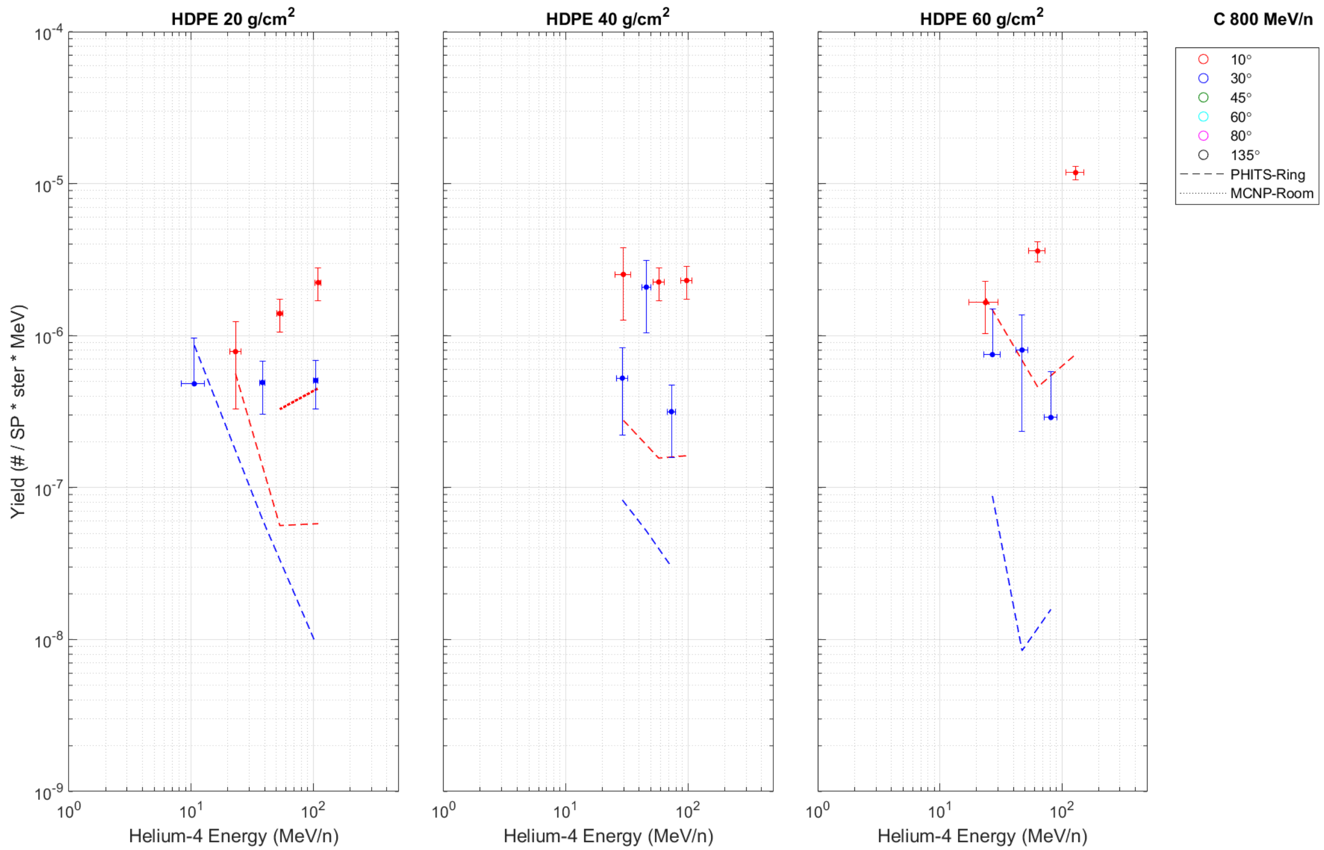

Figure 5.41. Double-differential thick-target helium-4 yields for 800 MeV/n C beam on HDPE upstream target with associated PHITS ring and MCNP room simulations.

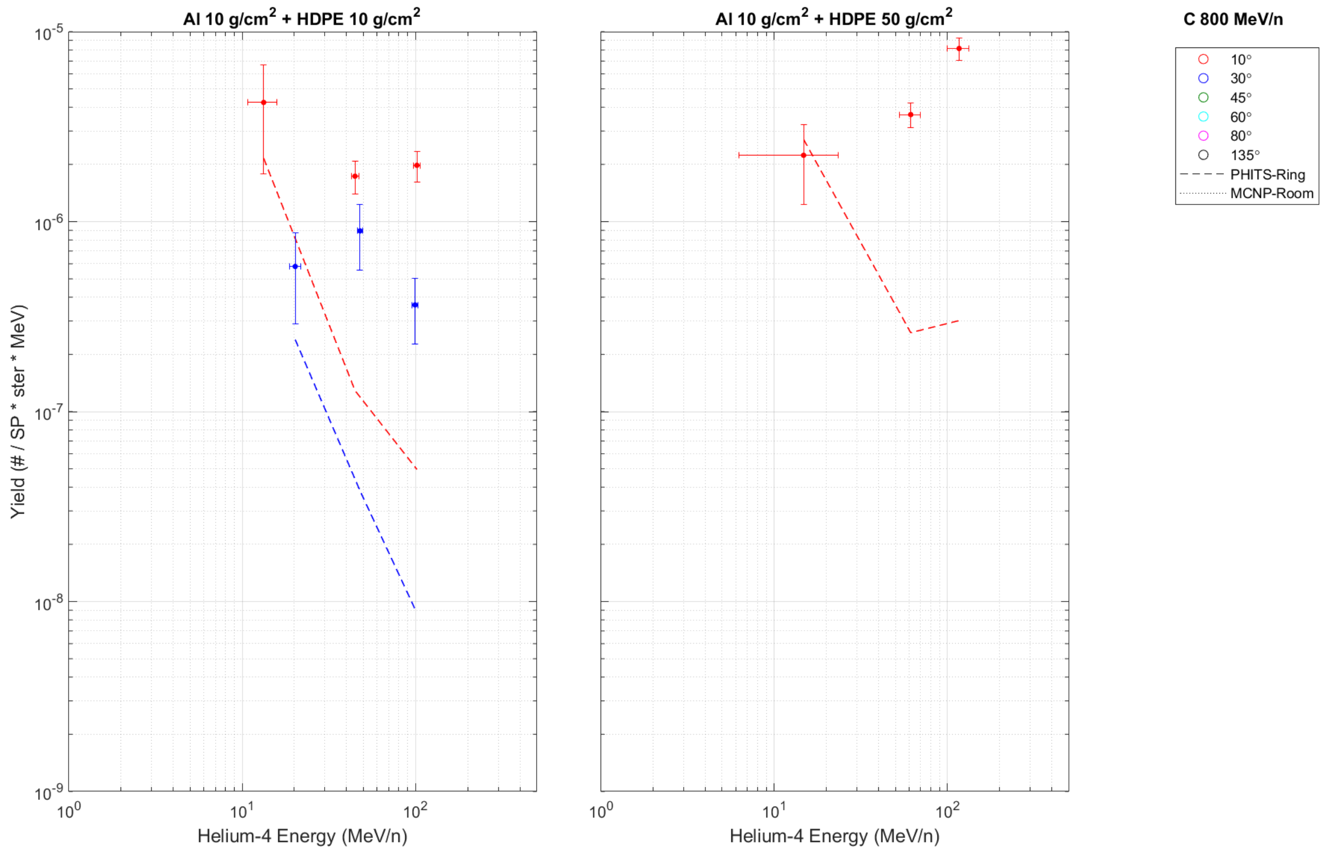

Figure 5.42. Double-differential thick-target helium-4 yields for 800 MeV/n C beam on Al+HDPE upstream target with associated PHITS ring and MCNP room simulations.

the complex light ions, the simulations can predict better at the forward detection angles (10° and 30° for deuteron and triton, 10° for helium-3 and helium-4).

Figure 5.43 to Figure 5.47 show the proton yield ratios of Monte Carlo simulations to experimental results for all analyzed 400 MeV/n beam and target combination systems, which reveals the proton well-reproduction or over-estimation in most of the cases by the Monte Carlo simulations. On the other hand, the complex light ion (deuteron, triton, helium-3, and helium-4) yields are generally under-estimated by the simulations, which can be seen in Figure 5.48 (using helium-4 yield ratios as an example). As discussed in the previous sub-section, the proton over-estimation and complex light ion under-estimation might result from poor coalescence incorporated into PHITS and MCNP.

Figure 5.48 also shows that PHITS does a better job at predicting helium-4 yields than MCNP. Pre-equilibrium emission of deuteron, triton, helium-3, and helium-4 is the dominant mechanism for production of those ions. The INCL model incorporated into PHITS can describe pre-equilibrium interactions [33]. However, the INCL version implemented in MCNP6 does not consider pre-equilibrium interactions, so MCNP uses Modified Exciton Model (MEM) to describe pre-equilibrium interactions [37]. Also, MCNP6 considers fermi breakup of excited or unstable nuclei with mass numbers up to 12. These two model differences might be responsible for the results that PHITS more closely predicts helium-4 yields than MCNP.

For 39 analyzed systems, as the mass number of incoming beam projectile increases, the agreement between the experimental and simulated results generally improves. Figure 5.49 shows the proton yield ratios of Monte Carlo simulations to experimental results for 400 MeV/n carbon and iron beam and target combination systems. In Figure 5.49, the yield ratios of iron projectile data are closer to 1 than the yield ratios of carbon projectile data. The difference in magnitude between experimental and simulated results reduces with increasing upstream target thickness in most cases. Also, both PHITS and MCNP do a

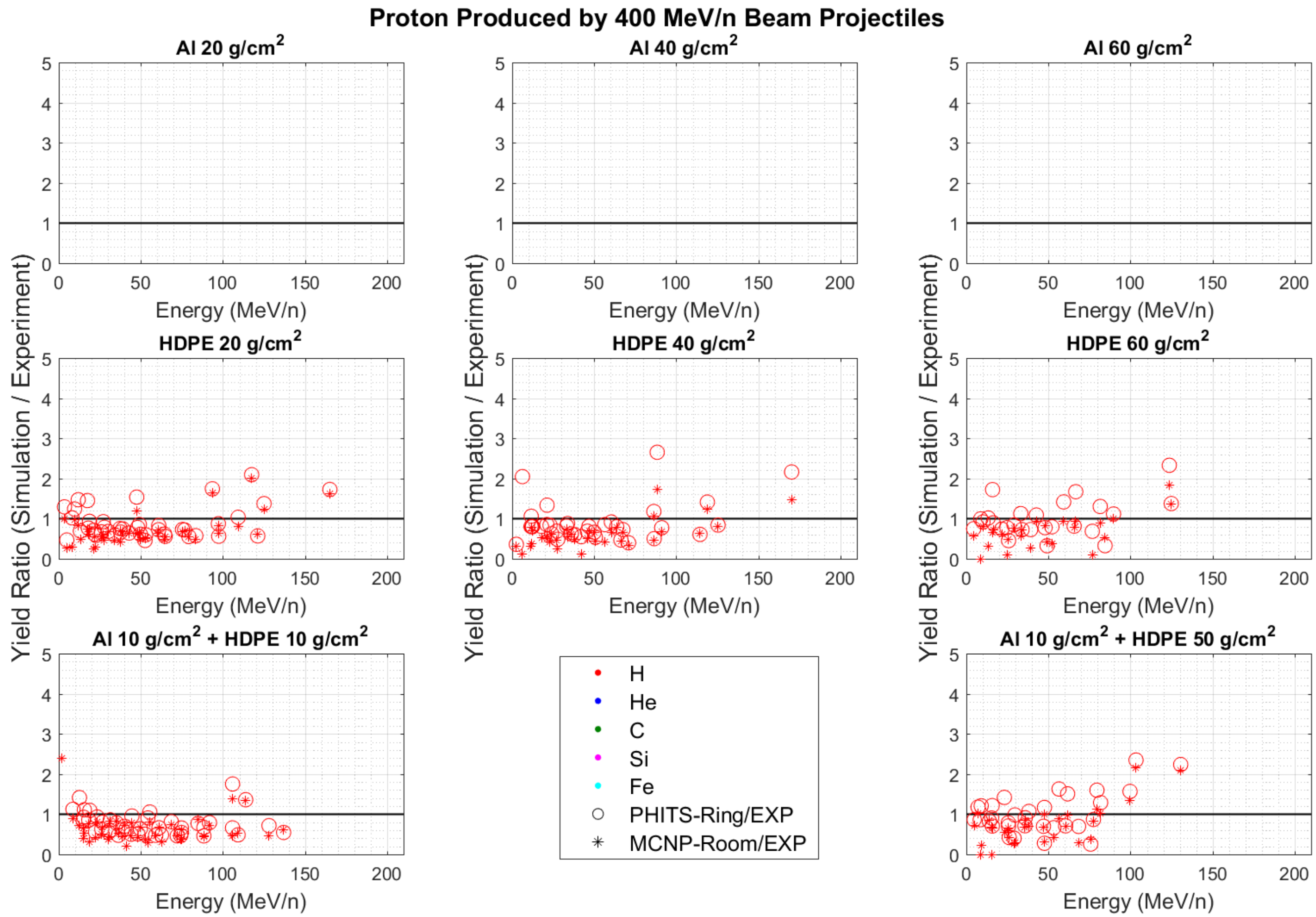

Figure 5.43. Proton yield ratios of Monte Carlo simulations to experimental results for 400 MeV/n proton beam projectiles on Al, HDPE, and Al+HDPE upstream target.

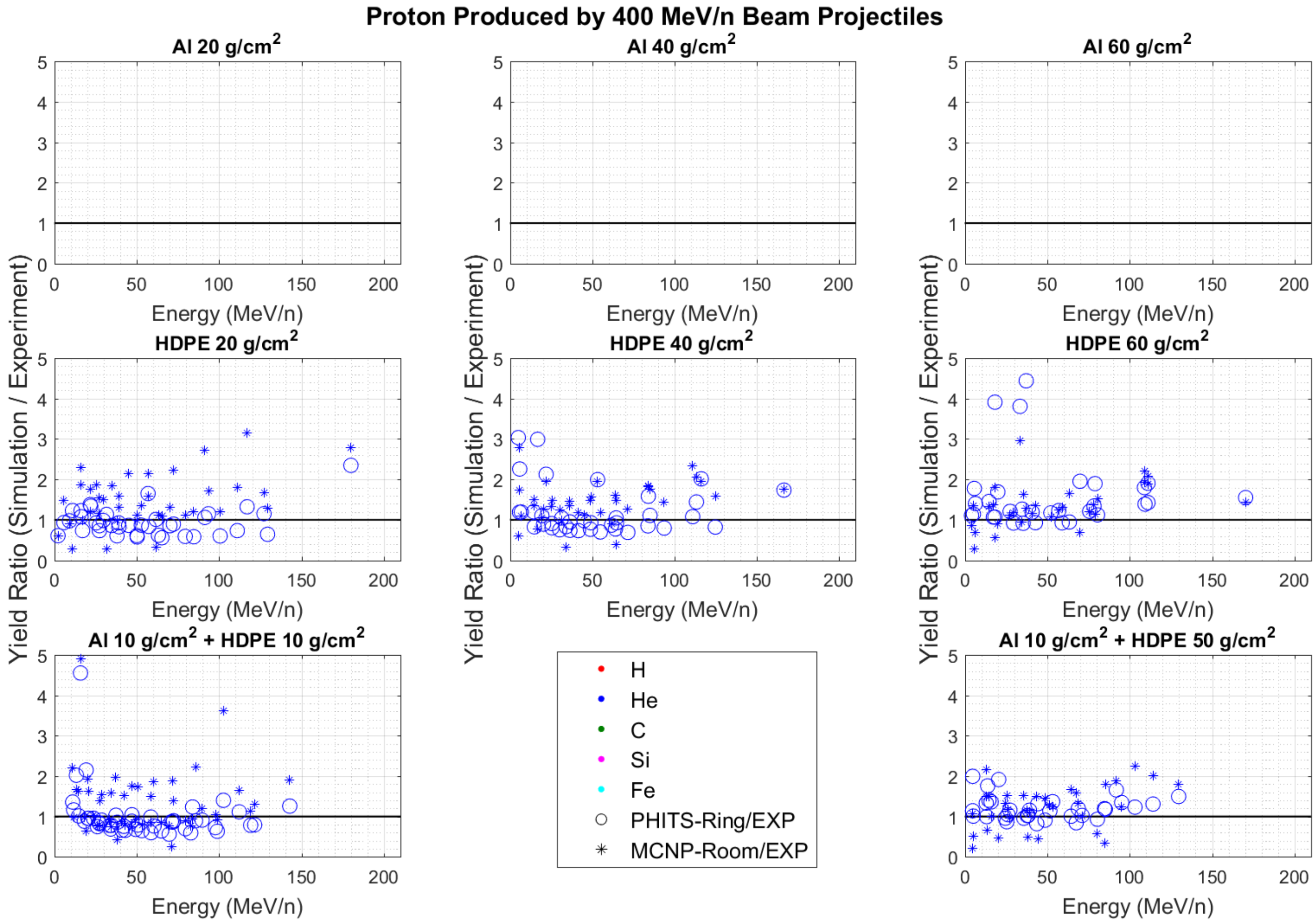

Figure 5.44. Proton yield ratios of Monte Carlo simulations to experimental results for 400 MeV/n beam projectiles on Al, HDPE, and Al+HDPE upstream target.

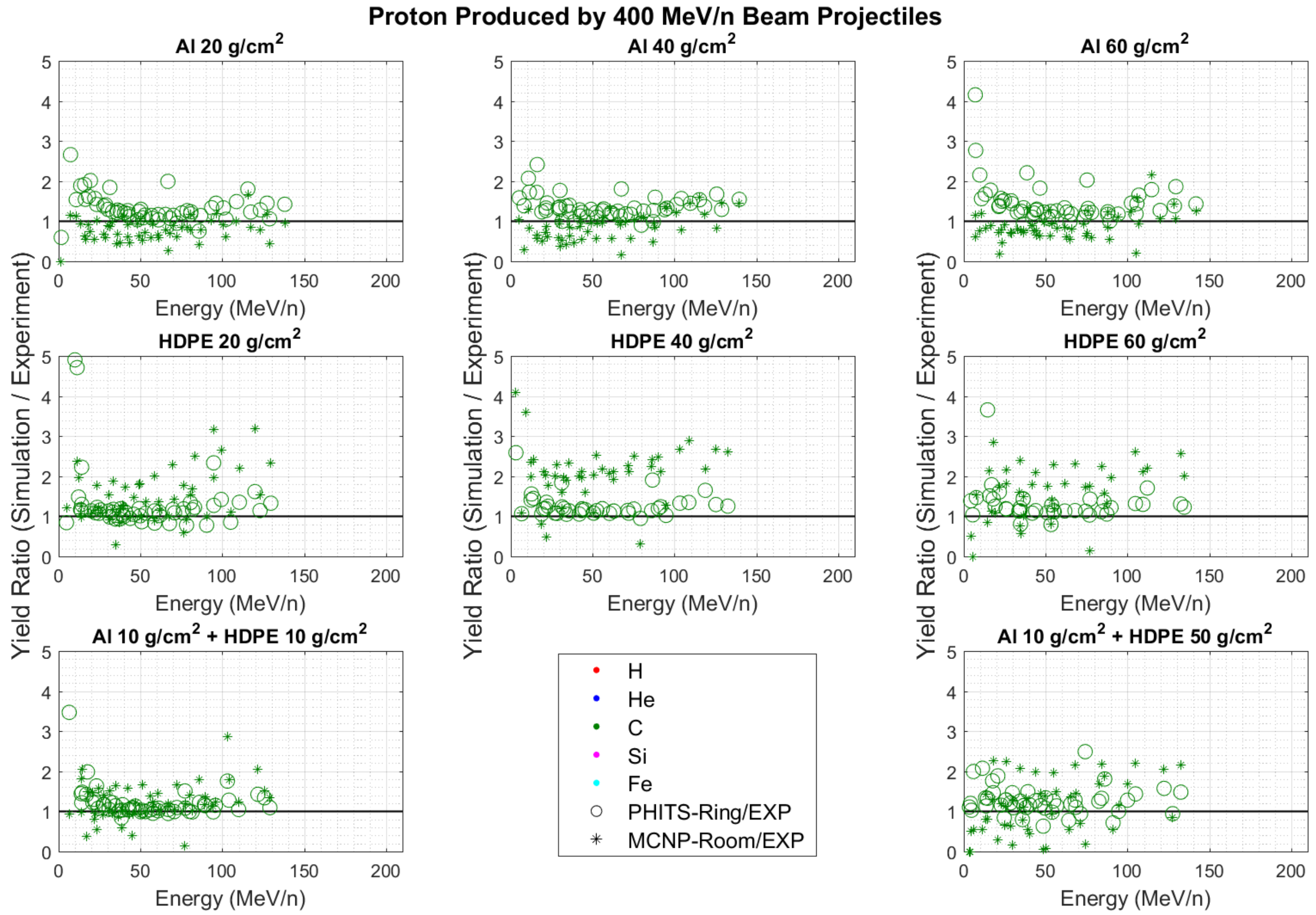

Figure 5.45. Proton yield ratios of Monte Carlo simulations to experimental results for 400 MeV/n carbon beam projectiles on Al, HDPE, and Al+HDPE upstream target.

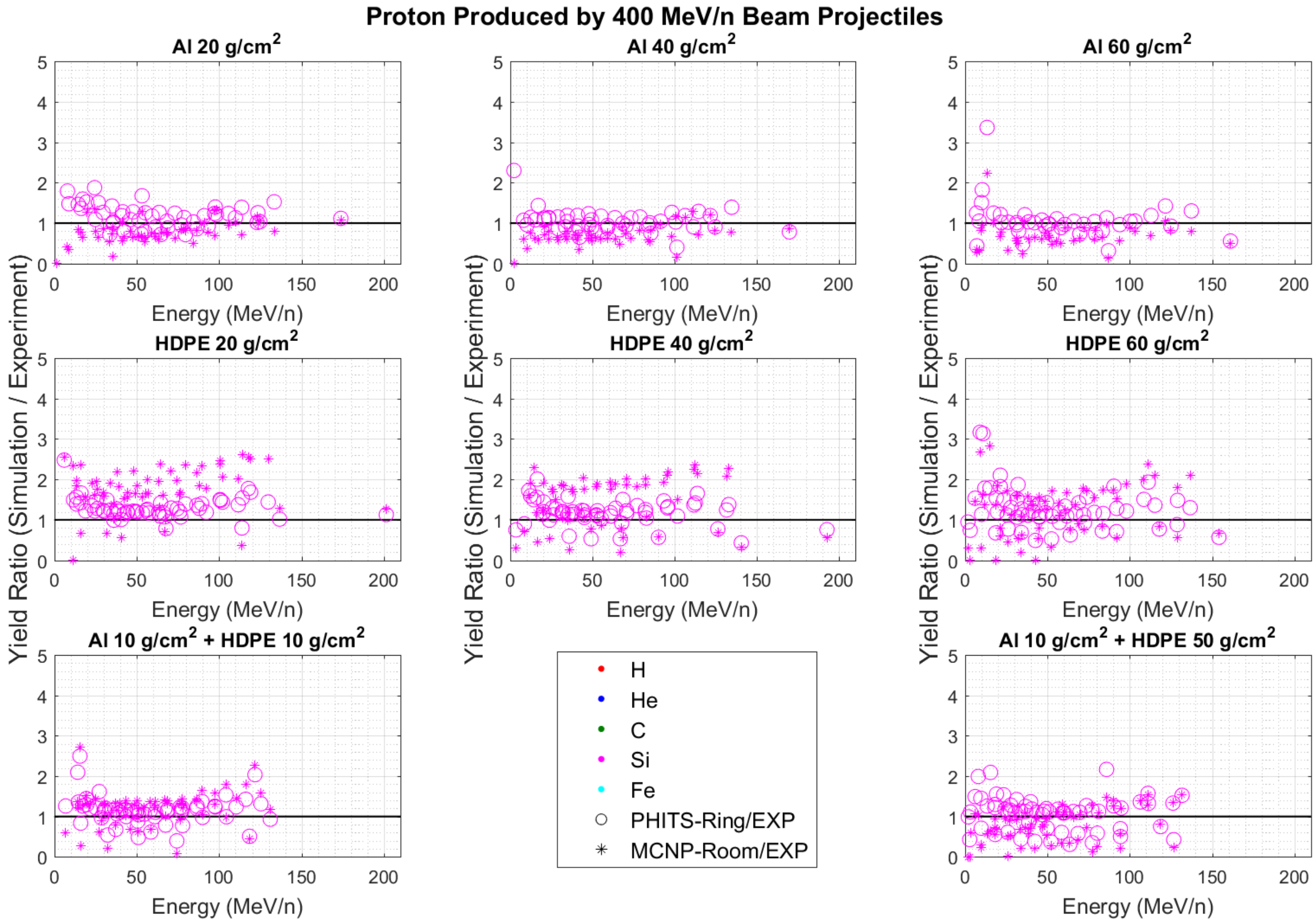

Figure 5.46. Proton yield ratios of Monte Carlo simulations to experimental results for 400 MeV/n silicon beam projectiles on Al, HDPE, and Al+HDPE upstream target.

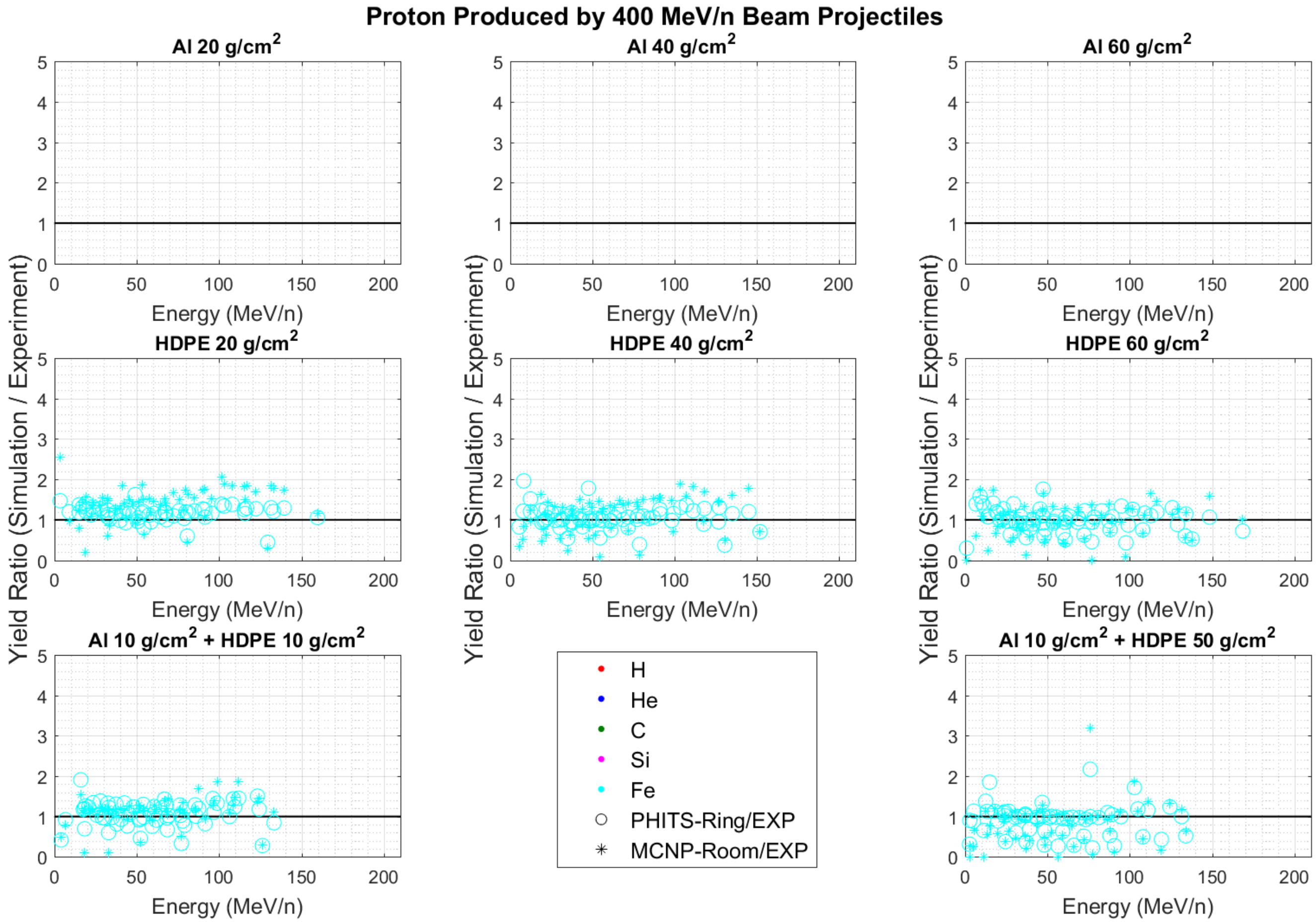

Figure 5.47. Proton yield ratios of Monte Carlo simulations to experimental results for 400 MeV/n iron beam projectiles on Al, HDPE, and Al+HDPE upstream target.

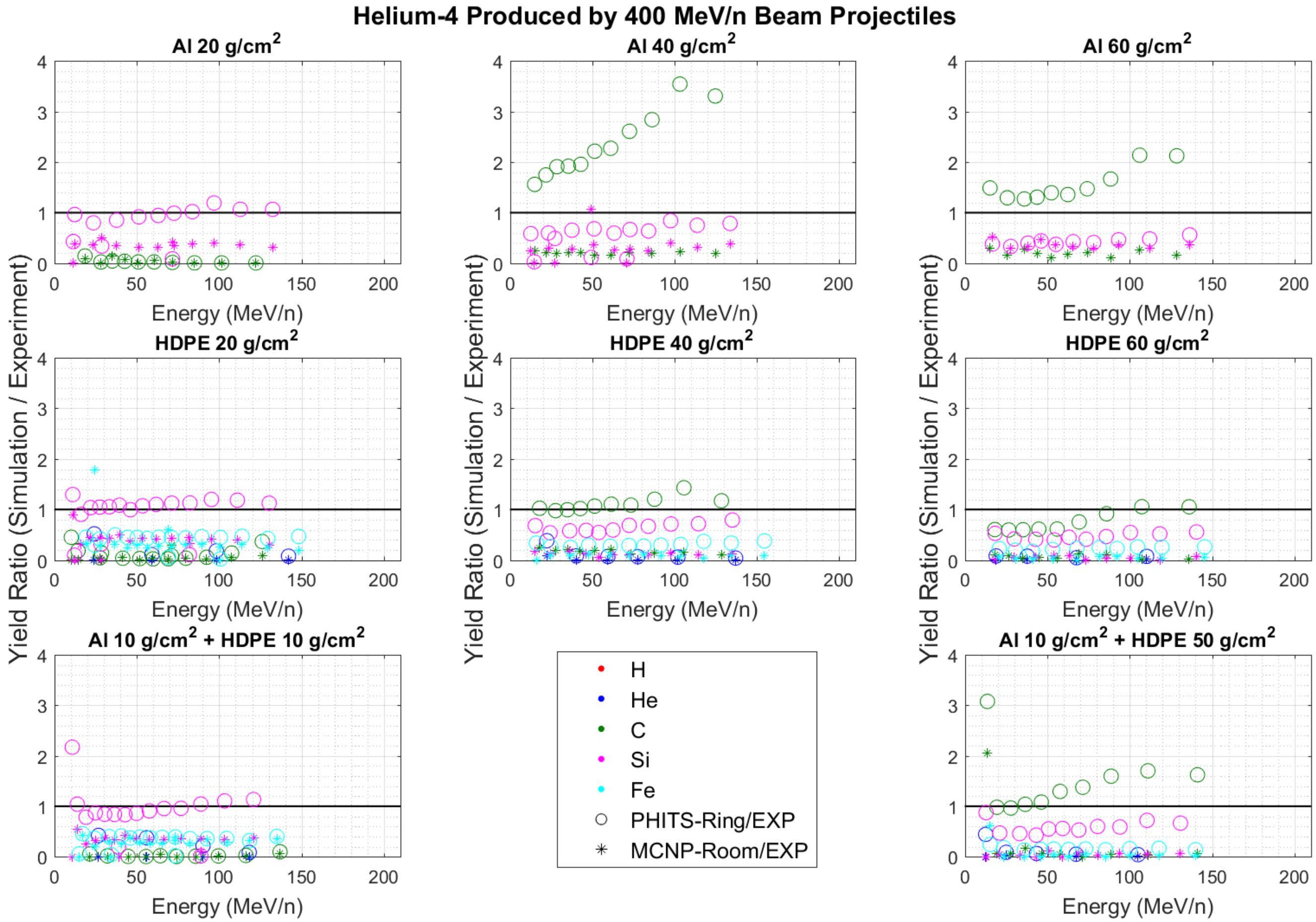

Figure 5.48. Helium-4 yield ratios of Monte Carlo simulations to experimental results for 400 MeV/n beam projectiles on Al, HDPE, and Al+HDPE upstream target.

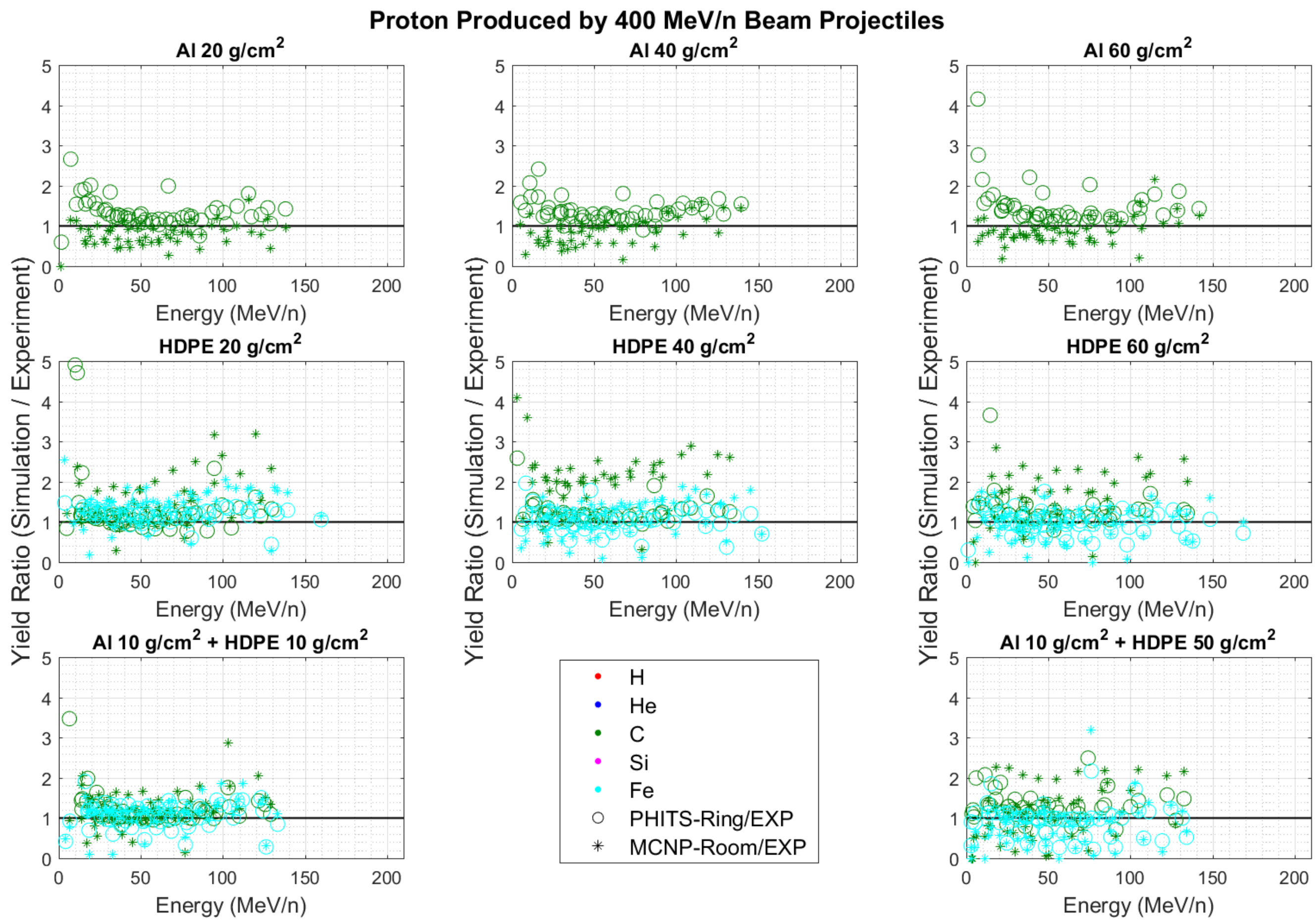

Figure 5.49. Proton yield ratios of Monte Carlo simulations to experimental results for 400 MeV/n C and Fe beam projectiles on Al, HDPE, and Al+HDPE upstream target.

better job when the incoming projectile energies are 400 and 800 MeV/n. This might result from the higher energy runs required longer measurement time to get even better statistics. Even though all the analyzed systems presented in this dissertation were able to get at least three data points in each spectrum, longer measurement time could still advance the quality of the data.

Comparisons of PHITS and MCNP simulated results with experimental data provide interesting findings: 1) PHITS simulations generally overestimate the light charged particle yields for the Al upstream target and underestimate for the HDPE upstream target, 2) MCNP simulations typically underestimate the light charged particle yields for the Al upstream target and overestimate for the HDPE upstream target, and 3) for Al upstream target, MCNP normally does better prediction on light charged particle yields than PHITS, while PHITS mostly predict more closely for HDPE upstream target. Since there will be multiple interactions within the upstream target in thick-target measurements, it is difficult to point out the simple cause of disagreement between experimental and simulated results. This illustrates that the major purposes of thick-target measurements are benchmark and uncertainty quantification of transport codes.

5.3 Dose Equivalent Results

5.3.1 Overview

The dose equivalent results were calculated from the experimental DDTT light charged particle yields. Since the dynamic range of the analyzed spectra is approximately the same for each light charged particle, the dose equivalents are closely related to the amount of measured yields. Therefore, comparisons of dose equivalents across the beam projectiles, target materials, and target thicknesses can also provide a sense of measured light charged particle yield comparisons.

For all light charged particle dose equivalent results, proton and helium-4 dose equivalents are the first and second highest dose equivalent contributors to the total dose equivalents behind thick shields accordingly. Thus, the following section discusses proton and helium-4 dose equivalent results for carbon projectile systems to illustrate the trends for all the datasets.

Each dose equivalent plot shows the total dose equivalent (Sv/Source particle) calculated by using three different quality factors ($Q_{NASA} Solid\ Cancers$, $Q_{NASA} Leukemia$, and $Q_{ICRP-60}$) on the left y-axis versus the upstream target thickness. The ratio of dose equivalent values calculated by using $Q_{ICRP-60}$ to $Q_{NASA} Solid\ Cancers$ is presented on the right y-axis of each dose equivalent plot. The error bars presented in these plots are the uncertainties resulted from the energy uncertainties in the DDTT light charged particle yield spectra.

5.3.2 Dose Equivalents

The proton dose equivalents using different quality factors are generally the same. On the other hand, the helium-4 dose equivalent results using ICRP-60 quality factor are generally higher than the results using NASA quality factors (mostly within 18% difference), but helium-4 dose equivalent results using different quality factors still present similar trend across target materials and target thicknesses. Also, the helium-4 dose equivalent results show the trend similar to the proton dose equivalent results. Therefore, the following discussion will be focusing on comparing proton dose equivalents across the beam projectiles, target materials, and target thicknesses. The proton dose equivalent results for carbon projectile systems are displayed in Figure 5.50 through Figure 5.58.

For 400 MeV/n C projectiles, the proton dose equivalent increased from 20 to 40 g/cm^2 and then decreased. It is because the 400 MeV/n C projectiles stopped in 40 g/cm^2, those secondary particles produced in the first 40 g/cm^2 were moderated by the remaining target material on the flight path for 60 g/cm^2 thick target. For 800 MeV/n C projectiles, the proton dose equivalents are increased by approximately a factor of 2 as the target thickness increases from 20 to 60 g/cm^2. For 1500 MeV/n C projectiles, the proton dose equivalents

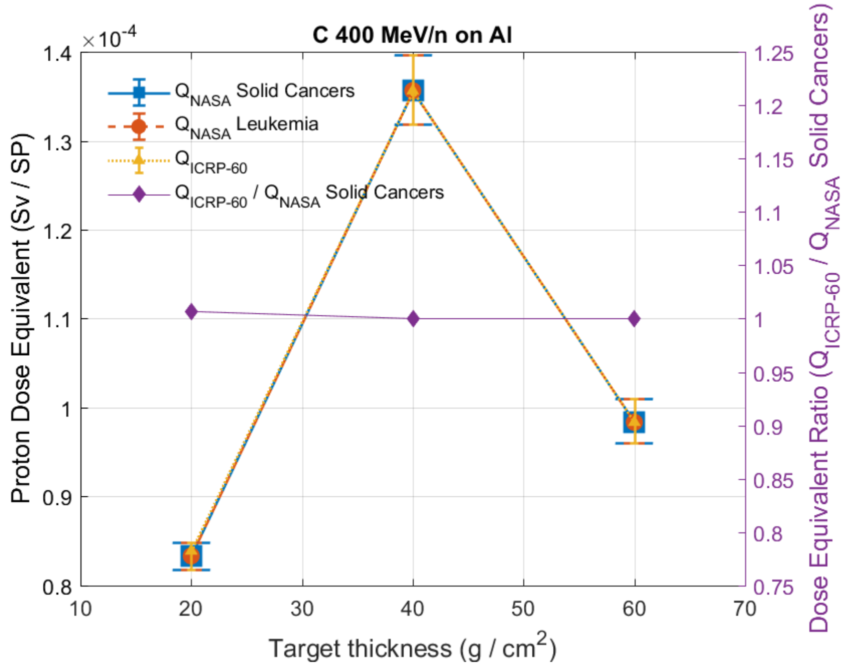

Figure 5.50. Proton dose equivalent results using ICRP-60 quality factor and the NASA quality factors for 400 MeV/n C beam on Al upstream target.

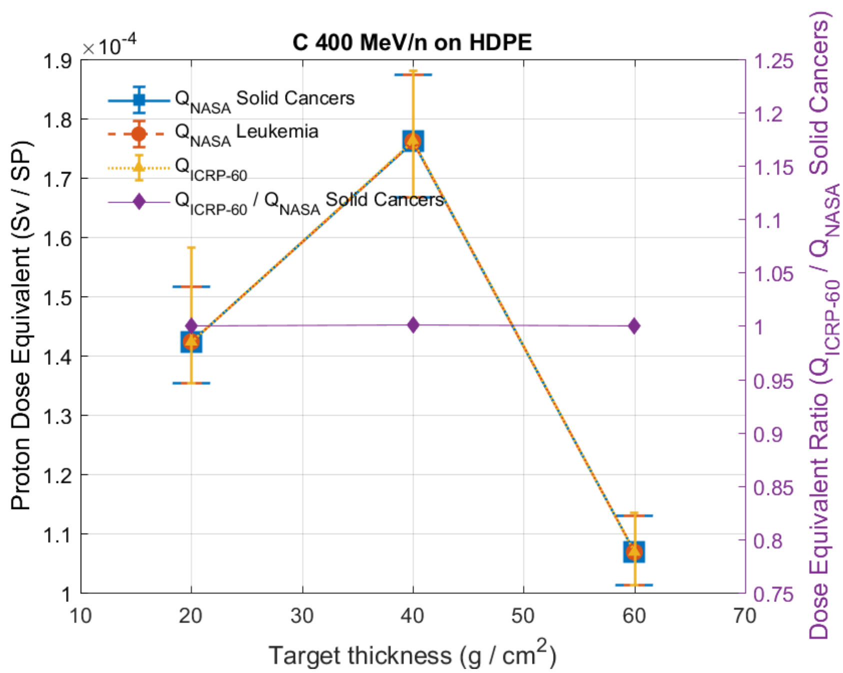

Figure 5.51. Proton dose equivalent results using ICRP-60 quality factor and the NASA quality factors for 400 MeV/n C beam on HDPE upstream target.

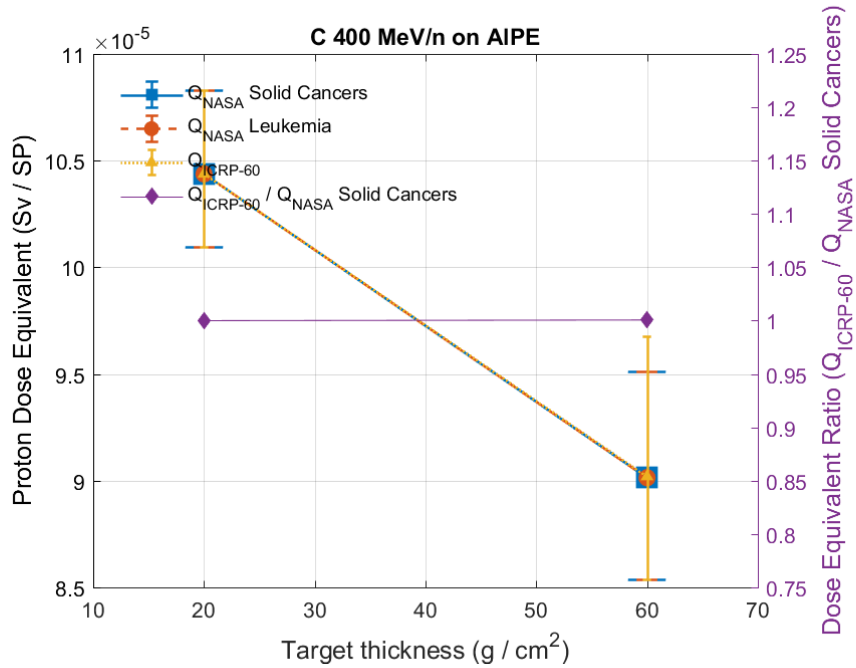

Figure 5.52. Proton dose equivalent results using ICRP-60 quality factor and the NASA quality factors for 400 MeV/n C beam on Al+HDPE upstream target.

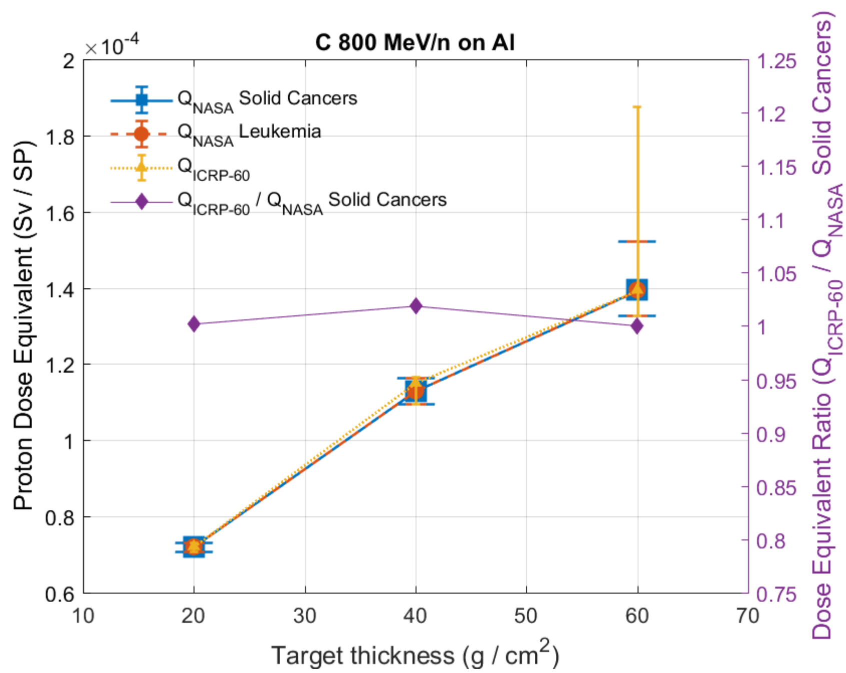

Figure 5.53. Proton dose equivalent results using ICRP-60 quality factor and the NASA quality factors for 800 MeV/n C beam on Al upstream target.

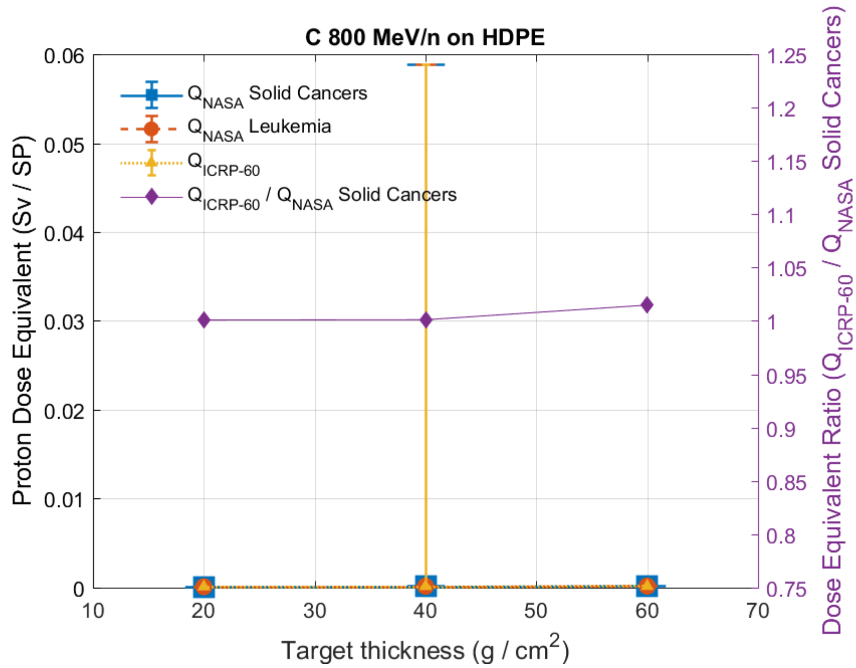

Figure 5.54. Proton dose equivalent results using ICRP-60 quality factor and the NASA quality factors for 800 MeV/n C beam on HDPE upstream target.

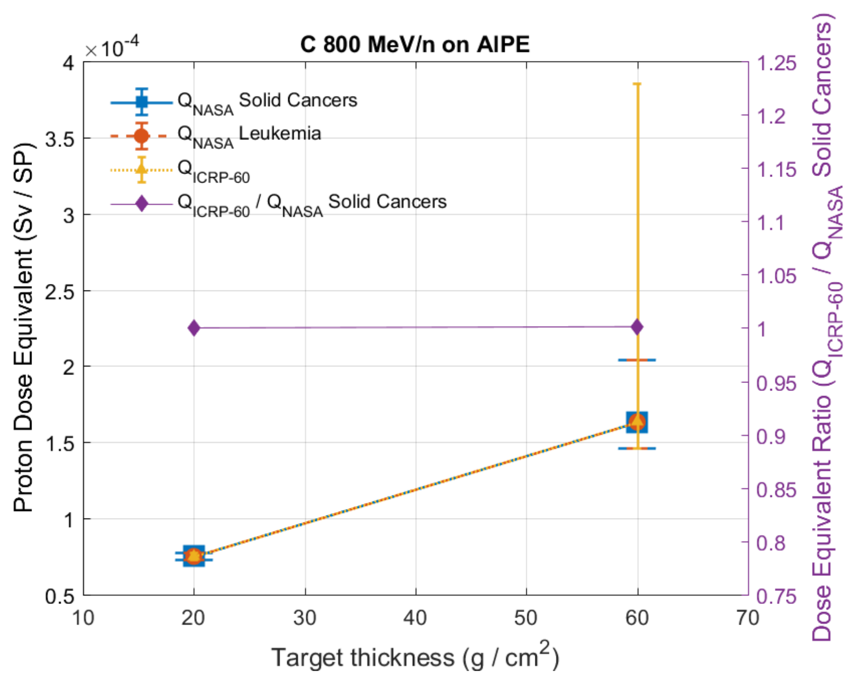

Figure 5.55. Proton dose equivalent results using ICRP-60 quality factor and the NASA quality factors for 800 MeV/n C beam on Al+HDPE upstream target.

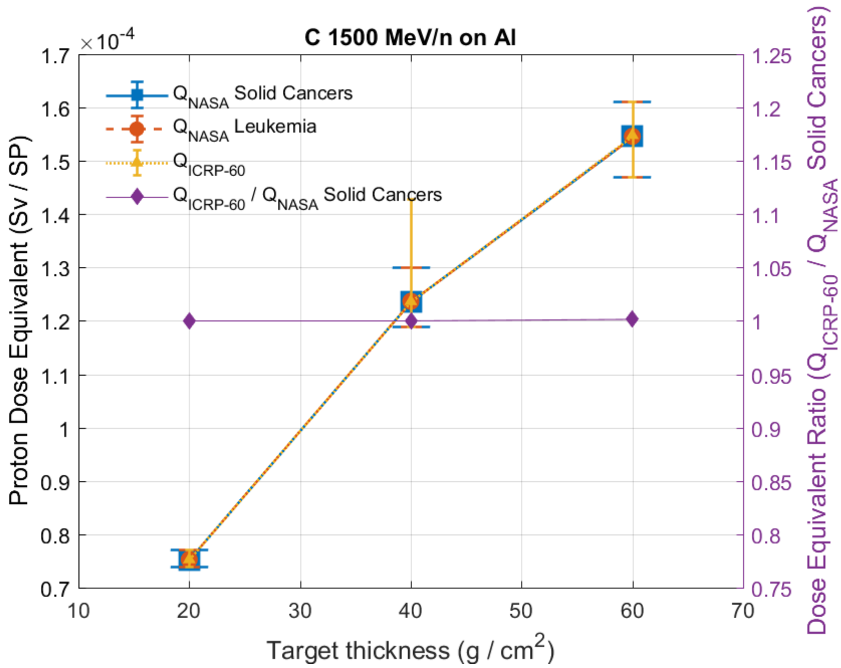

Figure 5.56. Proton dose equivalent results using ICRP-60 quality factor and the NASA quality factors for 1500 MeV/n C beam on Al upstream target.

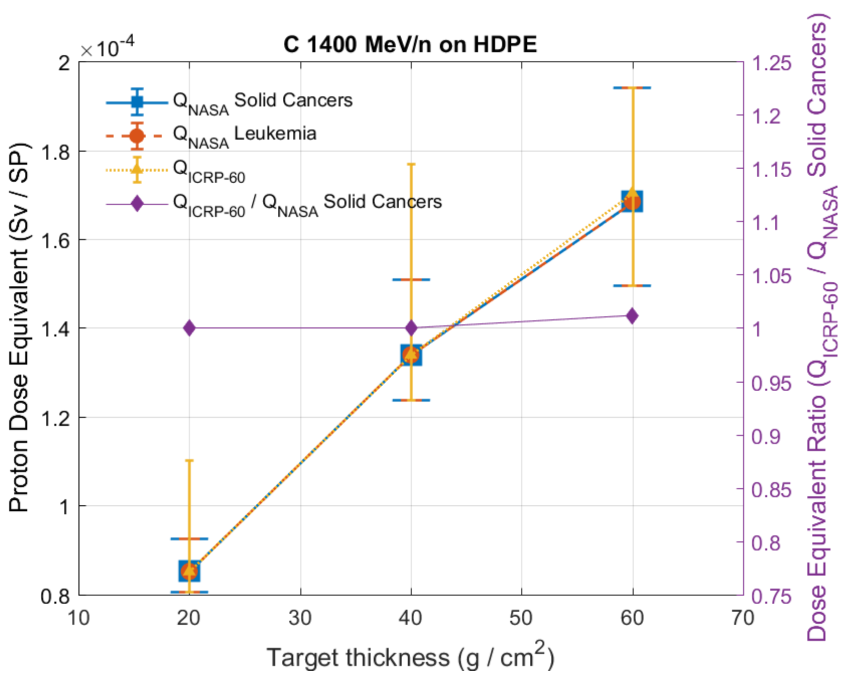

Figure 5.57. Proton dose equivalent results using ICRP-60 quality factor and the NASA quality factors for 1400 MeV/n C beam on HDPE upstream target.

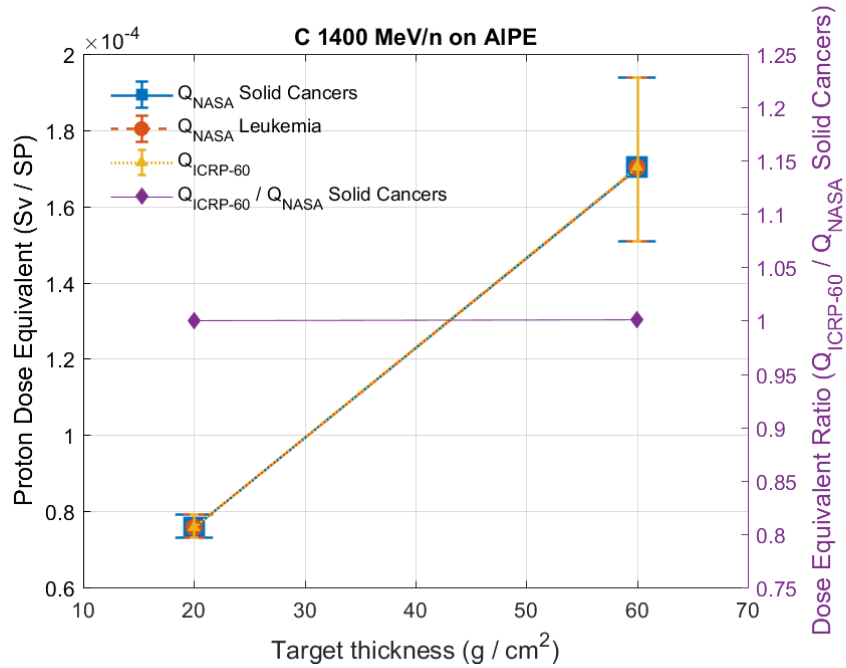

Figure 5.58. Proton dose equivalent results using ICRP-60 quality factor and the NASA quality factors for 1400 MeV/n C beam on Al+HDPE upstream target.

are increased by about a factor of 2.2 as the target thickness increases from 20 to 60 g/cm^2. Additionally, the proton dose equivalents are higher for HDPE upstream target. The proton dose equivalent has higher value for 400 MeV/n C projectiles for the certain target material and thickness.

5.3.3 Discussions

For HDPE upstream target systems, the proton dose equivalents are higher by magnitude than systems with Al and Al+HDPE upstream targets when comparing at a given beam and energy. The proton dose equivalent for those systems with beam projectile's energy that can punch through 60 g/cm^2 thick upstream target would increase as the target thickness increases because increasing shielding material provides more possible interactions as the beam projectiles traverse the upstream target. Also, the proton dose equivalents increase with increasing beam projectile mass number since the projectile fragmentation is the main source of the secondary charged particle. Generally, the proton dose equivalents present similar systematic trend to the experimental proton yields.

In terms of the differences between $Q_{NASA}Solid\ Cancers$ and $Q_{ICRP-60}$, the purple line in each dose equivalent plot presents the ratio of total dose equivalent values calculated using $Q_{ICRP-60}$ to using $Q_{NASA}Solid\ Cancers$. For proton dose equivalent results, the fractional difference between using these two quality factors is mostly less than 1%. The fractional difference between using these two quality factors for helium-4 dose equivalent results is generally within 18%. However, a few fractional difference data points of helium-4 dose equivalent results are between 25-50%.

CHAPTER SIX
CONCLUSIONS AND FUTURE WORK

This dissertation presents the datasets of secondary light charged particle measurements conducted and personally attended in November 2016 and November 2017 at the NASA Space Radiation Laboratory (NSRL) facility at Brookhaven National Laboratory. The secondary charged particles produced by 400-, 800-, and 2500-MeV protons and 400-, 800-, and 1500-MeV/n He, C, Si, Fe ions bombarding thick targets (20, 40, and 60 g/cm^2 aluminum and high-density polyethylene (HDPE), and 20 and 60 g/cm^2 combination of aluminum and HDPE) with an additional 60 g/cm^2 thick downstream target (aluminum or HDPE) placed 3.5 m from the middle of the upstream target were measured with organic liquid scintillators. The placements of the second 60 g/cm^2 downstream target in the experiments performed for this dissertation is unique. Double-differential thick-target (DDTT) yields were analyzed for protons measured at 10°, 30°, 45°, 60°, 80°, and 135° with respect to the beam direction and the middle of upstream target, deuterons detected at the angles not greater than 80°, tritons identified at angles from 10° to 60°, and helium-3 and helium-4 measured at 10° and 30°. In total, the 39 analyzed beam and target combination systems generating 1469 light charged particle yield spectra will be a benchmark dataset for comparisons to various transport codes to help investigate the accuracy of the transport codes. Additionally, the total dose equivalent for each analyzed light charged particle yield using the ICRP 60 quality factor and the NASA quality factors for solid cancers and leukemia were calculated.

The PHITS simulations presented in this work were designed by the author to compare with the experimental yields. The comparison between the experimental data, and PHITS and MCNP simulated results presented in this work will benefit the discussion on the differences between these Monte Carlo simulations for light charged particle production from thick target bombardment and will further help improve the physics models used in the transport codes. The proton yields are the most well-reproduced by PHITS and MCNP across the analyzed 39 systems. For the complex light ions, the simulations can predict better at the forward detection angles. In terms of Monte Carlo simulation comparison, the experimental yields were better matched by PHITS for HDPE upstream target systems while MCNP modeled more closely for Al upstream target systems. Additionally, the difference between the experimental and simulated results generally reduces with an increase in the mass number of incoming beam projectiles. Also, both PHITS and MCNP were able to replicate the experimental results better for systems with beam energy of 400 and 800 MeV/n.

Furthermore, the dose equivalent calculations associated with the measured double-differential thick-target light charged particle yields using ICRP 60 quality factor and the NASA quality factors for solid cancers and leukemia provide a new dataset for discussion on the quality factors in terms of track structure model. The proton dose equivalent results for HDPE upstream target systems have higher dose equivalent values than Al and Al+HDPE upstream target systems. Typically, for the beam projectiles with energy that can fully penetrate the upstream target, the proton dose equivalent increases as the target thickness increases. This is because increasing shielding material can provide more possible interactions as the beam projectiles traverse the upstream target. Also, the projectile fragmentation is the main source of the secondary charged particle, the proton dose equivalents increase with increasing beam projectile mass number.

Future work includes comparisons of the experimental double-differential thick-target light charged particle yields and other transport code simulations for verification and validation of physics models using in various transport codes. Additionally, the experimental yield results presented in this dissertation indicate the importance of cross section measurements, especially for complex light ion production, to help improve the physics models that are used in different particle transport codes. In terms of experiment, for higher energy beam, the longer measurement time is needed for light charged particle data to get better statistics.

LIST OF REFERENCES

[1] ICRP, 1991. 1990 Recommendations of the International Commission on Radiological Protection. ICRP Publication 60. Ann. ICRP 21 (1-3).

[2] Thomas B. Borak, Lawrence H. Heilbronn, Lawrence W. Townsend, Rafe A. McBeth, and Wouter de Wet, “Quality factors for space radiation: A new approach,” *Life Sciences in Space Research*, vol. 1, pp. 96-102, 2014.

[3] J. A. Simpson, “Elemental and Isotopic Composition of the Galactic Cosmic Rays,” *Annu. Rev. Nucl. Part. Sci.*, vol. 33, no. 1, pp. 323–382, 1983.

[4] “Guidance on Radiation Received in Space Activities,” National Council on Radiation Protection and Measurements, NCRP Report No. 98, 1989.

[5] J. P. Wefel, “Instrumentation for Radiation Measurement in Space,” in *Proc. of the Workshop on the Radiation Environment of the Satellite Power System (SPS)*, Springfield, VA, pp. 117–183. U.S. DOE Report CONF-7809164, 1978.

[6] T. Nakamura and L. Heilbronn, *Handbook on Secondary Particle Production and Transport by High-Energy Heavy Ions*. Singapore: World Scientific Publishing Co. Pte. Ltd., 2006.

[7] F.A Cucinotta, L.W Townsend, J.W Wilson, J.L Shinn, G.D Badhwar, R.R Dubey, “Light ion components of the galactic cosmic rays: Nuclear interactions and transport theory,” *Adv. Sp. Res.*, vol. 17, no. 2, pp. 77–86, 1996.

[8] L. C. Simonsen, J. W. Wilson, M. H. Kim, and F. A. Cucinotta, “Radiation Exposure for Humans Mars Exploration,” Health Physics, vol. 79, pp. 515-525, 2000.

[9] G.D Badhwar, P.M O'Neill, “Galactic cosmic radiation model and its applications,” *Adv. Sp. Res.*, vol. 17, no. 2, pp. 7–17, 1996.

[10] Tony C. Slaba, Amir A. Bahadori, Brandon D. Reddell, Robert C. Singleterry, Martha S. Clowdsley, and Steve R. Blattnig, “Optimal shielding thickness for galactic cosmic ray environments,” *Life Sciences in Space Research*, vol. 12, pp. 1-15, 2017.

[11] A. Ferrari, P. R. Sala, A. Fasso, and J. Ranft, “FLUKA: A multi-particle transport code (Program version 2005),” CERN-2005-010 / SLAC-R-773, Oct. 2005.

[12] S. Agostinelli et al., “Geant4—a simulation toolkit,” *Nucl. Instrum. Methods Phys. Res. Sect. Accel. Spectrometers Detect. Assoc. Equip.*, vol. 506, no. 3, pp. 250–303, Jul. 2003.

[13] J. T. Goorley et al., “Initial MCNP6 release overview-MCNP6 version 1.0,” Nucl. Technol., vol. 180, pp. 298–315, Dec. 2012.

[14] T. Satoh et al., “Particle and Heavy Ion Transport code System, PHITS, version 2.52,” *J. Nucl. Sci. Technol.*, vol. 50, no. 9, pp. 913–923, Jul. 2013.

[15] J. W. Wilson, T. C. Slaba, F. F. Badavi, B. D. Reddell, and A. A. Bahadori, “Advances in NASA radiation transport research: 3DHZETRN,” *Life Sci. Space Res.*, vol. 2, pp. 6-22, Jul. 2014.

[16] J. W. Wilson, T. C. Slaba, F. F. Badavi, B. D. Reddell, and A. A. Bahadori, “3DHZETRN: Shielded ICRU spherical phantom,” *Life Sci. Space Res.*, vol. 4, pp. 46–61, Jan. 2015.

[17] P. M. O’Neil, “Badhwar–O'Neill 2010 Galactic Cosmic Ray Flux Model—Revised,” IEEE Trans. Nuc. Sci., vol. 57, pp. 3148-3153, 2010.

[18] Steven A. Walker, Lawrence W. Townsend, John W. Norbury, “Heavy ion contributions to organ dose equivalent for the 1977 galactic cosmic ray spectrum,” *Advances in Space Research*, vol. 51, no. 9, pp. 1792–1799, 2013.

[19] Committee on the Evaluation of Radiation Shielding for Space Exploration National Research Council, Managing Space Radiation Risk in the New Era of Space Exploration. National Academies Press, 2008.

[20] F. A. Cucinotta, M.-H. Y. Kim, and L. J. Chappell, “Space Radiation Cancer Risk Projections and Uncertainties-2012,” NASA/TP-2013-217375, 2013.

[21] John W. Norbury, Jack Miller, Anne M. Adamczyk, Lawrence H. Heilbronn, Lawrence W. Townsend, Steve R. Blattnig, Ryan B. Norman, Stephen B. Guetersloh, and

Cary J. Zeitlin, "Nuclear Data for Space Radiation," *Radiation Measurements*, vol. 47, no. 5, pp. 315–363, 2012.

[22] T. Kurosawa, T. Nakamura, N. Nakao, T. Shibata, Y. Uwamino, A. Fukumura, "Spectral measurements of neutrons, protons, deuterons and tritons produced by 100MeV/nucleon He bombardment," *Nucl. Instrum. Methods Phys. Res. A*, vol. 430, pp. 400-422, 1999.

[23] R. E. Prael and H. Lichtenstein, "User Guide to LCS : The LAHET code system," vol. LA-UR-89-3, 1989.

[24] Rovituso, Schuy, Weber, Brons, Cortés-Giraldo, La Tessa, Piasetzky, Izraeli, Schardt, Toppi, Scifoni, Krämer, and Durante, "Fragmentation of 120 and 200 MeV U^{-1} ^{4}He Ions in Water and PMMA Targets," *Physics in Medicine and Biology*, vol. 62, no. 4, pp. 1310-1326, 2017.

[25] Gunzert-Marx, K., H. Iwase, D. Schardt, and R S Simon, Secondary Beam Fragments Produced by 200MeV u^{-1} ^{12}C Ions in Water and Their Dose Contributions in Carbon Ion Radiotherapy," *New Journal of Physics*, vol. 10, no. 7, 2008.

[26] E. Haettner, H. Iwase, M. Krämer, G. Kraft, and D. Schardt, "Experimental study of nuclear fragmentation of 200 and 400 MeV/ u ^{12}C ions in water for applications in particle therapy," *Phys. Med. Biol.*, vol. 58, no. 23, pp. 8265–8279, 2013.

[27] Luis Castellanos, "Thick-Target Measurements of Light Ion Yields Relevant to Radiation Transport Calculations," Doctoral Dissertation, University of Tennessee, Knoxville, 2018.

[28] J. F. Ziegler and J. P. Biersack and M. D. Ziegler (2008). SRIM - The Stopping and Range of Ions in Matter. SRIM Co. ISBN 978-0-9654207-1-6.

[29] Ron Fox, "Data Acquisition and Online Analysis at the NSCL," National Superconducting Cyclotron Laboratory, 2007.

[30] N. A. McGirl, "Double Differential Neutron Yields Produced by Proton, Helium, and Iron Interactions in Thick Aluminum Targets," PhD diss., University of Tennessee, Knoxville, 2017.

[31] Tatsuhiko Sato, Yosuke Iwamoto, Shintaro Hashimoto, Tatsuhiko Ogawa, Takuya Furuta, Shin-ichiro Abe, Takeshi Kai, Pi-En Tsai, Norihiro Matsuda, Hiroshi Iwase, Nobuhiro Shigyo, Lembit Sihver and Koji Niita, "Features of Particle and Heavy Ion Transport Code System (PHITS) version 3.02," *J. Nucl. Sci. Technol.*, vol. 55, pp. 684-690, 2018.

[32] Hideo Hirayama, Yoshihito Namito, Alex F. Bielajew *et al.*, "The EGS5 Code System," SLAC-R-730 and KEK Report 2005-8. Stanford (CA) and Tsukuba: SLAC and KEK; 2005.

[33] A. Boudard, J. Cugnon, J.-C. David, S. Leray, and D. Mancusi, "New potentialities of the Liège intranuclear cascade model for reactions induced by nucleons and light charged particles," *Phys. Rev. C*, vol. 87, pp. 014606, 2013.

[34] Koji Niita, Satoshi Chiba, Toshiki Maruyama, Tomoyuki Maruyama, Hiroshi Takada, Tokio Fukahori, Yasuaki Nakahara, and Akira Iwamoto, "Analysis of the (*N,xN′*) reactions by quantum molecular dynamics plus statistical decay model," *Phys. Rev. C*, vol. 52, pp. 2620-2635, 1995.

[35] S. Furihata, "Statistical analysis of light fragment production from medium energy proton-induced reactions," *Nucl. Inst. Met. in Phys. Res. B*, vol. 171, pp. 251-258, 2000.

[36] Yosuke Iwamoto, Tatsuhiko Sato, Shintaro Hashimoto, Tatsuhiko Ogawa, Takuya Furuta, Shin-ichiro Abe, Takeshi Kai, Norihiro Matsuda, Ryuji Hosoyamada and Koji Niita, "Benchmark study of the recent version of the PHITS code," *J. Nucl. Sci. Technol.*, vol. 54, pp. 617-635, 2017.

[37] T. Goorley, M. James, T. Booth, F. Brown, J. Bull, L. J. Cox, J. Durkee, J. Elson, M. Fensin, R. A. Forster, J. Hendricks, H. G. Hughes, R. Johns, B. Kiedrowski, R. Martz, S. Mashnik, G. McKinney, D. Pelowitz, R. Prael, J. Sweezy, L. Waters, T. Wilcox, and T.

Zukaitis, "Initial MCNP6 Release Overview," Nuclear Technology, vol. 180, no. 3, pp. 298-315, 2012.

[38] S. G. MASHNIK et al., "CEM03.01 User Manual," LA-UR-05-7321, Los Alamos National Laboratory, 2005.

[39] S. G. MASHNIK et al., "CEM03.03 and LAQGSM03.03 Event Generators for the MCNP6, MCNPX, and MARS15 Transport Codes," presented at the Joint ICTP-IAEA Advanced Workshop on Model Codes for Spallation Reactions, Trieste, Italy, February 4–8, 2008.

[40] K. K. GUDIMA, S. G. MASHNIK, and A. J. SIERK, "User Manual for the Code LAQGSM," LA-UR-01-6804, Los Alamos National Laboratory, 2005.

[41] Y. YARIV and Z. FRANKEL, "Intranuclear Cascade Calculation of High-Energy Heavy-Ion Interactions," *Phys. Rev. C*, Vol. 20, 1979.

[42] R. Brun and F. Rademakers, "ROOT—an object oriented data analysis framework," *Nucl. Instrum. Methods Phys. Res. Sect. Accel. Spectrometers Detect. Assoc. Equip.*, vol. 389, no. 1, pp. 81–86, 1997.

[43] Pi-En Tsai, "Study of Secondary Particles Produced from Heavy-Ion Interactions," Doctoral Dissertation, University of Tennessee, Knoxville, 2015.

[44] Berger, M.J., Coursey, J.S., Zucker, M.A., and Chang, J. (2005), *ESTAR, PSTAR, and ASTAR: Computer Programs for Calculating Stopping-Power and Range Tables for Electrons, Protons, and Helium Ions* (version 1.2.3). [Online] Available: http://physics.nist.gov/Star [*2017*]. National Institute of Standards and Technology, Gaithersburg, MD.

[45] L. Heilbronn, Y. Iwata, and H Iwase, "Off-line correction for excessive constant-fraction-discriminator walk in neutron time-of-flight experiments," *Nucl. Instrum. Methods Phys. Res. A*, vol. 522, no. 3, pp. 495-503, 2004.

VITA

Hui-Chen Wang is from Taiwan. She graduated from National Tsing Hua University with her B.S. in Engineering and System Science with concentrations in thermal hydraulics and nuclear energy in 2012 and her M.S. in Nuclear Engineering in 2014. She moved to Knoxville, Tennessee to attend the University of Tennessee working on her Ph.D. In addition to the research presented here, she also worked on Monte Carlo simulations of the mouse irradiated experiment from ^{252}Cf source. After graduation, she hopes to continue working in the field of radiation transport and detection.